

Optics and Quantum Electronics

Academic Staff

Prof. James G. Fujimoto, Prof. Erich P. Ippen, Professor Franz X. Kärtner

Research Staff, Visiting Scientists and Affiliates

Dr. Yu Chen, Dr. Mariana Carvalho, Dr. Linze Duan, Dr. Richard Ell, Dr. Robert Huber, Dr. Faith Omer Ilday, Dr. Christian Jirauschek, Dr. Francisco Lopez-Royo, Dr. Shun-ichi Matsushita, Dr. Thorsten Mack, Dr. Oliver Muecke, Dr. Norihiko Nishizawa, Dr. Lelia A. Paunescu, Dr. Thomas R. Schibli, Prof. Alphan Sennaroglu, Dr. Luciano Socci, Dr. Hideyuki Sotobayoshi, Dr. Kenji Taira, Dr. Phillipp Wagenblast, Dr. Macie Wojtkowski, Dr. Rebecca Younkin

Graduate Students

Desmond Adler, Aaron Aguirre, Jonathan Birge, Jeff Chen, Marcus Dahlem, Fuwan Gan, Blaise Gssend, Juliet Gopinath, Felix Grawert, Paul Herz, Pei-lin Hsiung, Aristidis Karalis, Jung-Won Kim, Tony Ko, Andrew Kowalevich, Lia Matos, Milos Popovic, Poh-Boon Phua, Peter Rakich, Karen Robinson, Vikas Sharma, Hanfei Shen, Jason Sickler, Vivek Srinivasan, Michael Watts, Aurea Tucay Zare

Technical and Support Staff

Dorothy Fleischer, Donna Gale

Research Areas and Projects

Ultrashort Pulse Generation and Laser Technology

Multiple-pass cavity (MPC) lasers general design principles
Generation of 150 nJ pulses from a multiple-pass cavity KLM Ti:Al₂O₃ oscillator
High performance, compact, prismless, low-threshold 30 MHz Ti:Sapphire laser
An extended cavity Cr:LiSAF laser pumped by low-cost laser diodes
Stretched-pulse high-power femtosecond fiber laser and supercontinuum (SC generation at 1.55 μm)
Nonlinear propagation and continuum generation effects in fibers
Broadband mode-locked Cr:forsterite laser
Computational methods for optimization of dispersion compensating mirrors
Ultrabroadband beam splitter with matched group delay dispersion
10 fs diode pumped Cr:LiCAF laser for high-resolution optical coherence tomography
Ultrabroadband Ti:Sapphire laser using oxidized AIAs/InGaAlP saturable bragg reflectors
Combined saturable absorber - modulator for active control of mode-locked lasers
Silicon-germanium-based semiconductor saturable absorbers for laser modelocking

Ultrafast Phenomena and Quantum Electronics

Laser micromachining of photonic devices in transparent materials
Laser cooling with ultrafast pulse trains
Carrier-envelope phase detection
Third-order nonlinearities in chalcogenide glasses suitable for high-index contrast fiber devices
Nonlinear nanocrystallite materials for laser mode-locking

Photonics and Devices

Integrated tunable, switchable optical add-drop multiplexer design

All optical switching and modulation in silicon by carrier injection

Polarization effects in lightwave systems

Broadband Spectral Measurements of High-Index Photonic Circuits using Supercontinuum Light

Source from 1-2 μm

Demonstration of line-defect guidance and adiabatic mode conversion in 2-dimensional photonic crystal formed from posts at optical wavelengths

Integrated polarization splitter and rotator designs

Optical Phase Control and Stabilization Techniques

Direct frequency comb generation from an octave-spanning Ti:Sapphire laser

Optical clockwork without the need for carrier-envelope phase control

Femtosecond Synchronization of RF-signals with Optical Pulse Trains

Publications, Presentations, Thesis and Books

Ultrashort Pulse Generation and Laser Technology

Multiple-Pass Cavity (MPC) Lasers General Design Principles

Sponsors

National Science Foundation – ECS-01-19452

Air Force Office of Scientific Research – F49620-01-01-0084

Project Staff

Dr. Alphan Sennaroglu, Andrew M. Kowalevicz, Professor James G. Fujimoto

The four-mirror resonator design that is the standard in Kerr lens mode-locking (KLM) lasers has been extensively examined to describe sensitivity to misalignment, stability, and to optimize performance [1-3]. While other similar cavities utilizing two- and three-mirror designs have also been analyzed [4,5], resonator configurations suitable for femtosecond pulse generation have remained basically unchanged. Moreover, there has been no significant advance in cavity architecture since the first KLM laser in 1991. In order to enable appreciable performance enhancements while allowing for compact cavity dimensions, we have worked out a general theory for multipass cavity (MPC) design.

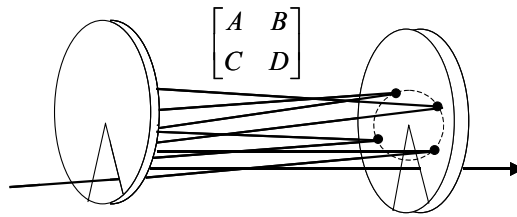


Figure 1. A schematic of a general multipass cavity. One round-trip is represented by the ABCD matrix.

A schematic of a Herriott-like MPC is shown in Figure 1. In its simplest form, an MPC consists of a stable two-mirror resonator and a mechanism for injecting and extracting light beams. When the MPC parameters are properly adjusted, the incident beam injected with the correct offset and tilt undergoes multiple bounces before exiting. When using appropriate design conditions developed in our theory, the MPC can leave the Gaussian beam q parameter invariant, so that the stability map of the standard KLM cavity is preserved. Therefore, MPCs enable the laser pulse energy to be increased by decreasing the repetition rate. MPCs also allow for the development of very compact lasers while preserving standard repetition rates and pulse energies.

The theory is based on the ABCD representation for a single round-trip through the MPC. It has been shown [6] that the final matrix representing the complete n round-trips through the MPC can be expressed as

$$M_T^n = \begin{bmatrix} \frac{A-D}{2} \frac{\sin n\theta}{\sin \theta} + \cos n\theta & B \frac{\sin n\theta}{\sin \theta} \\ C \frac{\sin n\theta}{\sin \theta} & \frac{D-A}{2} \frac{\sin n\theta}{\sin \theta} + \cos n\theta \end{bmatrix},$$

where A , B , C , and D are the matrix elements of the single round-trip matrix. By using the appropriate initial conditions, we show that θ is the angular advance on an end mirror of the MPC, as illustrated in Figure 2, after each of the n successive round-trips. By examining the above expression for M_T^n , it becomes clear that the MPC performs a q -preserving transformation ($q'=q$)

whenever $n\theta = m\pi$, where m is an integer. In other words, whenever the beam traverses an integer number of semicircular paths around the perimeter of the end mirrors, the MPC is q -preserving.

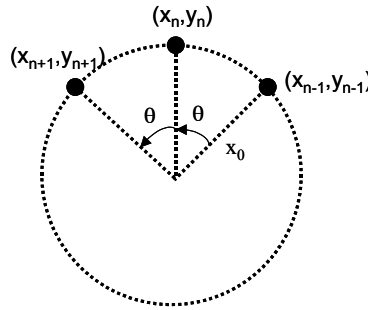


Figure 2. The spot pattern formed by the beams upon successive transits will, in general, be elliptical at a given reference plane in the cavity. For the proper choice of initial conditions, a circular spot pattern is obtained. In either case, the angular advance between successive round-trips is q .

The theoretical evaluation shows that, for any choice of m , there are infinitely many choices of n that lead to a q -preserving solution. Physically, most solutions can be rejected in practice due to finite beam size and the need to be able to inject and extract the beam from the cavity without interfering with adjacent beam paths. We show that based on possible injection and extraction techniques, there are a total of 32 possible two-mirror MPC designs. Each design offers unique advantages and disadvantages to particular types of laser performance goals.

References

1. T. Brabec, C. Spielmann, P.F. Curley, and F. Krausz, "Kerr lens modelocking," *Optics Letters* 17(18): 1292-1294 (1992).
2. V. Magni, G. Cerullo, and S. De Silvestri, "ABCD matrix analysis of propagation of gaussian beams through Kerr media," *Optics Communications* 96: 348-355 (1993).
3. V. Magni, G. Cerullo, S. De Silvestri, and A. Monguzzi, "Astigmatism in Gaussian-beam self-focusing and in resonators for Kerr-lens mode locking," *J. Opt. Soc. Am. B* 12(3): 476-485 (1995).
4. H.A. Haus, J.G. Fujimoto, and E.P. Ippen, "Analytic Theory of Additive Pulse and Kerr Lens Mode Locking," *IEEE J. Quant. Elect.* 28: 2086-2096 (1992).
5. V.I. Kalashnikov, V.P. Kalosha, I.G. Poloyko, and V.P. Mikhailov, "Optimal resonators for self-mode locking of continuous-wave solid-state lasers," *J. Opt. Soc. Am. B* 14(4): 964-969 (1997).
6. A. Sennaroglu and J.G. Fujimoto, "Design criteria for Herriott-type multi-pass cavities for ultrashort pulse lasers," *Optics Express* 11(9): 1106-1113 (2003).

Generation of 150 nJ Pulses from a Multiple-Pass Cavity KLM Ti:Al₂O₃ Oscillator

Sponsors

National Science Foundation – ECS-01-19452

Air Force Office of Scientific Research – F49620-01-01-0084

Project Staff

Andrew M. Kowalevich, Dr. Alphan Sennaroglu, Professor James G. Fujimoto, Professor Franz Kaertner

In addition to ultrafast studies, femtosecond lasers are utilized in nonlinear material processing. Even though pulse durations as short as around 5 fs [1,2] have been reached from conventional Ti:Sapphire lasers, the pulse energy is limited to a few nanojoules because of its high repetition rate. For material processing, high-energy pulses at moderate repetition rates are desirable.

We utilize a multiple-pass cavity (MPC) based on the Herriott cell to produce a unity-q transformation [3] that facilitates the lengthening of the cavity while maintaining the operating point of a standard laser. The long cavity lengths introduce significant dispersion from air and prismatic compensators produced higher order dispersion mismatch. Our current work uses specially designed double-chirped mirrors (DCMs) that compensate dispersion without the need for other intracavity dispersion compensating elements.

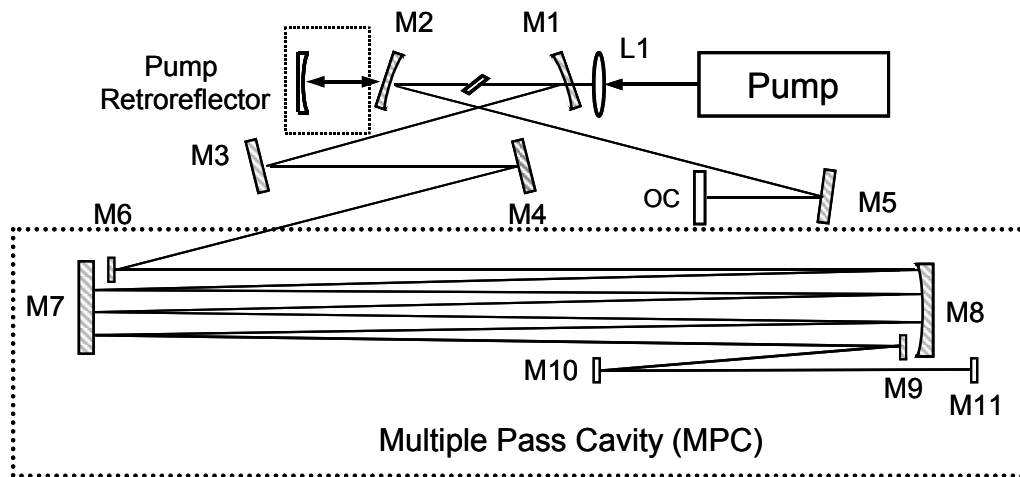


Figure 1. Schematic layout of the high-pulse-energy laser cavity. All shaded mirrors are DCMs. The pump source is a frequency-doubled Nd:Vanadate capable of 10W of light at 532 nm. The crystal is 3 mm thick and absorbs ~56% of the pump light on a single pass.

Figure 1 shows the schematic of the high-pulse-energy Ti:Al₂O₃ laser. The cavity length has been increased to 5.85 MHz repetition rate. Since our cavity length is approximately 20 times longer than a standard laser, we expect a similar scaling of the pulse energy for a given average output power. This substantially higher pulse energy leads to enhanced self-phase modulation (SPM). The additional frequency components from SPM would typically lead to progressively shorter pulses and considerably higher intensity in the gain medium, which, if left unbalanced, would overdrive the nonlinearities that lead to stable pulse generation. In order to balance the SPM, we increase the net negative dispersion. Our MPC adds 48 DCM bounces with approximately -46 fs² per bounce, leading to a net negative dispersion of -1250 fs² after accounting for the additional air path of 48 m.

In order to produce high pulse energies, we focus 9.4 W of pump light into our laser crystal. Since the crystal absorbs approximately 56% of the incident light, several watts of unabsorbed pump light are transmitted. We retroreflect this transmitted light with a 20 cm radius of curvature

mirror back into the crystal, which increases the average output power of the laser while also allowing for the use of a 25% output coupler (OC). This high percentage of output coupling, along with the large net negative dispersion, prevents the intracavity intensity from becoming too large. KLM is initiated by translating the end mirror (M11), which results in single-pulsed mode-locked operation with output powers as high as 877 mW.

To verify that the laser is, in fact, producing single pulses, the output is measured with a fast photodiode, an optical multichannel analyzer (OMA), as well as an intensity autocorrelator. The oscilloscope trace in Figure 2a shows spikes with 171 ns separation corresponding to the cavity round-trip time for 5.85 MHz. At the same time, the OMA monitors the laser spectrum, shown in Figure 2b. The mode-locked spectrum of the laser has 16.5 nm FWHM centered at 788 nm with dual symmetric sidebands, which are due to operation at large negative dispersion. In order to establish the duration of our pulses, we performed an intensity autocorrelation with a thin 300 μm KDP crystal. The measurement yields a FWHM of 67 fs resulting in a pulse width of 43 fs (Figure 2c), which is close to the transform limit of 39 fs, assuming a sech^2 pulse shape.

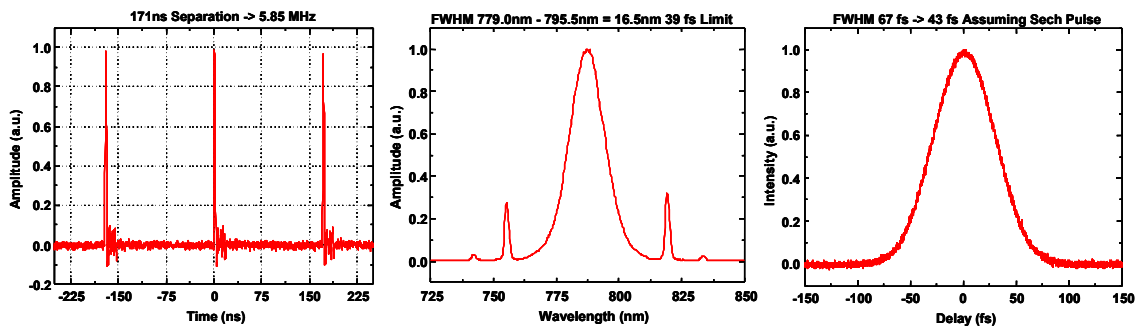


Figure 2. a) Pulse spikes from a fast photodiode at the repetition rate of the laser, b) the mode-locked spectrum of the laser with 16.5 nm FWHM, and c) the measured pulse duration of 43 fs which is close to the transform limit of 39 fs.

In conclusion, we have demonstrated a prismless, KLM $\text{Ti:Al}_2\text{O}_3$ laser operating at 5.85 MHz based on a Herriott-style MPC. Because of its unity transformation of the Gaussian beam in the MPC, we achieved long cavity laser performance with standard cavity laser stability. We have demonstrated 150 nJ pulses with 43 fs duration, corresponding to 3.5 MW peak power. We expect this performance which has never been achieved previously, to open new avenues for micromachining of materials that had only been possible before with amplified laser systems. It will also be a useful tool to eliminate thermal parasitics in pump probe and nonlinear optics experiments.

References

1. U. Morgner, F.X. Kartner, S.H. Cho, Y. Chen, H.A. Haus, J.G. Fujimoto, E.P. Ippen, V. Scheuer, G. Angelow, and T. Tschudi, "Sub-two-cycle pulses from a Kerr-lens mode-locked Ti:sapphire laser," *Optics Letters* 24(6): 411-413 (1999).
2. D.H. Sutter, G. Steinmeyer, L. Gallmann, N. Matuschek, F. Morier-Genoud, U. Keller, V. Scheuer, G. Angelow, and T. Tschudi, "Semiconductor saturable-absorber mirror-assisted Kerr-lens mode-locked Ti:sapphire laser producing pulses in the two-cycle regime," *Optics Letters* 24(9): 631-3 (1999).
3. D. Herriott, H. Kogelnik, and R. Kompfner, "Off-axis paths in spherical mirror interferometers," *Applied Optics* 3(4): 523-526 (1964).

High-Performance, Compact, Prismless, Low-Threshold 30 MHz Ti:Sapphire Laser

Sponsors

National Science Foundation – ECS-01-19452

Air Force Office of Scientific Research – F49620-01-01-0084

Project Staff

Andrew M. Kowalevich, Dr. Alphan Sennaroglu, Professor James G. Fujimoto, Professor Franz Kaertner

Practical femtosecond laser sources must meet several important requirements so that they can be readily integrated into systems and used in a wide range of scientific and technological applications. These requirements include low-cost design, compactness, and efficient all-solid-state operation with reasonably high pulse energies. One method for lowering the overall laser cost is to develop resonator configurations that permit low-threshold operation [1,2]. Because the pump laser is one of the most expensive components of a solid-state laser system, such a configuration will result in a dramatic cost reduction. The resultant decrease in average output power, however, leads to a decrease in the pulse energy and in the peak intensity, which limits the laser's use for applications that involve nonlinear optics. Previous studies have shown that pulse energy can be recovered by reducing the repetition rate of the laser. In particular, multipass cavity (MPC) configurations have been introduced to enhance laser performance while making efficient use of available pump power and space [3-5].

We have developed a novel Ti:Sapphire femtosecond laser that combines several favorable features to meet the system requirements described above. A schematic of the laser is shown in Figure 1. A 2-mm-thick Brewster-angled Ti:Al₂O₃ crystal (xtal) with a pump absorption coefficient of 6.84 cm⁻¹ at 532 nm is placed in an astigmatically compensated X cavity between two highly reflecting curved double-chirped mirrors (DCM's) (M1 and M2, R = 3 cm). The crystal is end-pumped at 532 nm by using a frequency-doubled, diode-pumped Nd:YVO₄ laser. The input pump lens (L1, f = 3.8 cm) focuses the pump beam to a 7 μm waist (1/e² radius) inside the gain medium. The overall transmission of the input lens (L1) and the input mirror of the resonator (M1) at 532 nm is 91.6%. The path length from M2 to the output coupler (OC) is 35 cm. The path length from M1 to the reference plane z_{R1} is 21 cm.

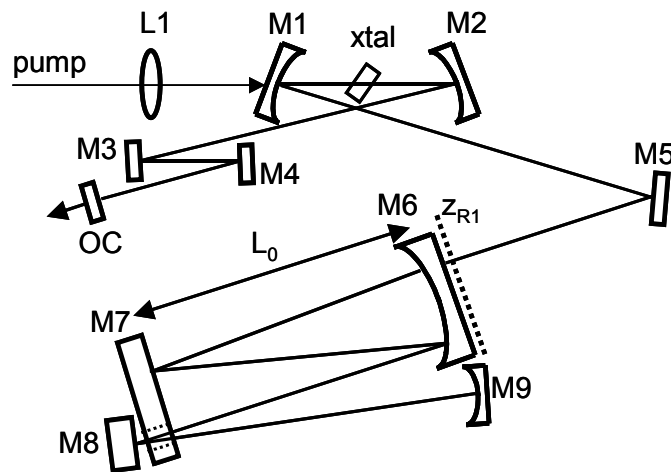


Figure 1. Schematic of the compact, prismless, low-threshold, multipass cavity femtosecond Ti:Al₂O₃ laser. Cavity lengths are extended and pulse energies increased using a multipass (MPC) cavity.

The laser, which is all-solid-state, has prismless dispersion compensation with DCMs [6,7], an MPC design to increase the effective cavity length, and tight focusing geometry to enable efficient low-threshold operation. The laser can operate using only 1.5 W of pump power. Although the effective cavity is approximately 5 meters long, an extremely compact design measuring only 30 x 45 cm has been achieved using an MPC.

The cavity length is extended by including an MPC that consists of high-reflectivity curved (M6, $R = 2$ m) and flat (M7) Bragg reflectors. The beam enters the MPC through a notch on the curved mirror and exits through a second notch on the flat mirror. The MPC is aligned so that the beam bounces form a circular spot pattern on each mirror. The mirror separation is 23.4 cm, resulting in successive spots separated by 40 degrees along the circular pattern. Starting at the input reference plane indicated as z_{R1} in Fig. 1, calculations show that when the bouncing beam makes nine full round-trips during a single transit through the MPC, the q parameter of the Gaussian beam upon exit is preserved and the Kerr lens mode-locking (KLM) operating point remains invariant. Because notches were used for coupling the beam into and out of the MPC in our design, only eight full round-trips are completed during a single pass. The remaining round-trip can be completed by retro-reflecting the exiting beam with a curved mirror located at a distance equal to the MPC mirror separation. The radius of curvature of this mirror must be $R/2$, where R is the radius of curvature of the curved MPC mirror (M6 in Fig. 1). This design, scalable to any value of R , always gives a q-preserving MPC, thus guaranteeing that the parameter of the Gaussian beam returning from the MPC is identical to that at the reference plane z_{R1} .

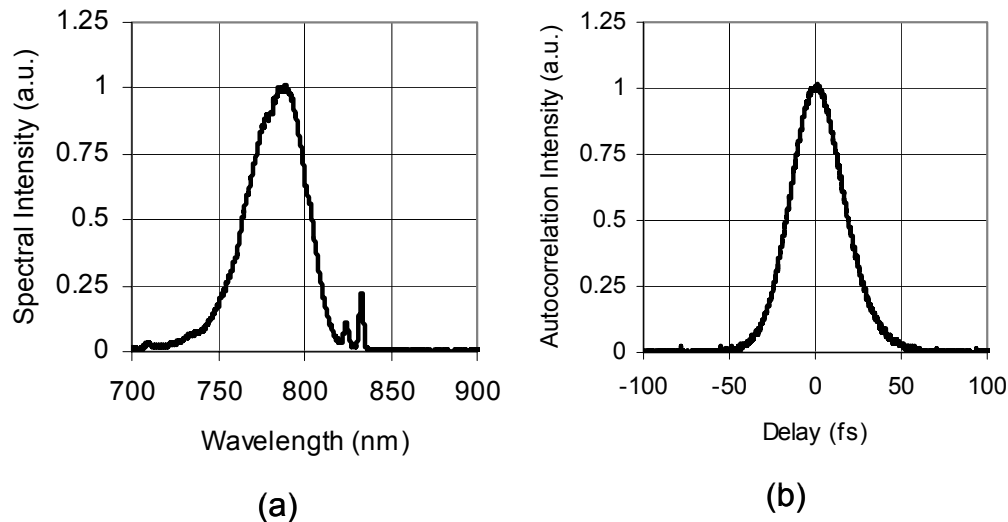


Figure 2. (a) Spectrum and (b) second harmonic intensity autocorrelation of the pulses obtained from the multipass $\text{Ti:Al}_2\text{O}_3$ oscillator. Pulse durations of 23 fs with bandwidths of 40 nm are generated.

With 1.5 W of pump power, up to 88 mW of mode-locked output power is obtained, corresponding to 2.8 nJ of pulse energy at 31.25 MHz repetition rate. This pump power is chosen because compact, low-cost pump lasers operating with this output power are now available. Figure 2(a) shows the mode-locked output spectrum. The spectrum is centered at 790 nm and has a FWHM of 40 nm. Figure 2 (b) shows the measured pulse duration corresponding to 23 fs pulses, assuming a sech^2 pulse shape.

References

1. K. Read, F. Blonigen, N. Riccielli, M. Murnane, and H. Kapteyn, "Low-threshold operation of an ultrashort-pulse mode-locked Ti:sapphire laser," *Optics Letters* 21(7): 489-491 (1996).
2. A.M. Kowalewicz, T.R. Schibli, F.X. Kartner, and J.G. Fujimoto, "Ultralow-threshold Kerr-lens mode-locked Ti:Al₂O₃ laser," *Optics Letters* 27(22): 2037-2039 (2002).
3. A.R. Libertun, R. Shelton, H.C. Kapteyn, and M.M. Murnane. "A 36 nJ-15.5 MHz extended-cavity Ti:Sapphire oscillator," paper presented at the *Conference on Lasers and Electro-Optics*, Baltimore, MD, 1999.
4. S.H. Cho, B.E. Bouma, E.P. Ippen, and J.G. Fujimoto, "Low-repetition-rate high-peak-power Kerr-lens mode-locked Ti:Al₂O₃ laser with a multiple-pass cavity," *Optics Letters* 24(6): 417-19 (1999).
5. S.H. Cho, F.X. Kärtner, U. Morgner, E.P. Ippen, J.G. Fujimoto, J.E. Cunningham, and W.H. Knox, "Generation of 90-nJ pulses with a 4-MHz repetition-rate Kerr-lens mode-locked Ti:Al₂O₃ laser operating with net positive and negative intracavity dispersion," *Optics Letters* 26(8): 560-562 (2001).
6. F.X. Kartner, N. Matuschek, T. Schibli, U. Keller, H.A. Haus, C. Heine, R. Morf, V. Scheuer, M. Tilsch, and T. Tschudi, "Design and fabrication of double-chirped mirrors," *Optics Letters* 22: 831-833 (1997).
7. N. Matuschek, F.X. Kärtner, and U. Keller, "Analytic design of double-chirped mirrors with custom-tailored dispersion characteristics," *IEEE Journal of Quantum Electronics* 35: 129-137 (1999).

An Extended Cavity Cr:LiSAF Laser Pumped by Low-Cost Laser Diodes

Sponsors

National Science Foundation – ECS-01-19452

Air Force Office of Scientific Research – F49620-01-01-0084

Project Staff

Aurea Zare, Dr. Alphan Sennaroglu, Professor James G. Fujimoto, Professor Franz Kaertner

The Ti:Sapphire laser, which emits femtosecond pulses at about 800 nm, is a standard laser in the laboratory today. However, increased use of this laser is inhibited by its high retail price. A substantial fraction of the cost comes from the pump source, which is typically a solid-state CW laser that emits several watts at 532 nm and costs tens of thousands of dollars. An alternative to Ti:Sapphire is the Cr:LiSAF gain medium, which has a broad emission bandwidth at about 850 nm and can be pumped at 670 nm with red laser diodes [1]. These laser diodes are relatively inexpensive: single spatial mode diodes emitting at 660-690 nm wavelengths with output powers of 50-60 mW can be purchased at about \$20 each. Modelocked Cr:LiSAF lasers pumped by single spatial mode diodes have been demonstrated by other researchers [2,3]. However, the highest pulse energy achieved from these lasers was 0.14 nJ [3], and we believe there is still room for improvement.

We demonstrate a single spatial mode diode-pumped, extended cavity Cr:LiSAF laser that uses a multipass cavity (MPC) to increase the output pulse energy [4]. Two different lasers were built: a prismless one that uses only double-chirped mirrors (DCMs) for dispersion compensation, and another that uses prisms. The prismless laser produces 39 fs pulses with 20 nm bandwidth and 0.75 nJ pulse energy at a repetition rate of 8.6 MHz. The laser using prisms generates 43 fs pulses, 18.5 nm bandwidth, and 0.66 nJ pulse energy at 8.4 MHz repetition rate.

Figure 1 shows the schematic of the extended cavity Cr:LiSAF laser. The pump source consists of two 50 mW diodes at 663 nm (D1 and D3), and one 50 mW diode at 685 nm (D2). Mode-locking is initiated and stabilized by a saturable Bragg reflector (SBR). The MPC consists of M6 and M7, which are flat and curved ($R=4$ m) DCMs respectively, which are separated by 2 meters. In one round-trip, a laser pulse experiences 16 bounces on the MPC mirrors, which corresponds to an added cavity length of 32 meters. Figure 2 shows the autocorrelation and spectrum of the laser that uses prisms; Figure 3 shows the same for the laser that uses DCMs for dispersion compensation.

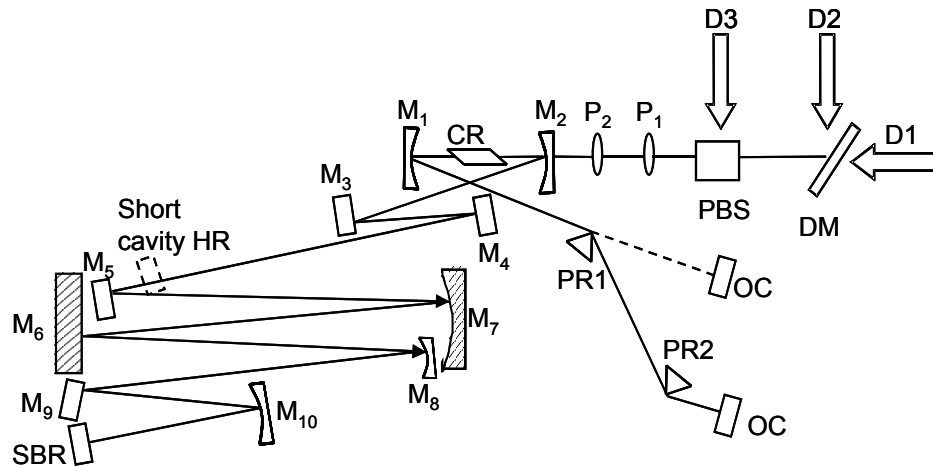


Figure 1. Experimental setup of the extended cavity femtosecond Cr:LiSAF laser.

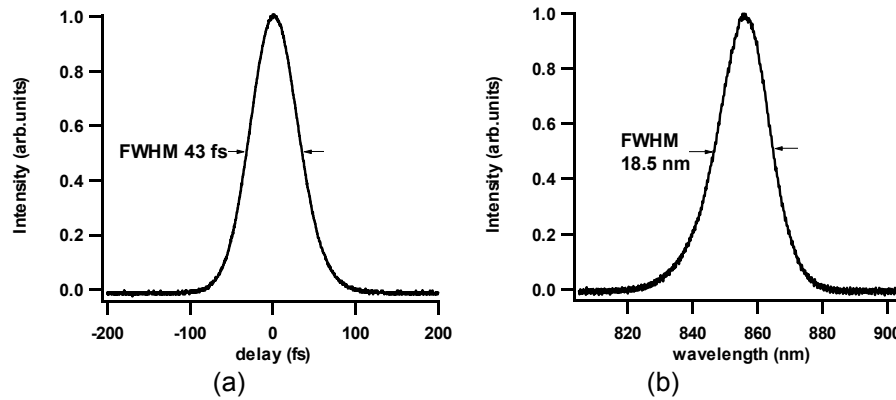


Figure 2. Autocorrelation (a) and spectrum (b) of the extended cavity Cr:LiSAF laser using prisms for dispersion compensation.

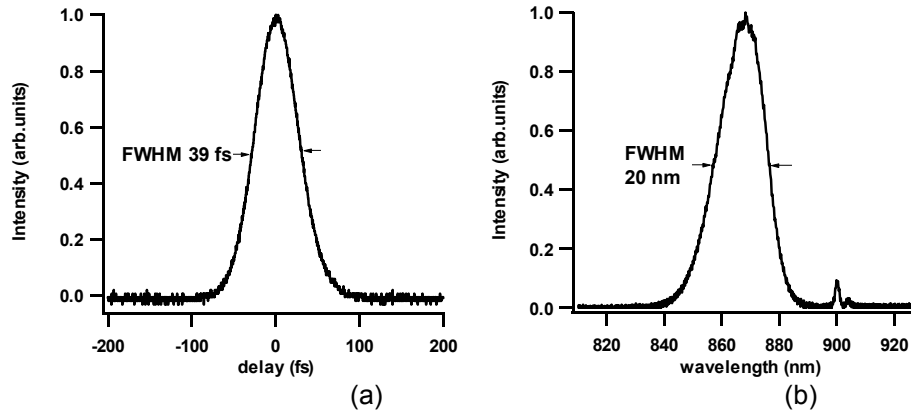


Figure 3. Autocorrelation (a) and spectrum (b) of the extended cavity Cr:LiSAF laser using only DCMs for dispersion compensation.

References

1. L.K. Smith, S.A. Payne, W.L. Kway, L.L. Chase, and B.H.T. Chai, "Investigation of the Laser Properties of $\text{Cr}^{3+}:\text{LiSrGaF}_6$," *IEEE Journal of Quantum Electronics* 28(11): 2612-2618 (1992).
2. J.M. Hopkins, G.J. Valentine, B. Agate, A.J. Kemp, U. Keller, and W. Sibbett, "Highly compact and efficient femtosecond Cr:LiSAF lasers," *IEEE Journal of Quantum Electronics* 38(4): 360-368 (2002).
3. B. Agate, B. Stormont, A.J. Kemp, C.T.A. Brown, U. Keller, and W. Sibbett, "Simplified cavity designs for efficient and compact femtosecond Cr:LiSAF lasers," *Optics Communications* 205(1-3): 207-213 (2002).
4. R.P. Prasankumar, Y. Hirakawa, A.M. Kowalewicz, F.X. Kaertner, J.G. Fujimoto, and W.H. Knox, "An extended cavity femtosecond Cr:LiSAF laser pumped by low cost diode lasers," *Optics Express* 11(11): 1265-1269 (2003).

Stretched-Pulse High-Power Femtosecond Fiber Laser and Supercontinuum (SC) Generation at 1.55 μm

Sponsors

National Institute of Health – R01-CA75289-06, R01-EY11289-18

National Science Foundation – ECS-01-19452, BES-0119494

Air Force Office of Scientific Research – F49620-01-1-0186, F49620-01-01-0084

Project Staff

Dr. Norihiko Nishizawa, Vikas Sharma, Professor Erich P. Ippen, Professor James G. Fujimoto

Fiber laser is robust, compact, and stable, so it is a useful light source for practical applications. Using the combination of fiber laser and highly nonlinear fibers, we demonstrate an all-fiber-type high-power supercontinuum source. Because the optical scattering in tissues is reduced and the penetration depth is increased at longer wavelengths, the wavelength region around 1.4-1.6 μm is of interest for optical coherence tomography (OCT) imaging [1,2]. This wavelength region is also attractive for the characterization of optical devices or spectroscopic applications using water absorption [3].

We have developed an all-fiber-type high-power supercontinuum source at 1.55 μm . A low-noise supercontinuum with 38 mW power and 180 nm bandwidth is generated using a high-power, stretched-pulse, passively mode-locked fiber laser and highly nonlinear fiber. An almost octave-spanning, wideband supercontinuum is also generated using highly nonlinear dispersion-shifted fibers.

Figure 1 shows the experimental setup of the high-power stretched-pulse passively mode-locked Er-doped fiber laser [4]. Recently, the combination of fiber laser and fiber amplifier is used to obtain high-energy pump pulse for supercontinuum generation [5-7]. Using the stretched-pulse fiber laser scheme, we can obtain clean high-energy ultrashort pulses without the additional fiber amplifier. The two high-power pump, 350 mW, laser diodes (LDs) at 980 nm are used as the pump light source. The output beams are combined using a polarization beam combiner (PBC) to introduce the high-power pump beams into the cavity. A normal dispersive, high-concentration Er-doped fiber is used as the gain device. The total dispersion in the cavity is set to be +0.0126 ps to demonstrate stable high-energy single-pulse operation. A birefringent plate and a polarizing beam splitter (PBS) are used in combination as a bandpass filter to obtain single-pulse operation. A linearly-chirped, high-energy output pulse is obtained using the rejected component in the mode-locking obtained through nonlinear polarization rotation. The average output power is 100 mW and the repetition rate is 50.9 MHz. The width of the spectrum is 70 nm at a center wavelength of 1.55 μm . The temporal width of the output pulse is 1.7 ps and the pulse energy is 2 nJ. The laser is capable of stable self-starting operation.

The output of the fiber laser is coupled into a 1.45-m-long SMF-28 to compress the temporal width of the output pulses to a minimum value. The SMF-28 is spliced to a 95 m normal dispersive highly nonlinear fiber (ND-HNF) to generate a smooth SC. The mode field diameter of the ND-HNF is 4 μm , the dispersion is $D = -4.74$ ps/km/nm, and the dispersion slope is 0.008 ps²/km/nm.

Figure 2(a) shows the optical spectra of the output pulses. The output from the fiber laser has a spectrum width of 70 nm. A near-Gaussian-shaped supercontinuum spectrum is generated stably at the output of the ND-HNF. The width of the spectrum is 180 nm (FWHM) and the optical power is 38 mW.

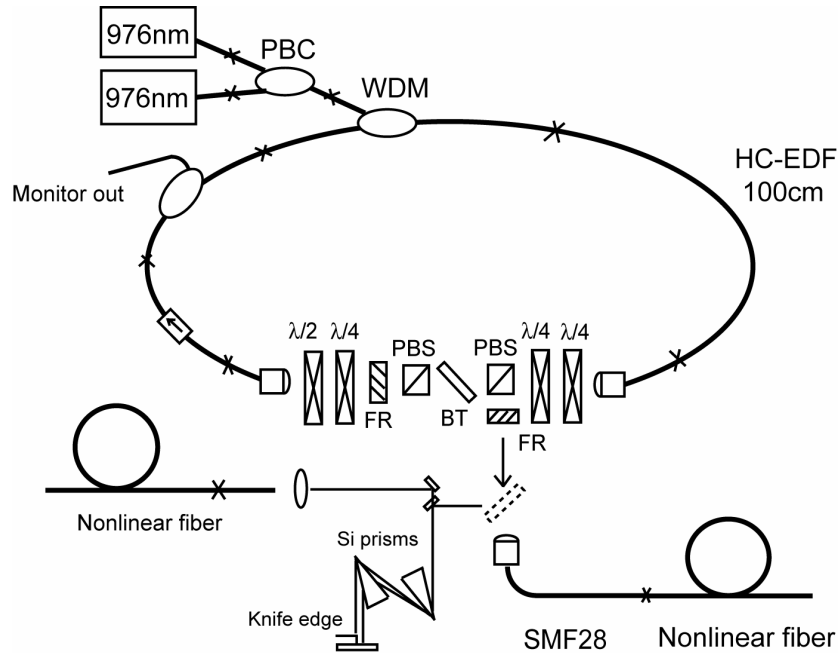


Figure 1. Scheme of stretched-pulse passively mode-locked high-power femtosecond fiber laser and supercontinuum generation scheme at 1.55 μm .

The spectrum shape changes in the fiber pulse compression stage due to nonlinear effects during the compression process. The small sharp peaks in the generated supercontinuum may be caused by nonlinear interaction between multiple spectral peaks of the compressed pulse. When a Si prism pair and spectrum filtering is used for pulse compression, a smooth supercontinuum without sharp modulation is generated because nonlinear effects do not alter the spectrum shape during the compression process (Fig.2b). In this scheme, the problem is the 3 dB coupling loss into the fiber after the prism compression.

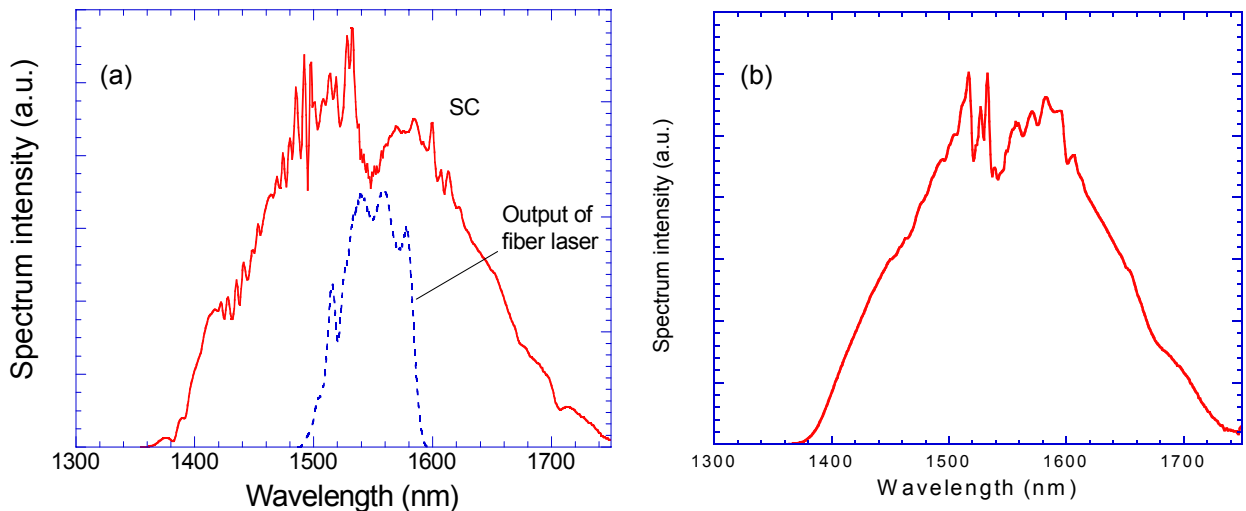


Figure 2. Optical spectrum of generated supercontinuum using (a) fiber compressor and (b) Si prism compressor.

Figure 3 shows the observed noise spectrum of the fiber laser and the generated supercontinuum. The intensity noise of the light source is characterized using a fast photodiode, bias-tee, and radio-frequency (RF) spectrum analyzer. Although peaks exist in the 10-20 MHz region, the noise level is low. The magnitude of the noise is not increased during the supercontinuum generation process. This is consistent with the results obtained using a Nd:Glass femtosecond laser and highly nonlinear fiber [8].

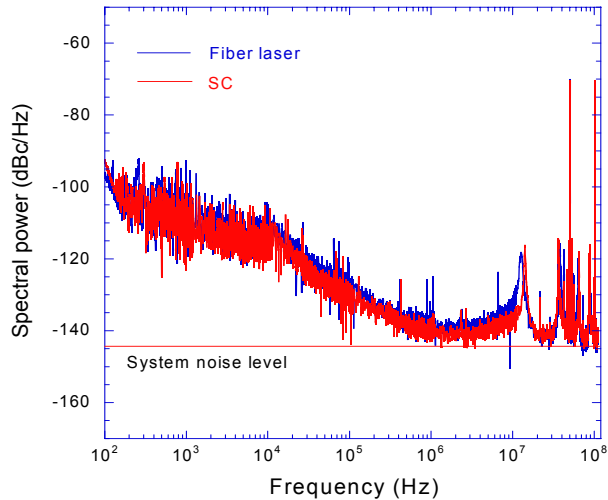


Figure 3. RF noise spectra for fiber laser and super continuum.

Figure 4 shows the wideband and low-noise supercontinuum generated using the combination of highly nonlinear dispersion-shifted fiber and highly nonlinear normal dispersive fiber. The spectrum is broadened from 1190 to over 1750 nm and the bandwidth is over 560 nm at -10 dB level. It does not have the fine structures and it is also useful for ultrahigh resolution or spectroscopic OCT.

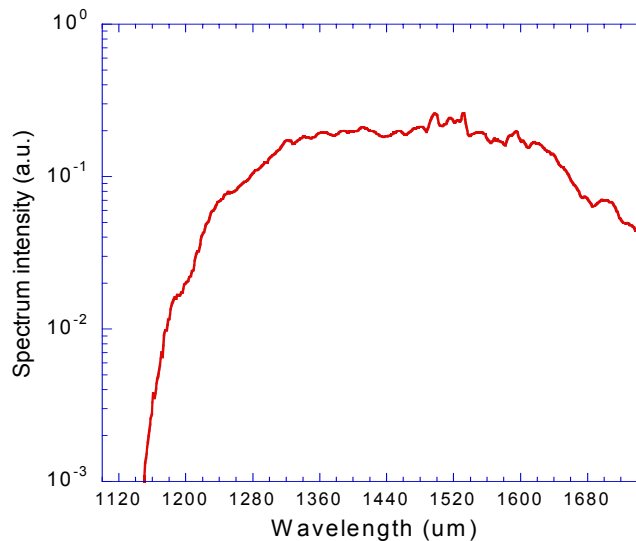


Figure 4. Optical spectrum of wideband supercontinuum.

References

1. B.E. Bouma, L.E. Nelson, G.J. Tearney, D.J. Jones, M.E. Brezinski, and J.G. Fujimoto, "Optical coherence tomographic imaging of human tissue at 1.55 μm and 1.81 μm using Er and Tm-doped fiber sources," *Journal of Biomedical Optics* 3(1): 76-9 (1998).
2. J.M. Schmitt, A. Knüttel, M. Yadlowsky, and M.A. Eckhaus, "Optical coherence tomography of a dense tissue - statistics of attenuation and backscattering," *Physics in Medicine and Biology* 39(10): 1705-1720 (1994).
3. J.M. Schmitt, S.H. Xiang, and K.M. Yung, "Differential absorption imaging with optical coherence tomography," *Journal of the Optical Society of America A* 15(9): 2288-96 (1998).
4. K. Tamura, C.R. Doerr, L.E. Nelson, H.A. Haus, and E.P. Ippen, "Technique for obtaining high-energy ultrashort pulses from an additive-pulse mode-locked erbium-doped fiber ring laser," *Optics Letters* 19: 46-48 (1994).
5. N. Nishizawa and T. Goto, "Widely broadened supercontinuum generation using highly nonlinear dispersion shifted fibers and femtosecond fiber laser," *Jpn. J. Appl. Phys.* 40: 365-367 (2001).
6. J.W. Nicholson, M.F. Yan, P. Wisk, J. Fleming, F. DiMarcello, E. Monberg, A. Yablon, C. Jorgensen, and T. Veng, "All-fiber, octave-spanning supercontinuum," *Optics Letters* 28(8): 643-645 (2003).
7. K. Bizheva, B. Povazay, B. Hermann, H. Sattmann, W. Drexler, M. Mei, R. Holzwarth, T. Hoelzenbein, V. Wacheck, and H. Pehamberger, "Compact, broad-bandwidth fiber laser for sub-2- μm axial resolution optical coherence tomography in the 1300-nm wavelength region," *Optics Letters* 28(9): 707-9 (2003).
8. S. Bourquin, A.D. Aguirre, I. Hartl, P. Hsiung, T.H. Ko, J.G. Fujimoto, T.A. Birks, W.J. Wadsworth, U. Bunting, and D. Kopf, "Ultrahigh resolution real time OCT imaging using a compact femtosecond Nd: Glass laser and nonlinear fiber," *Optics Express* 11(24): 3290-3297 (2003).

Nonlinear Propagation and Continuum Generation Effects in Fibers

Sponsors

National Institute of Health – R01-CA75289-06, R01-EY11289-18

National Science Foundation – ECS-01-19452, BES-0119494

Air Force Office of Scientific Research, Medical – F49620-01-1-0186, F49620-01-01-0084

Project Staff

Dr. Norihiko Nishizawa, Aaron D. Aguirre, Dr. Robert Huber, Vikas Sharma, Professor James G. Fujimoto

Recently, the technologies of ultrashort-pulse laser source and optical fibers have been advanced and the nonlinear pulse propagation along the fiber is an interesting research topic from several aspects. We have analyzed the nonlinear propagation of ultrashort pulses along fibers, both experimentally and numerically for two projects: (1) Analysis of supercontinuum generation for optical coherence tomography (OCT); and (2) High-energy ultrashort-pulse delivery using optical fiber.

Analysis of supercontinuum generation in terms of optical coherence tomography

As the light source, we use a compact diode-pumped femtosecond Nd:Glass laser. It generates ultrashort pulses with 100 fs duration with 160 mW average power at 50 MHz repetition and 1064 nm wavelength. Figure 1 shows the optical spectrum and corresponding point spread function for ultrahigh numerical aperture fiber. This fiber has large positive dispersion and small mode field diameter. Using the positively dispersive highly nonlinear fiber, we can generate Gaussian-like supercontinuum. When the coupling power is 100 mW, a 140 nm widely broadened supercontinuum is generated as shown in Fig.1(a). Using this supercontinuum, we can obtain an almost side-lobe-free point spread function. The axial resolution is 4.3 μm in air and the RF noise is not increased through the supercontinuum generation process. This supercontinuum is also robust for power fluctuation of coupling power, thus we can demonstrate stable imaging using this supercontinuum. The experimental results are well in agreement with the numerical ones obtained using the strict nonlinear Schrödinger equation.

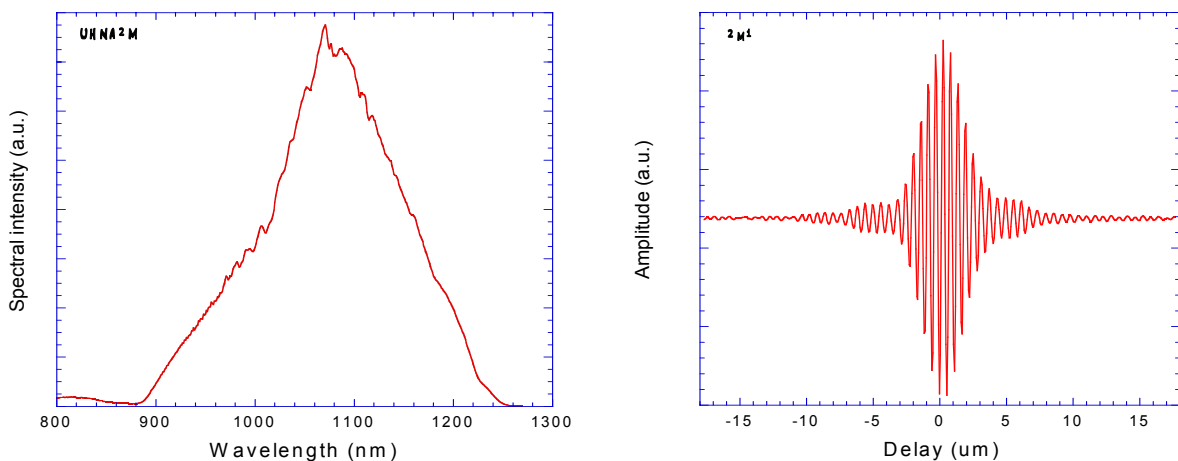


Figure 1. Optical spectrum and point spread function for a supercontinuum generated with positively dispersive highly nonlinear fiber.

Figure 2 shows the results for a generated supercontinuum using 1 m of photonic crystal fiber whose zero-dispersion wavelength is close to the pump wavelength. Using the zero-dispersive fibers, we can generate widely broadened supercontinuum. When the coupling power is 100 mW, the observed bandwidth of supercontinuum is larger than 300 nm at FWHM but the spectrum shape is complicated and there are many fine peaks. For the observed point spread function, the resolution width is almost 2 μm but there are large side lobes. The experimental results are also in agreement with the numerical results. The fine structure in the spectrum is sensitive to the power fluctuation.

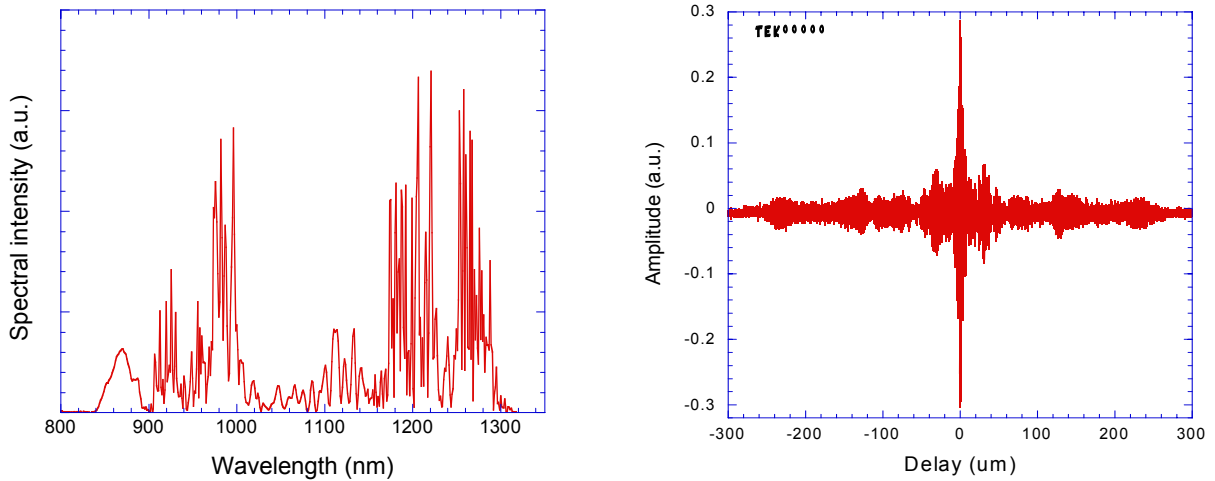


Figure 2. Optical spectrum and point spread function for supercontinuum generated with zero-dispersive highly-nonlinear fiber (photonic crystal fiber, PCF).

Figure 3 shows the numerical results of spectrum variation using the combination of these two fibers. The ultrashort pulse is first coupled into the PCF and the wideband supercontinuum with a lot of peaks is generated. Then the generated supercontinuum is coupled into positively dispersive, highly nonlinear fiber. In this fiber, the spectral peaks are suppressed and the spectrum shape is flattened, due to the effect of self-phase modulation and normal dispersion. We can obviously see the suppression of side lobes in the point spread function. This cascade connection method of different fibers is effective for smooth and wideband supercontinuum generation for high resolution OCT.

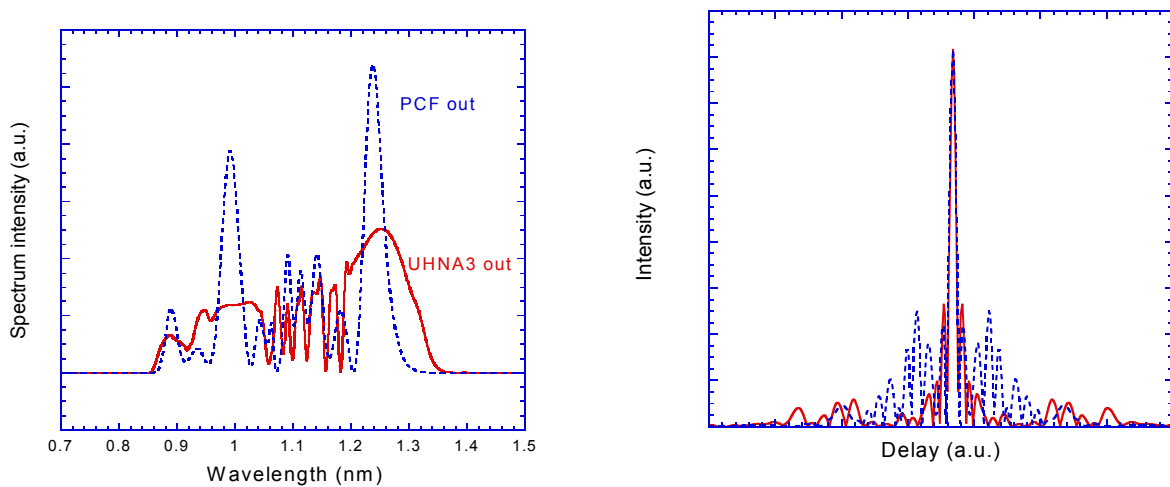


Figure 3. Optical spectrum and point spread function for super continuum generated with cascade connection of zero-dispersive highly-nonlinear fiber (photonic crystal fiber) and positively-dispersive highly-nonlinear fiber.

High-energy ultrashort-pulse delivery using spectrum broadening technique

High-energy ultrashort-pulse delivery is an important technique for endoscopic multiphoton microscopy, ultrashort-pulse processing, ultrashort-pulse surgery, etc. Recently, the multimode photonic crystal fiber that is suited for the single-mode propagation was demonstrated. Using this fiber, we can demonstrate the pulse propagation in a large-mode field area. The nonlinear effect in optical fiber is a limiting factor for high-energy ultrashort-pulse propagation.

Here, we propose a new approach to demonstrate high-energy ultrashort-pulse propagation. We have discovered that if we apply the spectral broadening process before the delivery fiber, we can obtain an ultrashort pulse whose energy is much higher than that without the spectrum broadening.

Figure 4(a) shows the temporal shape and chirping of an assumed input pulse. The pulse energy is 10 nJ and the temporal width is 4 ps. This condition of the input pulse is obtained by using the back propagation method. Figure 4(b) shows the temporal shape of the input and output pulse for the delivery fiber. We can obtain a 10 nJ almost pedestal-free 170 fs ultrashort pulse at fiber output. Figure 4(c) shows the variation of peak power of the propagating pulse. The peak power is nonlinearly increased and takes the maximum value at 1 m of the fiber output. Figure 4(d) shows the optical spectra at the input and output of the delivery fiber. It is interesting to note that spectrum narrowing occurs and the spectrum width is narrowed from the input spectrum.

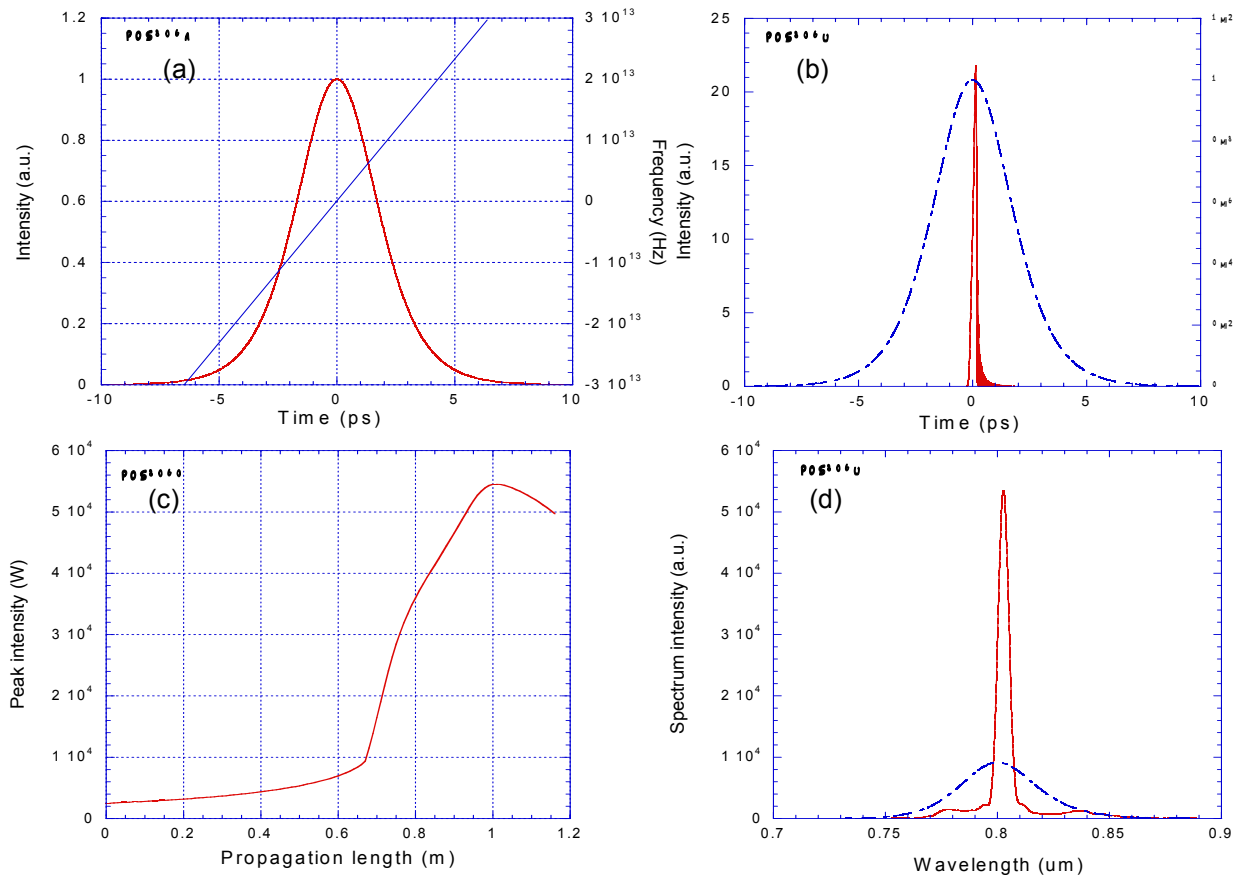


Figure 4. (a) temporal shape and chirping of input pulse, (b) temporal shape of input and output pulse, (c) variation of peak power, and (d) pulse spectrum shape.

Broadband Mode-Locked Cr:forsterite Laser

Sponsors

Office of Naval Research - N00014-02-1-0717

Air Force Office of Scientific Research - F49620-01-01-0084

Project Staff

Jung-Won Kim, Dr. Thomas Schibli, Sheila Tandon, Juliet Gopinath, Hanfei Shen, Dr. Gale Petrich, Professor Leslie A. Kolodziejski, Professor Erich P. Ippen, Professor Franz X. Kaertner

The construction of a broadband and stable Cr:forsterite laser is one of the most important tasks in single-cycle optical pulse synthesis using lasers [1]. It is difficult to generate very short pulses from Cr:forsterite due to its low gain, high third order dispersion and severe thermal loading [2]. For stable and broadband operation, we employed a broadband saturable Bragg reflector (SBR)[4].

Figure 1 shows the schematic of the broadband Cr:forsterite laser [3]. The resonator is a five mirror standard cavity used for SBR mode-locking. The laser uses a X-fold cavity design with 10 cm ROC curved mirrors. The focus on the SBR is designed to be 300 μm in diameter. The mirrors except OC are all double-chirped mirrors (DCMs) which provide negative dispersion inside the resonator. Calcium fluoride (CaF_2) wedges are used to fine-tune the overall dispersion. The wedge separation is small enough to avoid prism effects.

The Cr:forsterite crystal is 10 mm long with 0.9 cm^{-1} absorption coefficient, and purged with dry nitrogen to avoid water vapor condensation on the crystal. The crystal was kept at 5°C for mode-locked operation.

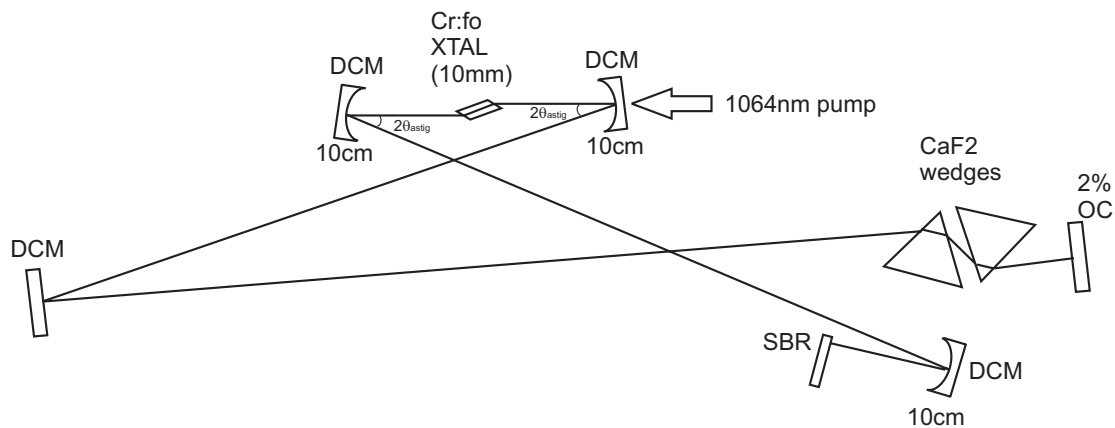


Figure 1. Broadband mode-locked Cr:forsterite laser [3].

The broadband saturable Bragg reflector (SBR) [4] consists of seven layer pairs of $\text{Al}_{0.3}\text{Ga}_{0.7}\text{As}$ /oxidized AlAs for the mirror structure, and a 40 nm thick InGaAs quantum well for the absorbing layer. Large area oxidized SBR-structures have been fabricated and are highly desirable to avoid problems involved with too tight focusing such as two photon absorption (TPA) and free carrier absorption (FCA).

The mode-locked output power is 50 mW with a 2 % output coupler at 6 W pump power. Figure 2 shows the measured output spectrum of the Cr:forsterite laser. The spectral range covers the range from 1080 nm up to 1500 nm at -30 dB from the peak power level. The 3-dB bandwidth is measured as 90 nm centered at 1243 nm. This bandwidth corresponds to the Fourier-transform limited pulse width of 19 fs assuming a sech^2 -pulse shape. This is one of the broadest spectra from a Cr:forsterite laser mode-locked by a semiconductor saturable absorber, tied with the

results in Refs. [5] and [6]. Compared to the previous Cr:forsterite laser used in Ref. [7], a significant improvement in spectral range, output power, and stability is obtained. This broadband Cr:forsterite laser will enable a more robust synchronization to an octave-spanning Ti:sapphire laser for single-cycle pulse synthesis.

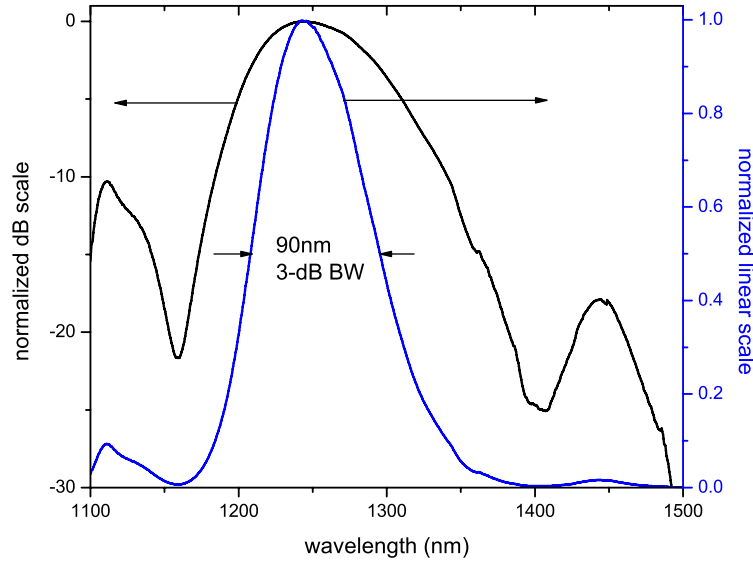


Figure 2. Measured spectrum of broadband Cr:forsterite mode-locked laser [3]. The 3-dB bandwidth is 90 nm centered at 1243 nm. The Fourier-transform limited pulsewidth is 19 fs.

References:

1. T.R. Schibli, O. Kuzucu, J. Kim, E.P. Ippen, J.G. Fujimoto, F.X. Kaertner, V. Scheuer, G. Angelow, "Toward Single-Cycle Laser Systems", *IEEE J. Sel. Top. Quant. Elec.* 9, 990-1001 (2003).
2. Z. Zhang, K. Torizuka, T. Itatani, K. Kobayashi, T. Sugaya, and T. Nakagawa, "Femtosecond Cr:Forsterite Laser with Mode Locking Initiated by a Quantum-Well Saturable Absorber", *IEEE J. Quant. Elec.* 33, 1975-1980 (1997).
3. J. Kim, "Toward Single-Cycle Optical Pulses", SM Thesis, MIT (2004).
4. S.N. Tandon, J.T. Gopinath, T.R. Schibli, G.S. Petrich, L.A. Kolodziejski, F.X. Kaertner, and E.P. Ippen, "Saturable absorber with large area broadband Bragg reflectors for femtosecond pulse generation", *CLEO 2003*, Baltimore, MD (2003).
5. Z. Zhang, K. Torizuka, T. Itatani, K. Kobayashi, T. Suguya, T. Nakagawa, H. Takahashi, "Broadband semiconductor saturable-absorber mirror for a self-starting mode-locked Cr:forsterite laser", *Opt. Lett.* 23, 1465-1467 (1998).
6. R.P. Prasankumar, C. Chudoba, J.G. Fujimoto, P. Mak, M.F. Ruane, "Self-starting mode locking in a Cr:forsterite laser by use of non-epitaxially-grown semiconductor-doped silica films", *Opt. Lett.* 27, 1564-1566 (2002).
7. T.R. Schibli, J. Kim, O. Kuzucu, J. Gopinath, S.N. Tandon, G.S. Petrich, L.A. Kolodziejski, J.G. Fujimoto, E.P. Ippen, and F.X. Kaertner, "Attosecond active synchronization of passively mode-locked lasers using balanced cross-correlation", *Opt. Lett.* 28, 947-949 (2003).

Computational Methods for Optimization of Dispersion Compensating Mirrors

Sponsors

Office of Naval Research - N00014-02-1-0717
 DARPA-Army Research Office - W11NF-04-1-0034

Project Staff

Jonathan R. Birge, Professor Franz X. Kaertner

The design and fabrication of dispersive optical thin-film filters and mirrors is a key ability for the generation of few-cycle laser pulses approaching the single-cycle regime [1]. Efficient and accurate calculation of dispersion properties (and gradients thereof) is indispensable for the design and optimization of these multilayer dielectric optical coatings.

The standard method for computing the group delay dispersion is to compute complex reflection coefficients using the transfer matrix technique and then take successive finite differences over frequency. For mirror systems containing up to 160 layers this leads to a large numerical effort during optimization. In addition, accurately computing the m th order dispersion at a single wavelength requires computing at least $(m+1)$ reflection coefficients and taking m finite differences. Unfortunately, numerical differentiation is inherently unstable, especially for higher order derivatives [2], and achieving high accuracy requires careful optimization of sample spacing to balance the competing effects of round off error and truncation error. We have developed a method to analytically compute dispersion to any order and show how approximations in the derivative lead to highly efficient algorithms for dispersion calculations. In practice, the first m derivatives of phase at a given wavelength can be computed in less time than for m zeroth-order reflection coefficients, resulting in significantly faster computation time than with numerical differentiation and yet without the associated issues of numerical stability or phase unwrapping.

This method can be extended to the efficient computation of analytic gradients of group delay for use in the numerical optimization of a filter's dispersive properties. The efficiency of this method allows for the simultaneous numerical optimization of a complete pair of double-chirped mirrors (a 160-dimensional space) in less than a minute.

1. Efficient Analytic Computation of Group Delay

Since derivatives of matrix products obey a product rule similar to scalars, if we know the zeroth through m th derivatives of the transfer matrix of a given structure, we can know all $(m+1)$ derivatives of some new structure composed of the given one plus a single added layer. In this way we can inductively compute any analytic derivative of any arbitrary structure in a memory efficient way. Most importantly, however, neglecting the effects of material dispersion on the coupling between forward and backward waves (which turns out to be a very good approximation) allows for significant computational simplification. In this limit, computing $(m+1)$ derivatives involves only $(m+1)$ full matrix multiplications and thus the analytic method requires the same number of matrix operations as the finite difference method. Furthermore, each matrix involved is a trivial transformation of a previously computed matrix. As such, the transcendental functions (trigonometric or exponential) needed to determine the basic transfer matrix for a given layer need only be computed once. Such transcendental functions actually take more time to compute than a matrix multiplication on most computers, so it turns out that in practice the analytic method is actually considerably faster than the finite difference method [4]. We find that the approximate analytic method is roughly three times faster than the standard finite difference algorithm, with negligible loss in accuracy.

The induction rules for the first several derivatives are given by [4]

$$\frac{\partial \mathbf{T}_{(1,0)}}{\partial k} = D_1^{(1)} \mathbf{T}_{(1,0)} + \mathbf{T}_1 \mathbf{T}'_{(1,-1,0)},$$

$$\frac{\partial^2 \mathbf{T}_{(1,0)}}{\partial k^2} = D_1^{(2)} \mathbf{T}_{(1,0)} + 2D_1^{(1)} \mathbf{T}_1 \mathbf{T}'_{(1,-1,0)} + \mathbf{T}_1 \mathbf{T}''_{(1,-1,0)},$$

$$\frac{\partial^3 \mathbf{T}_{(1,0)}}{\partial k^3} = D_1^{(3)} \mathbf{T}_{(1,0)} + 3D_1^{(2)} \mathbf{T}_1 \mathbf{T}'_{(1,-1,0)} + 3D_1^{(1)} \mathbf{T}_1 \mathbf{T}''_{(1,-1,0)} + \mathbf{T}_1 \mathbf{T}'''_{(1,-1,0)}.$$

Here the D s represent operators that compute the transfer matrix derivative with respect to k . However, in the case of lossless transfer matrices, such operators are equivalent to complex scalar multiplications. Thus, every term but the last on the right hand side is a simple multiplication of a previously computed value.

Optimization Results

A numerical routine to calculate the gradient of the phase derivatives of a mirror was developed based on the above algorithm. Its efficiency was such that it allowed for the simultaneous numerical optimization of a pair of double-chirped mirrors in terms of their total dispersion and reflectivity. Previously, the mirrors were optimized sequentially, resulting in such slow convergence that a truly optimal solution for the total pair was never obtained. Implementing the gradient computation in optimized C, we were able to improve existing DCM pairs to a locally optimal solution in around 11 seconds. Figure 1 shows the improvement in group delay error obtained. The fast convergence time resulting from the algorithm improvements should open up new avenues for the numerical design of DCM pairs, such as stochastic optimization.

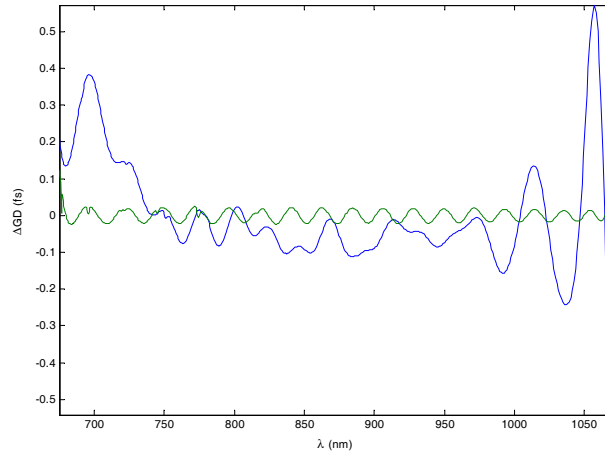


Figure 1. Group delay deviation of 160 layer DCM pair before and after optimization.

References:

- 1 T. R. Schibli, O. Kuzucu, J. Kim, E. P. Ippen, J. G. Fujimoto, F. X. Kaertner, V. Scheuer, and G. Angelow, "Toward single-cycle laser systems," *Journal of Selected Topics in Quantum Electronics* 9, 990–1001 (2003).
- 2 K. Atkinson, *An Introduction to Numerical Analysis* (Wiley, 1989), Chap. 5.
- 3 F. X. Kaertner, U. Morgner, T. R. Schibli, E. P. Ippen, J. G. Fujimoto, V. Scheuer, G. Angelow, and T. Tschudi, "Ultrabroadband double-chirped mirror pairs for generation of octave spectra," *J. Opt. Soc. Am. B* 18, 882–885 (2001).
- 4 J. R. Birge, C. Jirauschek and F. X. Kaertner, "Efficient analytic computation of group delay dispersion from optical interference coatings," OSA Thin Film Topical Conference, Tucson, Arizona (2004).

Ultrabroadband Beam Splitter with Matched Group Delay Dispersion

Sponsors

Office of Naval Research - N00014-02-1-0717
National Science Foundation - ECS 01-19452

Project Staff

Jung-Won Kim, Professor Franz X. Kaertner

As the pulse width of femtosecond lasers becomes shorter and shorter, the spectral range increases dramatically. Currently, pulses with octave-spanning spectra in the range of 600–1200 nm can be directly generated from mode-locked lasers [1]. For the characterization of such extremely short pulses using an interferometric auto-correlator (IAC) or the SPIDER method [2], ultra-broadband beam splitters for combining and splitting of the pulses without distortions are essential. Further, for a single-cycle optical pulse synthesis [3], which uses two broadband lasers ranging from 600 to 1500 nm, a beam splitter with well-controlled characteristics over the whole combined spectral range is necessary. Since conventional metallic beam splitters have considerable loss and strong wavelength dependence in reflection and transmission, it is highly desirable to design a broadband beam splitter based on multi-layer dielectric thin-film coating.

We report a new design for such an ultra-broadband beam splitter [4]. The key idea is to achieve the same group delay dispersion (GDD) for both reflection and transmission from any input ports to the output ports. In addition, this GDD is equal to the dispersion of a thin fused silica plate, which can be easily compensated either before or after the beam splitter. Figure 1 shows the schematic of the beam splitter. The design is carried out for p-polarized light with 45° angle of incidence. The fused silica substrate is about $655 \mu\text{m}$ thick, equal to a $750 \mu\text{m}$ ($=655/\cos(29.2^\circ)$) geometric path length in the substrate for 45° angle of incidence.

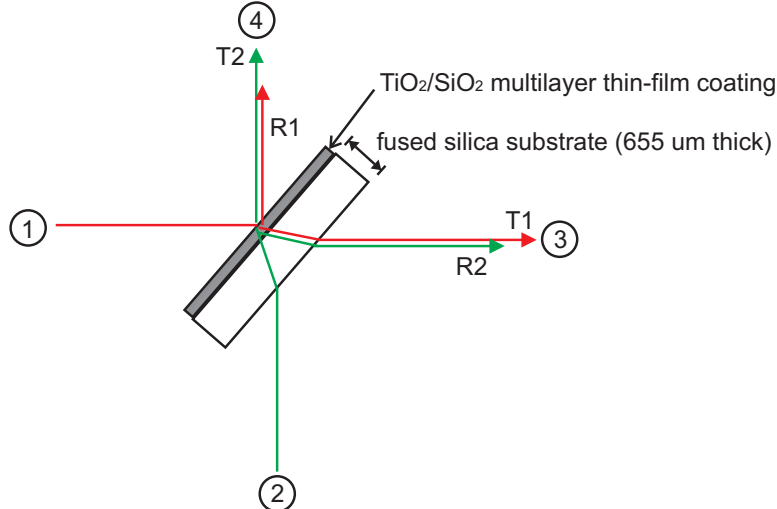


Figure 1. Ultrabroadband 50:50 beam splitter with matched group delay dispersion.

In designing the beam splitter, the group delay dispersion (GDD) for reflection from the coating (from port 1 to 4 in Fig. 1) is matched with the GDD of $750 \mu\text{m}$ of fused silica. In this condition, the GDD for any combination of input and output can be matched over the whole wavelength range. Let's denote the group delay (GD) of the coating between the air and the substrate interfaces with reflection R1 (from port 1 to 4 in Fig. 1), transmission T1 (from port 1 to 3 in Fig. 1), reflection R2 (from port 2 to 3 in Fig. 1), and transmission T2 (from port 2 to 4) by GD_{R1} , GD_{T1} , GD_{R2} , and GD_{T2} , respectively. In the design, the group delay for a single-pass in the substrate, GD_S , is matched with that of the coating reflection, up to a constant delay GD_0 , i.e. $\text{GD}_S = \text{GD}_{R1} + \text{GD}_0$. In this condition, the GDD from coating reflection is equal to the GDD from a single-pass in the

substrate, i.e. $GDD_{R1}=GDD_S$. The group delays for each optical path through the total beam splitter, i.e. coating plus substrate, are then given by GD_{R1} , $(GD_{T1}+GD_{R1}+GD_0)$, $(GD_{R2}+2(GD_{R1}+GD_0))$, and $(GD_{T2}+GD_{R1}+GD_0)$ for R1, T1, R2, and T2, respectively. For a lossless coating, the following relationships are generally valid: the group delays in transmission are identical, i.e. $GD_{T2} = GD_{T1}$, and the group delays in reflection satisfy $GD_{R2} = -GD_{R1}+2GD_{T1}$. Then the group delays can be expressed as GD_{R1} , $(GD_{T1}+GD_{R1}+GD_0)$, $(GD_{R1}+2GD_{T1}+2GD_0)$ and $(GD_{T1}+GD_{R1}+GD_0)$ for R1, T1, R2, and T2, respectively. Over the wavelength range of constant transmission, the GD for transmission through the coating, GD_{T1} , is almost constant, because the transmission through a dielectric coating is subject to a Kramers-Kroenig relation [5]. Therefore, the corresponding GDD is negligible. Thus, the GDD from any input to any output is matched with the GDD of the 750 μm thick fused silica, $GDD_S=GDD_{R1}$. Furthermore, one can show, with these relationships, that both output pulses (through ports 3 and 4 in Fig. 1) are perfectly overlapped in time by properly choosing the delay between two input pulses.

The coating consists of 38 layers of TiO_2 and SiO_2 on a fused silica substrate, and the total coating thickness is 3.54 μm . Figure 2 shows the reflectance/transmittance and the GD in reflection and transmission from the coating. The designed reflectance and transmittance are within $(50\pm 5)\%$ from 600 to 1500 nm. The resulting GD from coating reflection (solid black line in Fig. 2 (b)) is matched with that of 750 μm optical path length of fused silica up to a constant (dotted black line in Fig. 2(b)), (GD_S-GD_0) , within ± 1 fs from 650 to 1500 nm. This result demonstrates that the GDD in reflection from the coating is well matched with that of the substrate. The GD in transmission (dashed blue line in Fig. 2 (b)) is centered at 20 fs (dotted blue line in Fig. 2(b)) within ± 1 fs from 650 to 1500 nm.

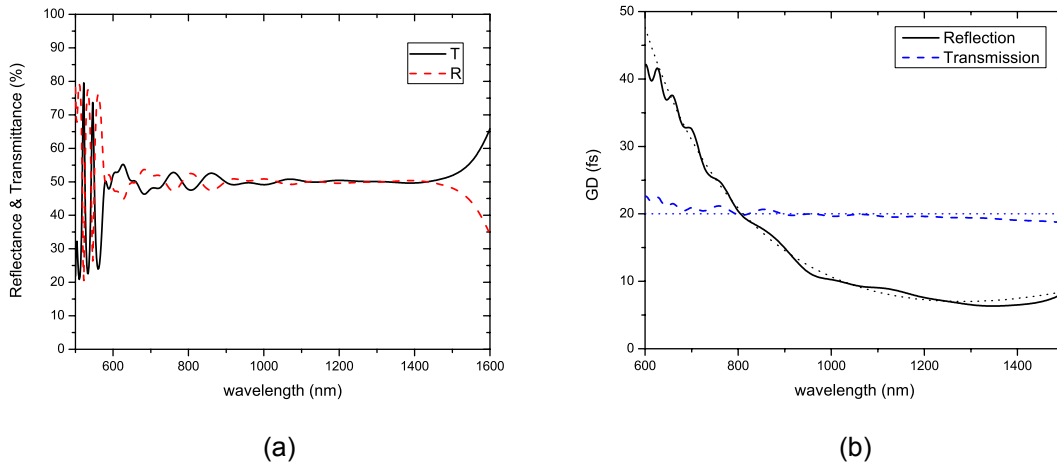


Figure 2: (a) Reflectance and transmittance of coating. (b) Group delay in reflection and transmission of coating.

References:

1. R. Ell, U. Morgner, F.X. Kaertner, J.G. Fujimoto, E.P. Ippen, V. Scheuer, G. Angelow, T. Tschudi, M.J. Lederer, A. Boiko, and B. Luther-Davies, "Generation of 5-fs pulses and octave-spanning spectra directly from a Ti:sapphire laser", *Opt. Lett.* 26, 373—375 (2001).
2. C. Iaconis and I.A. Walmsley, "Self-Referencing Spectral Interferometry for Measuring Ultrashort Optical Pulses", *IEEE J. Quant. Elec.* 35, 501—509 (1999).
3. T.R. Schibli, O. Kuzucu, J. Kim, E.P. Ippen, J.G. Fujimoto, F.X. Kaertner, V. Scheuer, G. Angelow, "Toward Single-Cycle Laser Systems", *IEEE J. Sel. Top. Quant. Elec.* 9, 990—1001 (2003).
4. J. Kim, F.X. Kaertner, V. Scheuer, G. Angelow, "Ultra-broadband beam splitter with matched group delay dispersion", to appear at Optical Interference Coating 2004.
5. G. Lenz, B.J. Eggleton, C.K. Madsen, C.R. Giles, and G. Nykolak, "Optimal Dispersion of Optical Filters for WDM Systems", *IEEE Photon. Tech. Lett.* 10, 567—569 (1998).

10 fs Diode Pumped Cr:LiCAF Laser for High-Resolution Optical Coherence Tomography

Sponsors

Air Force Office of Scientific Research - F49620-01-1-0084

Air Force Office of Scientific Research (MFEL) - F49620-01-1-0186

National Science Foundation - ECS-0119452 and BES-0119494.

Project Staff

Philipp Wagenblast, Tony H. Ko, Desmond Adler, Vikas Sharma, PD. Uwe Morgner, Professor James G. Fujimoto, Professor Franz X. Kaertner

Optical coherence tomography [1] has become a standard technique in ophthalmic diagnosis of glaucoma, macular edema and other retinal diseases. High axial resolution and high sensitivity imaging are achieved using low coherence interferometry with broadband, low coherence light sources. Using the ultra-broadband femtosecond output from Kerr-lens mode-locked Ti:sapphire lasers, axial image resolutions down to $3\ \mu\text{m}$ [2] have been achieved in retinal imaging. Compact and low pump power Ti:sapphire lasers have been developed to reduce complexity and cost of ultrahigh-resolution OCT systems. Directly diode-pumped, mode-locked lasers can provide an even further reduction in system cost. In this work, the output of a recently developed, mode-locked diode-pumped Cr:LiCAF laser is used to image the retina. The operating wavelength around $800\ \text{nm}$, similar to Ti:sapphire as well as superluminescent diode light sources, is well suited for ophthalmic imaging applications.

A diode-pumped ten fs laser [3] is modified in order to improve the interferometric point-spread function (PSF). Modulations in the spectrum of this laser originate from dispersion oscillations and are reduced by reducing the amplitude of the dispersion oscillations. This is accomplished by combining mirrors with an opposite dispersion ripple such that the oscillations cancel to a level where no visible influence on the spectrum is seen. A nearly Gaussian-shaped spectrum with a bandwidth of $89\ \text{nm}$ is achieved. The mode-locked output beam is coupled into a $5.5\ \mu\text{m}$, $1.14\ \text{NA}$ single mode fiber with a maximum power of $17\ \text{mW}$, i.e. 53% of the output power is coupled into the fiber. The diode-pumped laser has a foot print size of $20\ \text{x}\ 30\ \text{cm}$, and laser, pump diodes, and fiber coupling unit fit onto a $1\ \text{x}\ 2\ \text{foot}$ optical breadboard.

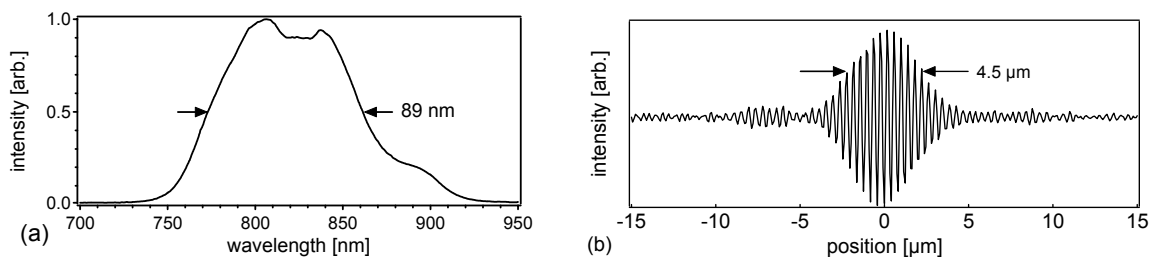


Figure 1. (a) fiber coupled mode-locked spectrum and (b) The measured point-spread function in air of the ophthalmic slitlamp imaging system was $4.5\ \mu\text{m}$ resolution.

OCT imaging system

For imaging of the human retina, an ultrahigh resolution ophthalmic OCT system was used. Dispersion between the reference and sample arms of the interferometer was carefully balanced. A high-speed, high-sensitivity, low-noise electronic detection system has been built in order to achieve high dynamic range and high sensitivity OCT imaging. A computer controls the scanning pattern of the OCT beam on the retina, acquires data, and generates an OCT image on the display in real time. The imaging system in the sample arm is based on a slit lamp biomicroscope which has an integrated CCD to provide a video image of the fundus of the eye. The subject's eye position is established by using an internal fixation target. After imaging is completed, axial motion artifacts in the image are corrected using standard cross-correlation algorithms. For OCT

imaging, the incident laser power on the eye was 600 μW . The measured PSF resolution of the system as shown in Fig. 1(c), is 4.5 μm in air, which corresponds to 3.4 μm in tissue. OCT imaging of the macular region of the retina was performed. Each OCT image consists of 3000 axial and 600 transverse pixels and was generated with scans of 1.5 mm in axial depth and 6 mm in the transverse direction.

Results

The images obtained with the Cr:LiCAF source can be compared with the corresponding images from the commercial OCT system (Zeiss Stratus OCT). The intensity profile of the backscattered light is mapped into a false color picture for enhanced visualization of intraretinal layers.

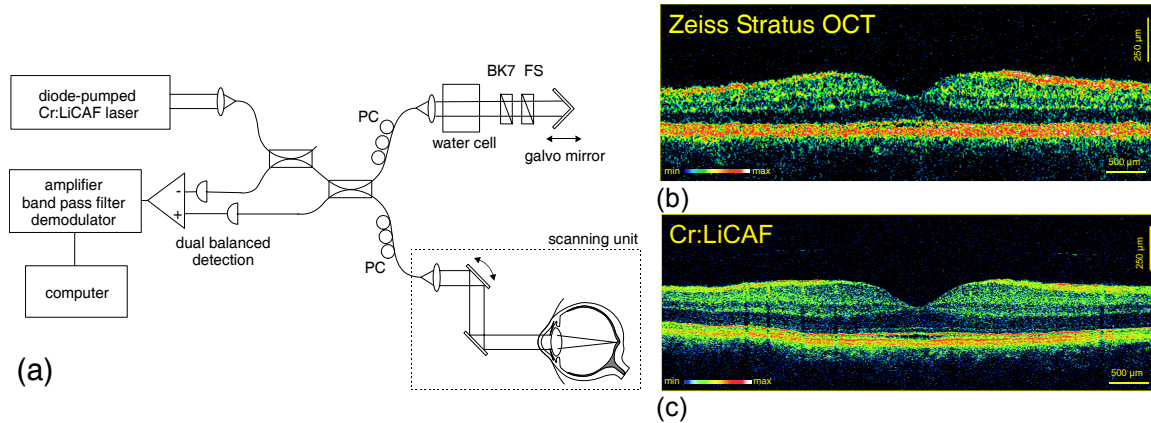


Figure 2. Left: (a) Fiber-interferometric OCT system. Dispersion and polarization of both interferometer arms are equalized separately. Right: Retinal images taken with (b) a commercial Stratus OCT system (Carl Zeiss Meditec, Dublin, CA) with 10 μm axial resolution in tissue, and (c) with the broadband, diode-pumped Cr:LiCAF laser as light source with 3.4 μm axial resolution in tissue.

Fig. 2 shows images of the right eye, taken with the commercial OCT system, and taken with our system employing the diode-pumped Cr:LiCAF laser as a light source. Comparing the ultrahigh resolution OCT images obtained with the Cr:LiCAF light source and the standard OCT images obtained with the commercial system demonstrates that the Cr:LiCAF light source yields approximately a 3x improvement in image resolution. Retinal structures and retinal layer boundaries are much better delineated using the ultrahigh resolution OCT-system than with the standard resolution OCT-imaging system. Specific structures such as the ganglion cell layer and the external limiting membrane are also much better visualized in the ultrahigh resolution image. The image quality obtained with the Cr:LiCAF source is very similar to the ultrahigh resolution OCT images previously obtained with a low-threshold Ti:Sapphire laser light source with 125 nm bandwidth centered around 800 nm which yields $\sim 3 \mu\text{m}$ resolution. Also the signal level of 92 dB when using the Cr:LiCAF-laser is close to the 94 dB obtained with the Ti:Sapphire laser light source. Thus essentially identical image quality is achieved by a light source that is direct diode-pumped, and has much reduced complexity, cost, and footprint size.

References

- D. Huang, E. A. Swanson, C. P. Lin, J. S. Schuman, W. G. Stinson, W. Chang, M. R. Hee, T. Flotte, K. Gregory, C. A. Puliafito, J. G. Fujimoto, "Optical coherence tomography," *Science* 254, 1178-1181 (1991).
- W. Drexler, U. Morgner, R. K. Ghanta, F. X. Kaertner, J. S. Schuman, J. G. Fujimoto, "Ultrahigh resolution ophthalmic optical coherence tomography," *Nature Med.* 7, 502-507 (2001).
- P. Wagenblast, R. Eil, U. Morgner, F. Grawert, F. X. Kaertner, "10-fs, diode-pumped Cr³⁺:LiCAF laser," *Opt. Lett.* 28, 1713-1715 (2003).

Ultrabroadband Ti:Sapphire Laser using oxidized AlAs/InGaAlP saturable Bragg reflectors

Sponsors

Office of Naval Research - N00014-02-1-0717

Air Force Office of Scientific Research - F49620-01-1-0084

Project Staff

Dr. Richard Ell, Sheila Tandon, J.T. Gopinath, G.S. Petrich, Professor Leslie A. Kolodziejski, Professor Erich P. Ippen, and Professor Franz X. Kaertner

The generation of ultrabroadband spectra and sub-10fs laser pulses in the near infrared spectral region is of major importance in many areas of research and applications. Especially in Optical Coherence Tomography, broad spectra implying short coherence lengths and therefore enable measurements with unprecedented resolution [1]. Short laser pulses themselves allow the study of fast dynamical processes, as such as in semiconductors [2]. A way to generate such broad spectra and short pulses is the implementation of Kerr-lens mode-locking in solid-state lasers with large gain bandwidth. Prominent systems are titanium-doped sapphire lasers [3] and Colquiriite based lasers, as for example chromium doped LiCAF [4]. It is desirable to use alternative mode-locking mechanisms such as mode-locking with semiconductor saturable Bragg reflectors (SBRs). The essential advantage of using SBRs is the fact that mode-locking is self-starting. In addition, the laser cavity does not need any sophisticated alignment procedure near the stability edge of the resonator. Using SBRs for mode-locking is also very helpful for laser materials with low nonlinearity, where Kerr-lens mode-locking is difficult or impossible to achieve.

Broadband Saturable Bragg Reflectors using Oxidized AlAs

Semiconductor saturable Bragg reflectors (SBRs) employing AlAs/GaAs or AlAs/AlGaAs mirrors limit the pulse-width in ultra-short laser systems due to the small bandwidth of the Bragg mirrors. Semiconductor absorbers transferred to a metal mirror by post processing offer a more broadband approach [5]. For Ti-Sapphire laser systems, use of an AlGaAs/CaF₂ mirror has also been demonstrated for broadband SBRs in the visible [6]. An alternative is to monolithically integrate absorbers onto broadband Bragg-mirrors with a low index layer created by steam oxidation of AlAs. The high index layer is selected depending on the wavelength of the laser system. For lasers in the infrared, AlGaAs/Al_xO_y mirrors have been used to create large area broadband SBRs [7]. Large scale oxidation techniques have also allowed for the creation of broadband Bragg reflectors in the visible wavelength range. In_{0.5}Ga_{0.15}Al_{0.35}P, with a bandgap at 536nm, is lattice matched to GaAs and can be used as the high index layer. With Al_xO_y as the low index layer, mirrors can be created for broadband reflection below 800nm. By incorporating a GaAs absorbing layer, this structure is completely unstrained and can be used for modelocking the Ti:Sapphire laser.

Mode-locking of a Titanium-sapphire Laser with an oxidized SBR

Oxidized SBRs for the near infrared have been successfully used in a Titanium-sapphire free space solid-state laser. The laser consisted of a standard z-folded cavity with a repetition rate of about 75MHz. One end mirror was replaced by a focusing mirror with a radius of curvature of R=100mm to focus onto the SBR active region. When the SBR was introduced into the cavity, replacing a high reflector, it introduced a decrease in CW power of about 20-30% which leads to estimated non-saturable losses of about 2-3%. Figure 1 displays mode-locked spectra from two different samples. The output power was in the order of 100-120mW with an output coupling mirror with 3% transmission at 800nm. The pump power was approximately 5W. The spectra extend over more than 100nm at FWHM and allow for sub-10fs pulse duration. The strong modulation of the spectra shown in Figure 1 are due to the broadband dispersion-compensating mirrors used in the laser cavity.

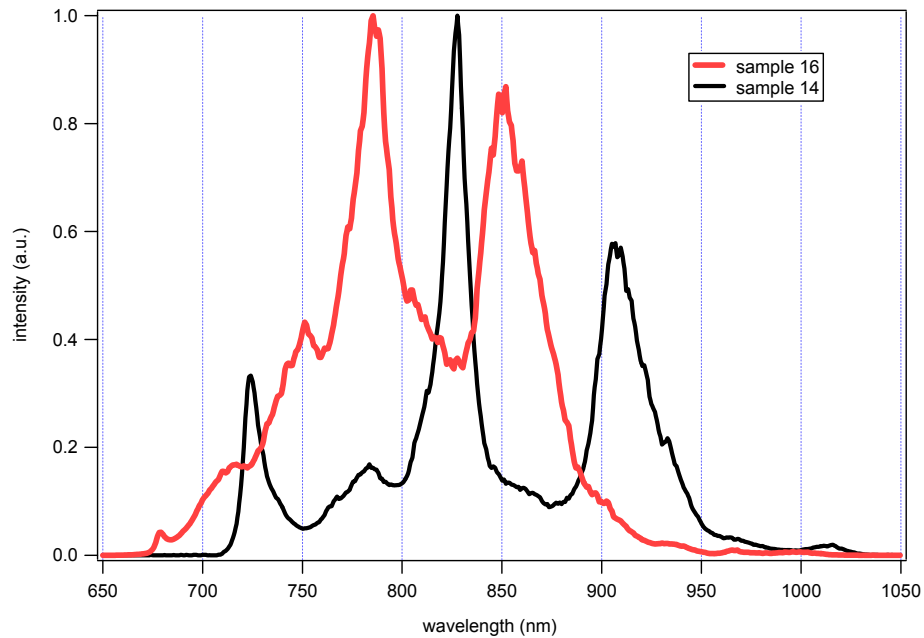


Figure 1: Mode-locked spectra as emitted by a 75 MHz repetition rate Titan-sapphire laser.

Next steps towards broadband SBR operated sub-10fs laser is on one hand the optimized growth of further generations of oxidized SBRs. The reflectivity bandwidth ought to be extended towards shorter wavelengths around 600-650nm and the modulation depth of the absorber, i.e. the thickness of the quantum well, may be increased. On the laser side, we intend to use dispersion compensating mirrors with smoother dispersion properties to be able to generate less modulated spectra.

Nevertheless, these first results are very promising and are supposed to be extended to other lasers like, for example, chromium doped LiCAF.

References:

1. A. D. Aguirre, P. Hsiung, T. H. Ko, I. Hartl, J. G. Fujimoto, "High-resolution optical coherence microscopy for high-speed, in vivo cellular imaging" *Opt. Lett.* 28(21), 2064 (2003).
2. O. D. Mücke, T. Tritschler, M. Wegener, U. Morgner, and F. X. Kaertner, "Signatures of Carrier-Wave Rabi Flopping in GaAs" *Phys. Rev. Lett.* 87, 057401 (2001).
3. R. Ell, U. Morgner, F. X. Kaertner, J. G. Fujimoto, E. P. Ippen, V. Scheuer, G. Angelow, T. Tschudi, M. J. Lederer, A. Boiko, and B. Luther-Davies, "Generation of 5-fs pulses and octave-spanning spectra directly from a Ti:sapphire laser" *Opt. Lett.* 26(6), 373 (2001).
4. P. Wagenblast, R. Ell, U. Morgner, F. Grawert, F. X. Kaertner, "Diode-pumped 10-fs Cr³⁺ LiCAF laser" *Opt. Lett.* 28(18), 1713 (2003).
5. Z. Zhang, T. Nakagawa, K. Torizuka, T. Sugaya, K. Kobayashi, "Gold-reflector-based semiconductor saturable absorber mirror for femtosecond mode-locked Cr⁴⁺:YAG lasers," *Applied Physics B*, 70, S59, 2000.
6. M. Haiml, L. Gallmann, U. Keller, "GaAs absorber layer growth for broadband AlGaAs/fluoride SESAMs" *Journal of Crystal Growth*, 227-228, 172, 2001.
7. S. N. Tandon, J. T. Gopinath, T. R. Schibli, G. S. Petrich, L. A. Kolodziejski, F. X. Kaertner, and E. P. Ippen. "Saturable Absorbers with Large Area Broadband Bragg Reflectors for Femtosecond Pulse Generation." Conference on Lasers and Electro-Optics (CLEO), 2003.

Combined saturable absorber - modulator for active control of mode-locked lasers

Sponsors

National Science Foundation - ECS 03-22740

Air Force Office of Scientific Research - F49620-01-1-0084

Project Staff

Felix J. Grawert, Juliet T. Gopinath, Dr. Ömer Ilday, Gale Petrich, Professor Leslie Kolodzieci, Professor Erich Ippen, Professor Franz X. Kaertner

The design of a novel optically-controllable saturable absorber for suppression of Q-switching instability in high repetition rate lasers is investigated. Initial attempts to modelock microchip lasers in the 10 GHz range with a semiconductor saturable absorber structure and employing established Q-switching suppression techniques have failed [1]. To address this shortcoming, we are pursuing the concept of an active feedback scheme that employs an optically-controlled semiconductor saturable absorber mirror that incorporates both saturable absorption and linear loss modulation [2].

The device is composed of a Bragg mirror, a quantum well and an additional layer that allows for intra-cavity loss modulation through free carrier absorption (Figure 1). Aiming for a wavelength around 1550 nm, a shorter wavelength (808nm or 670nm) with heavy absorption in the modulation layer will be employed for modulation.

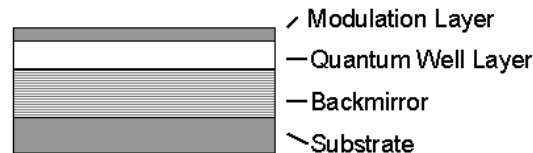


Figure 1. Schematics of the combined absorber-modulator. A backmirror provides the desired reflectivity, a quantum well the saturable absorption and a modulator layer linear loss that can be controlled by carrier injection of a low-wavelength laser diode.

First devices that were grown on GaAs substrates showed good mode locking properties, but did not have sufficient loss modulation to achieve the required modulation effect. Pump-probe measurements reveal that this failure is caused by a carrier lifetime in the modulation layer that is two orders of magnitude below the desired value. The short carrier lifetime is due to a high number of dislocations and stacking faults arising from the large lattice mismatch between the back-mirror and the modulator layer.

In order to increase the carrier lifetime in the active modulation layer, the design was modified to be grown perfectly lattice-matched on an InP-wafer. The active layers (modulation layer and saturable absorption layer) are grown lattice-matched to the substrate. In a subsequent processing step, a back-mirror is added *after* the growth of the functional layers has been completed. This decoupling of mirror deposition and active layer growth makes it significantly easier to obtain high quality material that provides for the desired modulation properties.

Modulation measurements with a two-color pump-probe setup (Figure 2, probe beam with 5 mW power at 1500 nm and pump beam with 100 mW power at 800 nm) exhibited approximately 0.3% of modulation depth over the desired frequency range of 100kHz to 10MHz with a flat phase (Figures 3 and 4). Numerical simulations of the laser dynamics reveal that an amount of modulation slightly exceeding the maximum saturable absorption will be sufficient for stabilizing the laser. Thus, the current modulator structure, driven by 200 mW pump light should be sufficient to reach the goal. Different structures for the modulator and quantum well building blocks of the device are under investigation and a number of fabrication methods of the back-mirror are

explored in collaboration with Prof. Amann's group at the Technical University of Munich, Germany.

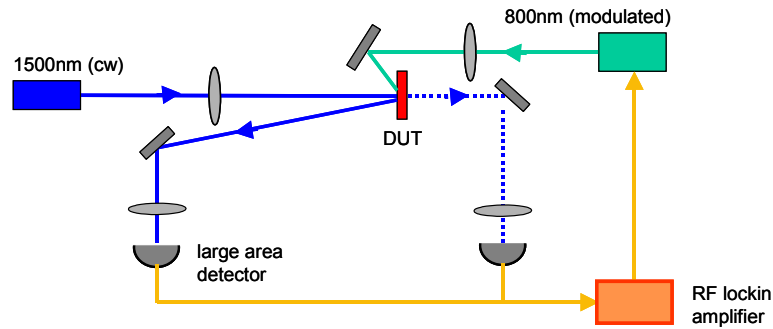


Figure 2. Two-color pump-probe setup for measurement of the linear modulation depth. A 1500 nm cw-laser beam is reflected from the device under test. The latter is modulated by a short wavelength laser diode (800 nm) that is driven by a lock-in amplifier. The lock-in technique allows detection of slightest changes in reflectivity. In addition, it allows determination of the frequency response of the DUT.

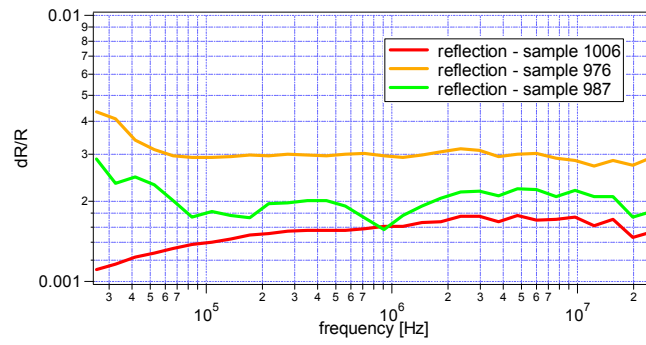


Figure 3. Amplitude response of the modified and lattice matched absorber-modulator device. With only 100mW incident pump power up to 0.3% modulation depth could be achieved over a wide frequency range.

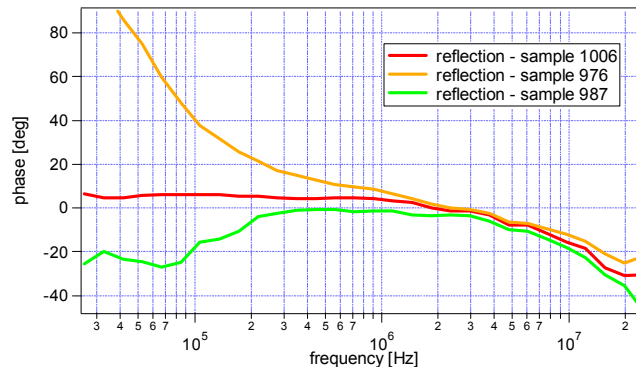


Figure 4. Phase response of the modified and lattice matched absorber-modulator device. In the relevant frequency range between 100kHz and 10MHz a sufficiently flat phase was observed.

References:

1. Schibli, T.R., T. Kremp, U. Morgner, F.X. Kaertner, R. Butendeich, J. Schwarz, H. Schweizer, and F. Scholz, "CW-operation and Q-switched mode locking of Cr:YAG-microchip lasers," *Opt. Lett.* 26, 148-150 (2001).
2. Schibli, T.R., U. Morgner, and F.X. Kaertner, "Control of Q-switched mode locking by active feedback," *Opt. Lett.* 26, 941 (2001).

Silicon-Germanium-based Semiconductor Saturable Absorbers for Laser Modelocking

Sponsors

National Science Foundation - ECS 03-22740

Air Force Office of Scientific Research - F49620-01-1-0084

Fonds Québécois de la Recherche sur la Nature et les Technologies, Canada

Project Staff

Felix J. Grawert, Shoji Akiyama, Juliet T. Gopinath, Hanfei Shen, Dr. Ömer Ilday, Professor Kazumi Wada, Professor Erich Ippen, Professor Franz X. Kaertner

Semiconductor Bragg reflectors (SBRs) based on III-V semiconductors have been used successfully over the last decade to mode lock lasers [1]. Here we describe a novel SBR based on the silicon/silicon-dioxide/germanium material system (Figure 1), which is directly compatible with silicon opto-electronics. In brief terms, our SBR structure offers three significant benefits over conventional absorbers based on III-V materials: (i) integrability, (ii) an unprecedentedly large operational bandwidth spanning 700 nm and (iii) large two-photon absorption (TPA) which facilitates suppression of Q-switching instabilities in high-repetition rate lasers [2,3].

The silicon/silicon-dioxide/germanium SBR essentially consists of a Bragg mirror and a saturable absorption layer that is placed at a peak of the resulting standing wave pattern (Figure 1). The high-index contrast Bragg mirror is formed of alternating SiO₂ and Si layers. The large difference of the refractive indices ($n_{\text{SiO}_2}=1.45$ and $n_{\text{Si}}=3.5$) allows achieving a record 99% bandwidth of over 700 nm with a peak reflectivity of 99.8% with only six layer pairs (Figure 2). In contrast, conventional SBRs made of the common III-V materials GaAs and AlAs require 22 layer pairs to achieve the same peak reflectivity, but provide only 90 nm of usable bandwidth (Figure 2). On top of the Si/SiO₂ Bragg mirror a germanium layer is embedded in a silicon layer of $3/4\lambda$ optical thickness. The germanium layer provides the saturable absorption. As can be observed in Figure 1, the germanium absorber layer is located at a peak of the standing wave pattern to maximize absorption, while the field decays rapidly upon further penetration in the mirror and barely reaches the lower part of the mirror structure

The fabrication of the SBR is described in Figure 3. The structure provides very high reflectivity and wide bandwidth. In addition, the structure provides a path with high thermal conductivity to the substrate and thus has an increased damage threshold. In contrast to other approaches aiming for wider bandwidth of the SBR [5,6] the chosen material system opens the way to future integration with compact integrated optical devices.

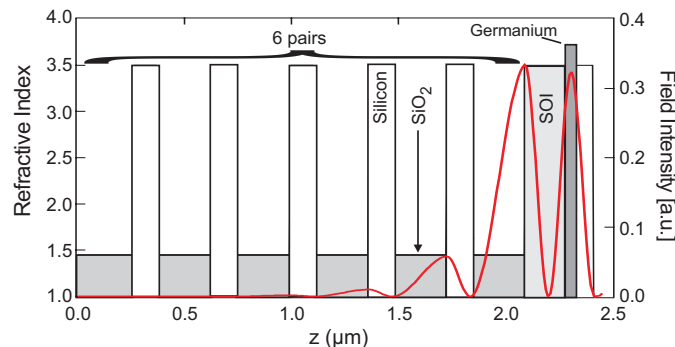


Figure 1. Refractive index profile and standing wave pattern of the SBR. The fields decays rapidly in the 6-pair Si/SiO₂ mirror due to the large index contrast. All interfaces are exposed to high field intensities and are created by thermal oxidation, reducing scattering loss. The Bragg mirror is terminated with an SOI layer that allows for subsequent growth of crystalline Germanium.

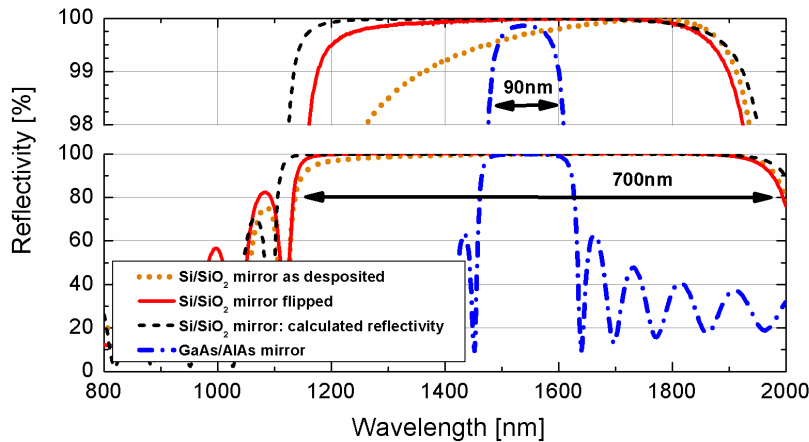


Figure 2. Calculated and measured reflectivity of the 6 pair Si/SiO₂ mirror and a 22 pair GaAs/AlAs mirror. The high-index contrast mirror (dash) has significantly larger bandwidth than the conventional semiconductor Bragg mirror (dash-dot). The high surface roughness on top of the mirror reduces the reflectivity in the short-wavelength range (dotted), but this problem is overcome by flipping the mirror upside down (solid) such that the highest quality layers are topmost.

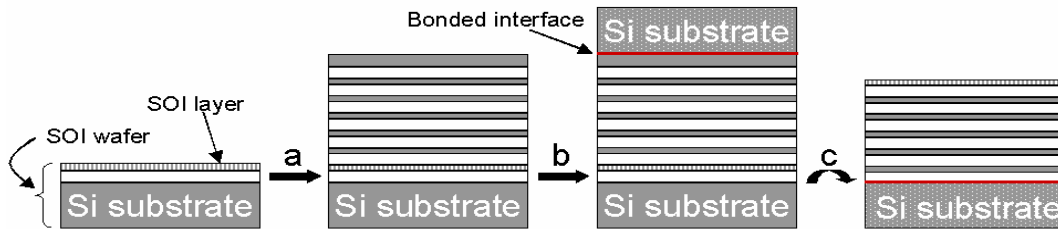


Figure 3 Fabrication process of the Si/SiO₂ mirror. **(a)** On an SOI wafer the 6 pair Si/SiO₂ Bragg mirror is built by repeated silicon deposition and wet oxidation. A thick silicon layer terminates the mirror. **(b)** The surface is planarized by CMP and a new silicon substrate is bonded atop. **(c)** The original substrate consisting of handle and buried oxide of the SOI wafer is removed by KOH and BOE etch. The crystalline SOI layer is now terminates the device allowing for deposition of further crystalline device layers.

References:

1. Keller, U., D.A.B. Miller, G.D. Boyd, T.H. Chiu, J.F. Ferguson and M.T. Asom, Solid-state low-loss intracavity saturable absorber for Nd:YLF lasers: an antiresonant semiconductor Fabry-Perot saturable absorber. *Opt. Lett.* 17, 505 (1992).
2. Thoen, E.R., E.M. Koontz, M. Joschko, P. Langlois, T.R. Schibli, F.X. Kaertner, E.P. Ippen and L.A. Kolodziejewski, Two-photon absorption in semiconductor saturable absorber mirrors. *Appl. Phys. Lett.* 74, 3927 (1999).
3. Schibli, T.R., E.R. Thoen, F.X. Kaertner and E.P. Ippen, Suppression of modelocked Q-switching and break-up into multiple pulses by inverse saturable absorption. *Appl. Phys. B* 70, 41 (2000).
4. S. Schoen, M. Haiml, U. Keller, Ultrabroadband AlGaAs/CaF₂ semiconductor saturable absorber mirrors, *Appl. Phys. Lett.* 77, 782 (2000).
5. Z.Zhang, T. Nakagawa, H.Takada, K. Torizuka, T. Sugaya, T. Miura, K. Kobayashi, Low-loss broadband semiconductor saturable absorber mirror for mode-locked Ti:sapphire lasers, *Opt. Commun.* 176, 171 (2000).

Ultrafast Phenomena and Quantum Electronics

Laser Micromachining of Photonic Devices in Transparent Materials

Sponsors

National Science Foundation – ECS-01-19452

Air Force Office of Scientific Research – F49620-01-01-0084

Project Staff

Andrew Martin Kowalewicz, Vikas Sharma, Professor James G. Fujimoto

Laser micromachining using femtosecond pulses is a powerful and versatile technique for fabricating photonic devices in transparent materials. It promises to enable high-density photonic structures, since multiple layers of waveguides can be fabricated on a single substrate. More importantly, it opens the door to a wide range of new devices fabricated in three-dimensional geometries, many of which provides enhanced functionality not possible in planar geometries. The micromachining process is very versatile and allows for rapid fabrication of a wide range of different devices under computer control. These devices can be designed, fabricated, and tested rapidly, thereby streamlining the device development process.

The direct writing of waveguides using femtosecond laser oscillators is attractive because the cumulative effects of high-repetition-rate pulses, as well as the cumulative heating that results when the intrapulse arrival time is shorter than the thermal diffusion time, enables device fabrication approximately three orders of magnitude faster than using amplified lasers (mm/s versus $\mu\text{m/s}$). In most studies to date, however, the typical pulse energy available from laser oscillators (~ 10 nJ) necessitates focusing with very high numerical aperture (NA) objectives and oil immersion in order to reach intensities sufficient to initiate the nonlinear interaction. This requirement severely limits available working distance and the ability to machine at depth in materials. We have developed an extended cavity Ti:Sapphire laser capable of generating 150 nJ pulses [1] that overcomes the restriction to very high NA objectives, thus giving greater flexibility and versatility to the machining process.

Recent work on photonic device fabrication in transparent materials using femtosecond pulses has enabled the creation of a wide variety of devices. Two-dimensional devices, such as X and directional couplers [2-5], gratings [6,7], interferometers [7,8], as well as active waveguides [9], have been demonstrated. While three-dimensional couplers have been demonstrated with amplified femtosecond lasers [10,11], oscillator machining has been limited to basic three-dimensional waveguides spaced over several tens of microns [5].

Here, we present the research in the area of device fabrication in transparent materials using femtosecond laser oscillators. We begin by demonstrating the fabrication of simple waveguides and determine their index and loss characteristics. Using these waveguides, elemental two-dimensional photonic devices are fabricated, in particular, directional couplers and X-couplers. Using a broadband source the spectral dependence arising from the wavelength-dependent coupling is demonstrated for the fabricated directional couplers and, in contrast, the flat and broadband width response (wavelength independence) is demonstrated for the fabricated X-couplers. More complex two-dimensional structures are possible using multiple couplers. Using two X-couplers fabricated back-to-back, a Mach-Zehnder interferometer is constructed.

Finally we demonstrate the ability to produce three-dimensional structures, which is one of the most attractive features of this fabrication technique. By changing the depth of the focal spot within the substrate, three-dimensional waveguides are fabricated. Next, by creating multi-layered two-dimensional structures, the capacity to achieve a high device density is shown. Beyond structural density, three-dimensional fabrication allows for devices with functions and geometries that are not possible in two dimensions (planar geometries). As a initial example, we demonstrate a 1-to-4 coupler. Next, we combine a horizontally oriented X-coupler with a

vertically oriented directional coupler to deliver different spectral components to different levels of the substrate. And lastly, utilizing the full dimensional freedom allowed by this technique, we fabricate a symmetric three-waveguide directional coupler and demonstrate its performance.

Waveguides

By changing the exposure parameters, a wide range of waveguide sizes and index variations are possible. Figure 1 shows a phase contrast image of 7 waveguides. All waveguides were written using an effective ~ 0.80 NA and by translating the glass substrate at 10 mm/s. Waveguide diameters ranging from 2.1 μm to 9.0 μm are possible by varying the incident pulse energy from 10 nJ to 40 nJ. Similar variations in waveguide size can be achieved by keeping the incident pulse energy constant and changing the speed of translation. In this case, larger waveguides result from slower feed rates. For the best balance of reproducibility, control, and speed, we determined on a feed rate of 10 mm/s with an incident power of ~ 85 mW, which gives a pulse energy of ~ 15 nJ.

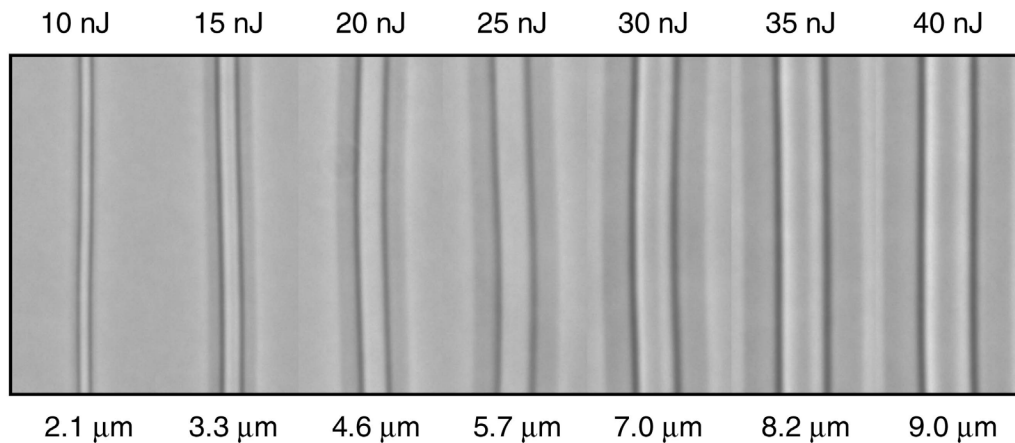


Figure 1. Phase contrast images of different waveguide sizes possible under different exposure conditions. Incident pulse energy is shown at the top of each image with the corresponding waveguide diameter shown below. All waveguides were fabricated with about 0.80 NA and 10 mm/s scan rate.

In order to estimate the refractive index change in the fabricated waveguide, we performed a V-number analysis assuming a step-index structure (even though a graded index profile may be present) and found $\Delta n = 5 \times 10^{-3} - 8 \times 10^{-3}$.

The attenuation of transmitted power in the waveguides is caused by several factors, but can be attributed to two major effects: absorption and scattering. Using a cut-back loss measurement technique the loss for straight waveguides was found to be 1.64 dB/cm at 800 nm. (Variations in the geometry and bending of the waveguides can produce additional attenuation.)

Two-Dimensional Photonic Devices

Using single mode waveguides, we created a variety of photonic devices. In this section, we demonstrate wavelength-dependent devices, a directional coupler and a Mach-Zehnder interferometer, and an X-coupler that results in tunable power coupling that is nearly wavelength independent. Since single wavelength characterization has been previously reported, here we will present broad bandwidth performance.

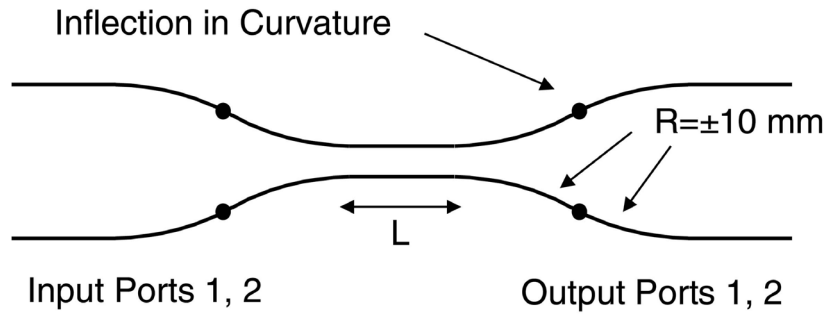


Figure 2. Schematic of a symmetric directional coupler. Circular paths with a radius 10 mm are used to bring the waveguides together for an interaction length L .

A schematic of the fabricated directional couplers is shown in Figure 2. The bends are curved waveguides of 10 mm radius in an attempt to reduce loss. The couplers are fabricated with a waveguide separation, d , of $5 \mu\text{m}$ for each of the four different interaction lengths ranging from 1.0 mm to 2.5 mm in equal increments.

In order to evaluate the wavelength dependence of the device, the output from a mode-locked femtosecond laser is measured using a spectrometer to serve as the reference spectrum for the characterization. The broadband light is then coupled into each of the two input ports of the directional coupler, and a measurement is performed on the wavelength-dependent output. Multiple measurements are used to construct two average spectra: a “through” spectrum, which is the average of P_{11} and P_{22} , and a “cross” spectrum, which represents the average of P_{12} and P_{21} .

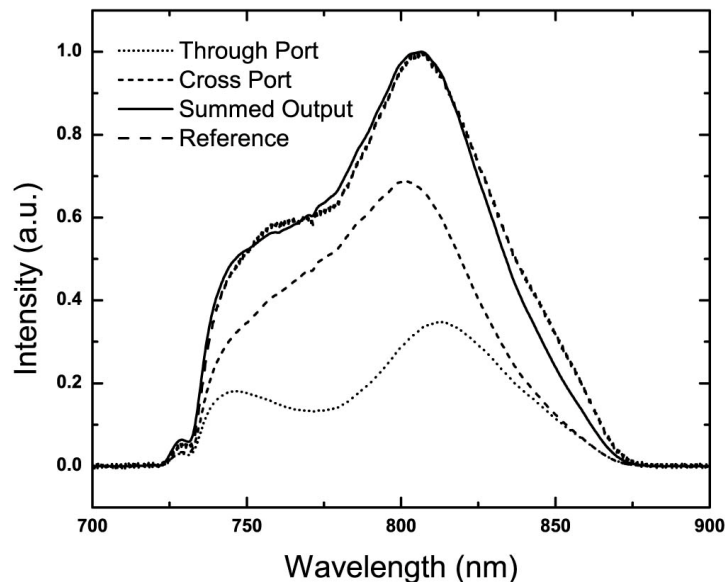


Figure 3. Plot of the output spectra of the cross and through ports of the coupler. Their sum shows excellent agreement with the reference spectrum.

Figure 3 shows the spectral output of a representative directional coupler with $L = 1.5$ mm. The through port and cross port outputs are plotted along with their sum. Due to the wavelength-dependent coupling coefficient, the two output spectra are different, but their sum is in agreement with the reference spectra. With further analysis, we confirmed that, for the shorter wavelengths, which have a higher coupling coefficient, an increased interaction length resulted in an increased transfer of power in the blue components, as compared to the red components.

Current technology uses directional couplers or variations thereof to produce 1-to-N splitters or couplers of varying ratios. Unfortunately, because of the wavelength dependent coupling, it is often difficult or impossible to achieve a uniform transfer of power over any significant spectral width. By using nonlinear fabrication techniques, it is possible to fabricate couplers that have a nearly wavelength-independent transfer of power.

In order to demonstrate this capability, a number of X-couplers were fabricated. The X-couplers were composed of two crossed single-mode waveguides. In order to tailor the power transferred from one waveguide to the other, X-couplers with crossing angles ranging from 1.00° to 1.75° in 0.25° increments were fabricated. The devices were then evaluated using a broad spectral source in an analogous fashion to the characterization of the directional couplers discussed earlier.

Figure 4 shows the spectral data for an X-coupler with a crossing angle of 1.25° . The through port and cross port outputs are plotted, along with their sum, which is in agreement with the reference spectrum. The similarity in appearance of the two outputs confirms the wavelength-independent power splitting of the X-coupler. The power splitting ratio that results can be tuned by changing the crossing angle.

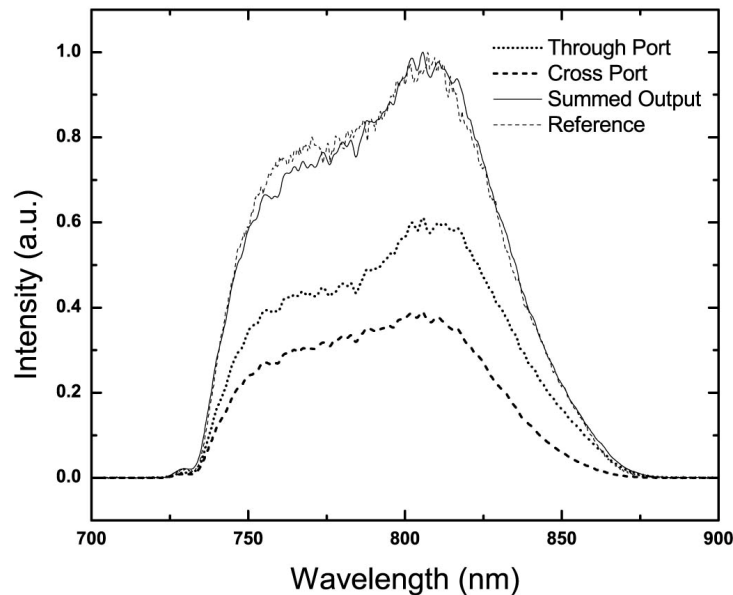


Figure 4: Plot of the output spectra of the cross and through ports of an X-coupler with a 1.25° crossing angle. The similar shape of both spectra in comparison to the reference spectrum suggests wavelength-independent coupling.

Our experiments show that as the crossing angle increases from 1.25° to 1.50° , and further to 1.75° , the coupling ratio changes from $\sim 60/40$ to $\sim 80/20$ to $\sim 90/10$, with less power transferred from the input guide to the output guide. Based on the results, an equal 50/50 power splitter should be achievable using a crossing angle between 1.00° and 1.25° .

Using multiple couplers in series, more functionally useful devices can be demonstrated. As an example of a more complex photonic device, we fabricated a Mach-Zehnder interferometer consisting of two X-couplers placed back-to-back with crossing angles of 2° [8]. This device was reported previously.

Three-Dimensional Machining

As we have mentioned, one of the advantages that laser micromachining in transparent materials offers is the ability to utilize the full three dimensions of the substrate. In comparison to planar geometries, three-dimensional fabrication techniques allow for greatly increased device density and promises enhanced functionality. In addition, the greater freedom of three-dimensional geometry permits the fabrication of devices not possible in two-dimension.

The ability to fabricate structures at various depths in the material is an important capability for efficient use of space. While oscillator machined three-dimensional waveguides were previously demonstrated [5], the structures were contained within a depth of about $100\ \mu\text{m}$. By using a specially designed objective we have demonstrated the capability to machine waveguides through the entire $1\ \text{mm}$ substrate thickness. The objective used in the study had a $0.80\ \text{NA}$ with approximately $1.5\ \text{mm}$ of working distance in glass. The objective was designed to correct for variable cover glass thicknesses. This allowed for diffraction limited focusing over the full depth of the substrate.

By vertically stacking standard two-dimensional devices, it is possible to create parallel architecture not possible in a planar geometry. Because there is no linear absorption, and material modification occurs only at the focal spot, waveguides can be fabricated in any order without affecting previously existing structures.

To demonstrate this capability and to take advantage of the full freedom that the third dimension offers, we fabricated a 1-to-4 waveguide coupler. Figure 5 (a) shows a schematic of the device. It is composed of multiple X-couplers oriented in orthogonal planes to divide the power of the incoming beam. The device has a single input port with four output ports at three separate depths within the glass.

The operation of the device was tested using $800\ \text{nm}$ light. The output of the 1-to-4 three-dimensional coupler is shown in inverted gray scale in Figure 5 (b). The slightly varying intensities are likely due to minor imperfections in the movement of the stages during the writing of the approximately $2.6\ \mu\text{m}$ waveguides used in this device.

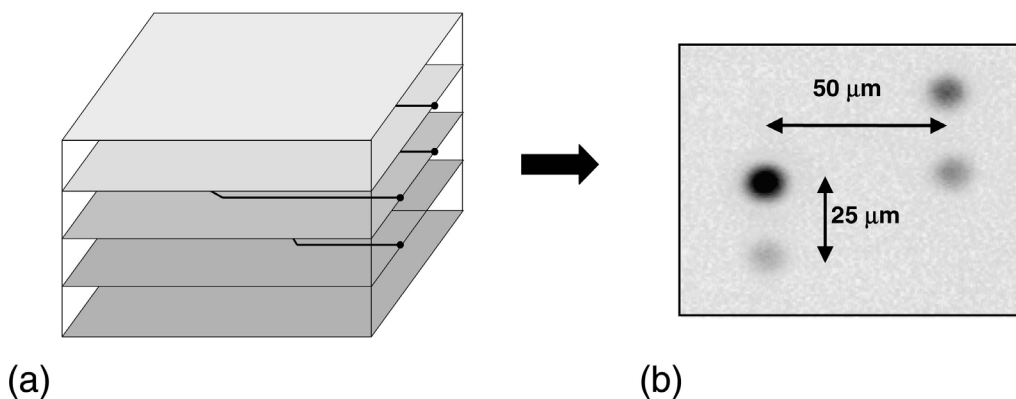


Figure 5. (a) Schematic of the 1-to-4 three-dimensional waveguide coupler with outputs on three separate levels of the substrate. (b) CCD image of the output modes from the waveguides; the output ports are separated by $50\ \mu\text{m}$ along the x-axis and $25\ \mu\text{m}$ along the z-axis.

Instead of using only X-couplers to divide the power into multiple output ports, different types of couplers can be used. By using a combination of X and directional couplers, power division and wavelength filtering can be performed. Finally, different spectral components can be transmitted to various layers at the output. Figure 6 (a) shows the schematic of a device with a horizontally oriented broad bandwidth coupler and a vertically oriented directional coupler that we have fabricated. In order to test the spectral performance of the device, the output from a mode-locked femtosecond laser was used.

Figure 6 (b) shows a normalized comparison of the reference spectrum and the output spectrums. The agreement of the broadband width spectra demonstrates a nearly flat coupling over the full 150 nm of the input light source. The other branch of the X-coupler is directed through a directional coupler oriented along an orthogonal plane. The outputs of the top and bottom guides are shown in Figure 6(b), which are normalized to the output of the broad bandwidth port. Since the directional coupler has a wavelength dependant coupling, it is possible to divide the spectral components between the two output ports, thus sending the longer wavelengths to the upper output and the shorter ones to the lower port. The ratio of the power between the broadband output port and the sum of the two directional coupler ports is 4:3, indicating a nearly symmetric power splitting between the two arms of the device. Other coupling ratios can be achieved by changing the crossing angle of the waveguides composing the X coupler.

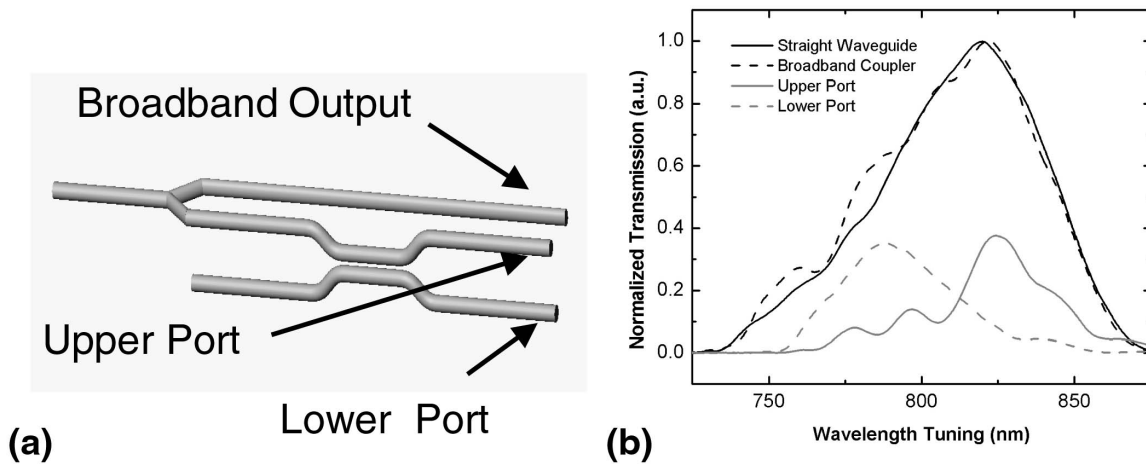


Figure 6. (a) Schematic of the device with a broad bandwidth X-coupler in the horizontal plane, and a directional coupler in the vertical plane. (b) Spectral comparison of the different output ports of the device demonstrating both wavelength division capability and broadband coupling.

Finally we demonstrate a three-waveguide directional coupler. In an analogous fashion to conventional directional couplers, where two identical guides interact via mode-coupling, three-dimensional machining allows for the creation of a three-waveguide directional coupler. Figure 7(a) shows the schematic of the device that was constructed. The geometry requires a symmetry that is not possible in planar configurations. The waveguides were fabricated on the edges of an equilateral triangle. The initial and final side lengths of 50 μm correspond to the center-to-center waveguide separation. In order to enable mode-coupling, the path of each waveguide was directed toward the corresponding vertex of an equilateral triangle, 5 μm on each side, by equal bending angles of 1.2°. The power transfer between the guides can be tailored by varying the interaction length, L, during which the waveguides are at their minimum separation.

Figure 7(b) shows a CCD image in inverted gray scale of a coupler with a 2.00 mm interaction length. The output port of the input guide maintains 43% of the total power, with the remaining 28% and 29% being transferred to the upper right and left outputs, respectively. Coupling ratios can be controlled using different fabrication parameters although a complete transfer has not yet been obtained. Further improvements in the fabrication process, including a more uniform sample translation along non-orthogonal stage directions should allow for a greater fraction of the light to be transferred between the three waveguides.

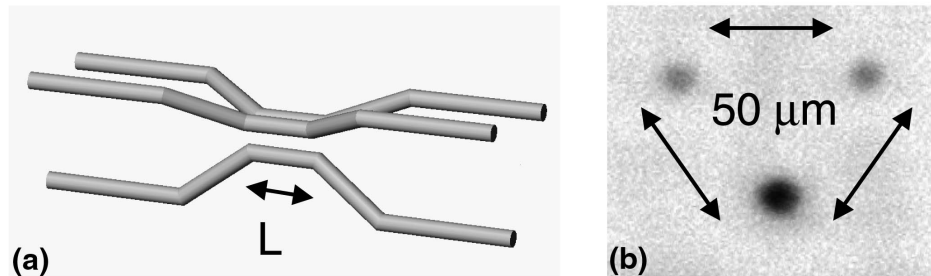


Figure 7. (a) Schematic of the symmetric three-waveguide directional coupler. Waveguides are separated by $50\ \mu\text{m}$ at the ends and $5\ \mu\text{m}$ in the interaction region, L . (b) Inverse gray-scale CCD image of the waveguide outputs.

References

1. A.M. Kowalewicz, A.T. Zare, F.X. Kartner, J.G. Fujimoto, S. Dewald, U. Morgner, V. Scheuer, and G. Angelow, "Generation of 150-nJ pulses from a multiple-pass cavity Kerr-lens mode-locked Ti:Al₂O₃ oscillator," *Optics Letters* 28(17): 1597-1599 (2003).
2. D. Homoelle, S. Wielandy, A.L. Gaeta, N.F. Borrelli, and C. Smith, "Infrared photosensitivity in silica glasses exposed to femtosecond laser pulses," *Optics Letters* 24(18): 1311-1313 (1999).
3. C.B. Schaffer, A. Brodeur, J.F. Garcia, and E. Mazur, "Micromachining bulk glass by use of femtosecond laser pulses with nanojoule energy," *Optics Letters* 26(2): 93-95 (2001).
4. A.M. Streltsov and N.F. Borrelli, "Fabrication and analysis of a directional coupler written in glass by nanojoule femtosecond laser pulses," *Optics Letters* 26(1): 42-43 (2001).
5. K. Minoshima, A.M. Kowalewicz, I. Hartl, E.P. Ippen, and J.G. Fujimoto, "Photonic device fabrication in glass by use of nonlinear materials processing with a femtosecond laser oscillator," *Optics Letters* 26(19): 1516-18 (2001).
6. Y. Kondo, K. Nouchi, T. Mitsuyu, M. Watanabe, P.G. Kazansky, and K. Hirao, "Fabrication of long-period fiber gratings by focused irradiation of infrared femtosecond laser pulses," *Optics Letters* 24(10): 646-648 (1999).
7. C. Florea and K.A. Winick, "Fabrication and characterization of photonic devices directly written in glass using femtosecond laser pulses," *Journal of Lightwave Technology* 21(1): 246-253 (2003).
8. K. Minoshima, A.M. Kowalewicz, E.P. Ippen, and J.G. Fujimoto, "Fabrication of coupled mode photonic devices in glass by nonlinear femtosecond laser materials processing," *Optics Express* 10(15): 645-652 (2002).
9. Y. Sikorski, A.A. Said, P. Bado, R. Maynard, C. Florea, and K.A. Winick, "Optical waveguide amplifier in Nd-doped glass written with near-IR femtosecond laser pulses," *Electronics Letters* 36(3): 226-227 (2000).
10. W. Watanabe, T. Asano, K. Yamada, and K. Itoh, "Wavelength division with three-dimensional couplers fabricated by filamentation of femtosecond laser pulse," *Optics Letters* 28: 2491-2493 (2003).
11. S. Nolte, M. Will, J. Burghoff, and A. Tuennermann, "Femtosecond waveguide writing: a new avenue to three-dimensional integrated optics," *Appl. Phys. A* 77(1): 109-111 (2003).

Laser Cooling with Ultrafast Pulse Trains

Sponsors

Air Force Office of Scientific Research F49620-03-1-0313
Pappalardo Fellowship

Project Staff

Blaise Gassend, Zilong Chen, Dr. David Kielpinski, Prof. Franz X. Kaertner

Laser cooling and trapping are central to modern atomic physics. The low temperatures and long trapping times now routinely achieved by these means have led to great advances in precision spectroscopy and ultracold chemistry studies, and provide a suitable starting point for evaporative cooling to Bose-Einstein condensation. However, laser cooling is restricted to less than 20 atomic species, mostly the alkali and alkali-earth metals and the metastable states of noble gases. Laser cooling with ultrafast pulses offers a way to cool a wide variety of other atomic species [1]. This project, developed in collaboration with the Center for Ultracold Atoms (CUA) at MIT, aims to implement this cooling scheme initially with trapped ytterbium ions, and later with neutral hydrogen atoms.

Two-Photon Cooling with Mode-Locked Lasers

Mode-locked lasers provide the sharp frequency selectivity of single-frequency lasers along with great versatility in optical frequency synthesis. The stable repetition rate of the laser pulses gives rise to a series of sharp lines in the frequency domain. These lines are narrow enough ($\ll 1$ MHz) for laser cooling and precision spectroscopy. The lines also cover a wide range of frequencies, up to a full octave in extreme cases [2], and these lines each can be used to drive separate atomic transitions [1]. At the same time, the high peak powers of the pulses enable efficient and straightforward nonlinear frequency conversion deep into the ultraviolet, with much higher power than that available by conversion of single-frequency lasers.

These advantages let us address the two major obstacles to laser cooling of arbitrary atomic species. First, the lowest energy transitions of many atoms, notably hydrogen, lie in the vacuum ultraviolet. Not enough laser power is available in this spectral region to drive effective laser cooling. Second, the complex level structure of many atoms (and all molecules) permits decay of an excited electron into a number of metastable levels widely separated in energy. Each metastable decay channel must typically be repumped by a separate laser, so the laser system becomes unwieldy.

Proof of Principle with Trapped Ytterbium Ions

Initially we wish to demonstrate this scheme with trapped ytterbium ions (Yb^+), which have been extensively studied for atomic clocks [3]. The spectroscopic and laser-cooling properties of Yb^+ are well understood. The extremely deep traps ($> 10,000$ K) available for ions will permit us to produce and trap the ions without cooling, so that we can detect even very weak cooling forces. The level structure of Yb^+ offers a two-photon transition in the infrared, so that we can cool directly with the output of a mode-locked Ti:sapphire laser.

Over the past year, we have constructed an ion trap apparatus for radiofrequency trapping of Yb^+ (Fig. 1). The trap consists of two electrodes, the so-called ring and fork. Applying several hundred volts at 15 MHz provides a stable trapping potential for several thousand Yb^+ ions. The ions are produced by bombarding a beam of neutral Yb with electrons. The whole apparatus is evacuated to ultrahigh vacuum to avoid heating of the ions by collision with background gas. We are

currently attempting to detect ions in the trap by fluorescence from frequency-doubled mode-locked laser light resonant with the single-photon Yb⁺ transition at 369.5 nm.

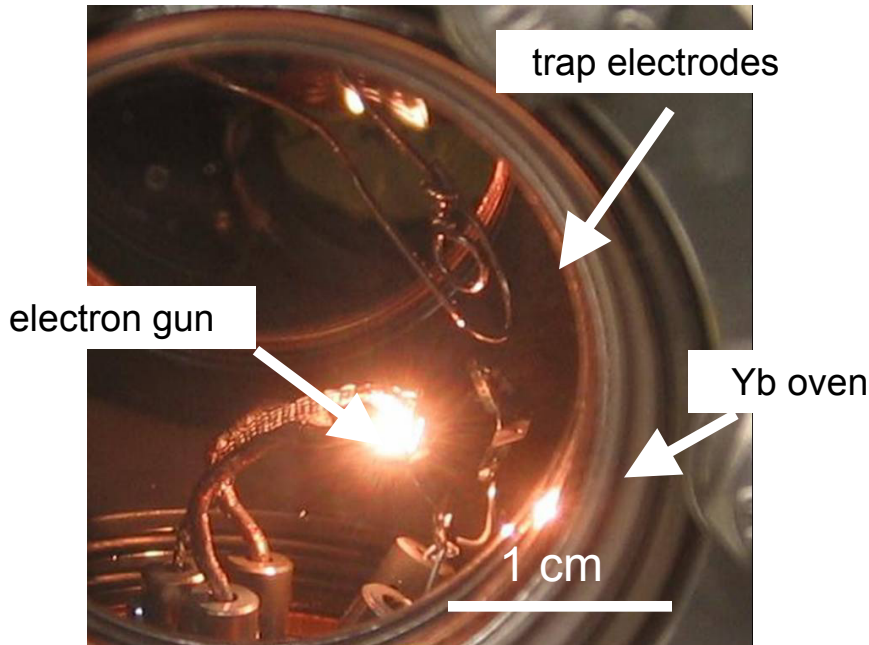


Figure 1. Apparatus for trapping Yb⁺. Several hundred volts at 15 MHz are applied across the trap electrodes. The Yb oven produces a beam of neutral Yb, which is ionized by the electron gun. An ultra-high vacuum chamber contains the apparatus.

Development of High-Repetition-Rate Ti:sapphire Laser for Mode-Locked Cooling

Efficient two-photon laser cooling requires a mode-locked laser with high average power and high repetition rate. Because of the small two-photon cross section, at least a watt of average power is desirable to achieve a high scattering rate and thus large cooling forces. Since laser cooling depends on velocity-selective scattering via the Doppler shift, we also need a repetition rate larger than the initial Doppler-broadened line-width of the atomic sample – otherwise the laser can heat, as well as cool, the atoms. Commercial mode-locked lasers cannot supply the combination of 1 GHz repetition rate and 1 W average power. However, we can accept relatively long pulses of a few hundred fs, easing our design constraints somewhat. We are currently building a mode-locked Ti:sapphire laser to fulfil these requirements. So far we have mode-locked a 500 MHz laser at 800 nm using a semiconductor saturable absorber, and have incorporated a birefringent filter for tuning to the relevant Yb⁺ transition at 871 nm. We have also operated another laser with Kerr-lens mode-locking at 871 nm, with 360 MHz repetition rate and 100 mW output power. We expect the power and repetition rate to increase to our design values by employing an optimized semiconductor saturable absorber.

References:

1. D. Kielpinski, "Laser cooling with ultrafast pulse trains," <http://xxx.lanl.gov/abs/quant-ph/0306099>
2. R. Ell, U. Morgner, F.X. Kaertner, J.G. Fujimoto, E.P. Ippen, V. Scheuer, G. Angelow and T. Tschudi, "Generation of 5 fs pulses and octave-spanning spectra directly from a Ti:sapphire laser," *Opt. Lett.* 26(6): 373-5 (2001).
3. H.A. Klein, A.S. Bell, G.P. Barwood, and P. Gill, "Laser cooling of trapped Yb⁺," *Appl. Phys. B* 50, 13 (1990).

Carrier-Envelope Phase Detection

Sponsors

Office of Naval Research - N00014-02-1-0717

Air Force Office of Scientific Research - F49620-01-01-0084

Project Staff

Christian Jirauschek, Dr. Lingze Duan, Professor Franz X. Kaertner

With the arrival of laser pulses consisting of only few optical cycles, attention has been drawn to effects which not only depend on the electric field envelope, but also on the phase between the rapidly oscillating carrier wave and the envelope. Various approaches have been used for detecting this carrier-envelope (CE-) phase Φ_{CE} . Here, we show that excitation of a two-level system may lead to a phase sensitive inversion after passage of the pulse. This effect can be observed when the Rabi frequency approaches the carrier frequency. In this regime, carrier-wave Rabi flopping occurs, i.e., the excitation of a two-level system is so strong, that significant inversion is generated during one optical cycle [1]. The phase sensitive inversion can be directly probed optically or it can be read out electronically by an applied field, resulting in a compact electronic phase detector.

We assume excitation by sinc-shaped pulses with a full-width at half-maximum (FWHM) pulse duration T , a carrier frequency $\omega_0=2\pi f_0$ and a maximum field strength E_{max} occurring at the center of the pulse for vanishing CE-phase. Those pulses are a fairly good description of recently generated few-cycle laser pulses. The two-level medium is described by its resonance frequency $\omega_{ba}=(E_b-E_a)/\hbar$, dipole matrix element d and dephasing time T_2 ; energy relaxation processes are assumed to be negligible for the time scales considered.

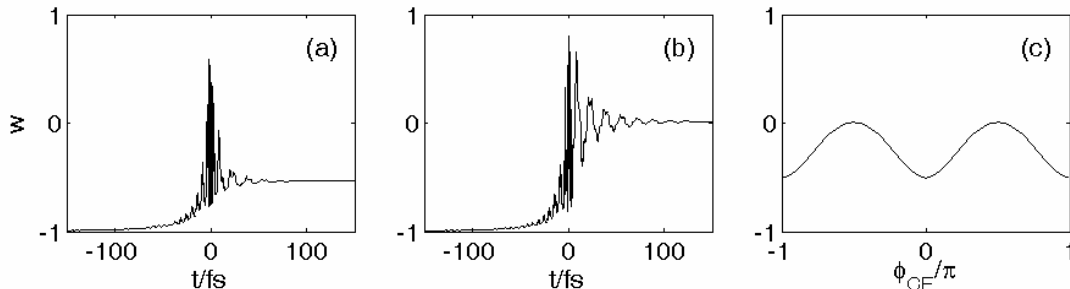


Fig. 1: Inversion w in a two-level system with $\omega_{ba}=3.28/\text{fs}$, $d=0.4e$ nm and $T_2=40$ fs, for excitation by a 5 fs pulse with $E_{max}=6$ V/nm and $f_0=375$ THz (i.e., $\lambda_0=800$ nm): (a) time evolution for $\varphi_{CE}=0$, (b) time evolution for $\varphi_{CE}=-\pi/2$, (c) phase dependence of the remaining inversion.

The dynamics of the two-level system is found by numerically solving the Bloch equations. As an example, we compute the inversion in a two-level system, interacting with a sinc pulse. Figs. 1 (a) and (b) show the evolution of the inversion w for excitation with a $\varphi_{CE}=0$ and $\varphi_{CE}=-\pi/2$ pulse respectively. In Fig. 1(c), the CE dependence of the stationary value, reached after interaction with the pulse, is displayed. The remaining inversion is modulated with twice the CE-frequency since the Bloch equations are invariant with respect to simultaneous inversion of the electric field and the dipole moment, leaving the inversion invariant.

Fig. 2 shows the modulation depth, defined as $\delta=(w_0-w_{-\pi/2})/(w_0+w_{-\pi/2}+2)$, for single- and two-cycle pulses as a function of the Rabi frequency $\Omega_R=dE_{max}/\hbar$ and resonance frequency ω_{ba} [2]. The phase relaxation time is set to $T_2f_0=18.75$. A value of $\delta =\pm 1$ indicates maximum possible modulation of the inversion, $\delta=0$ indicates no modulation. High sensitivity of the inversion with respect to the CE-phase is found for off-resonant excitation and strong excitation, i.e., the Rabi frequency is a considerable fraction of the carrier frequency.

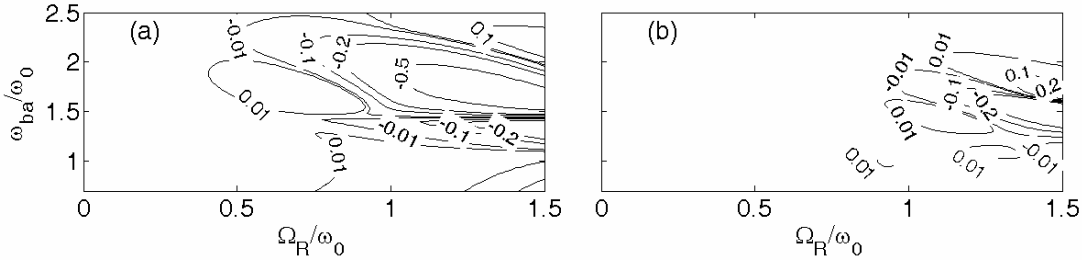


Fig. 2: Modulation depth δ as a function of the Rabi frequency Ω_R and the transition frequency ω_{ba} in units of ω_0 , for $T_2f_0=18.75$. Displayed is δ after interaction with (a) single-cycle pulses, (b) two-cycle pulses.

The calculations can be extended to a two-band semiconductor model. The interaction with the electric field is described by the semiconductor Bloch equations, the Coulomb interaction among carriers and propagation effects are neglected. Our model includes energy-dependent dipole moments and dephasing rates. For the energy bands, we choose the highest valence band and the conduction band of GaAs or respectively InGaP, obtained with a tight-binding method. $\Omega_g = d_g E_{\max} / \hbar$ is the Rabi frequency at the Γ point, with the maximum field strength E_{\max} and the dipole matrix element d_g .

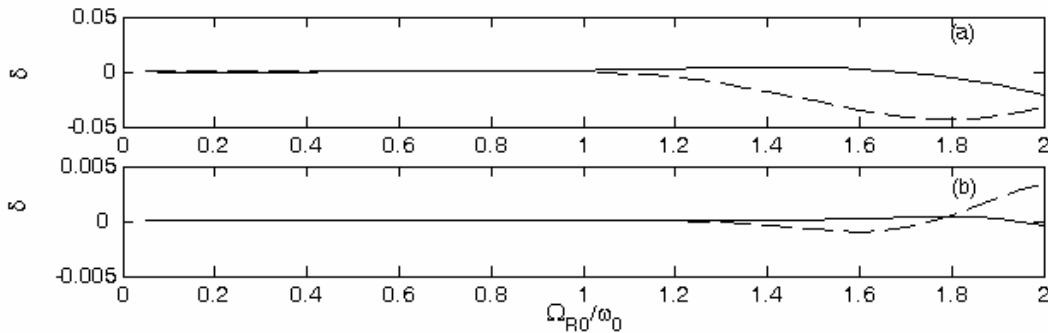


Fig. 3: Modulation depth δ in GaAs (solid line) and InGaP (dotted line) for (a) single-cycle and (b) two-cycle pulses.

Fig. 3 shows the modulation depth, which is for a semiconductor defined as $\delta = [N(0) - N(-\pi/2)] / [N(0) + N(-\pi/2)]$, where $N(\varphi_{CE})$ is the total number of electron-hole pairs after the pulse [3]. The modulation depth is greatly reduced in the semiconductor, compared to a two-level system. The reason for this is that only the near-band-gap transitions contribute to the phase signal. The population of the higher-lying states is phase-insensitive, mainly because of the increased dephasing for higher energies.

The inversion could be detected optically in a pump-probe experiment. It is even more appealing to read out the inversion electronically by an applied bias voltage, resulting in a compact electronic phase detector. Experimental investigations of these possible novel electronic phase detection schemes are in progress. Increased phase sensitivity can be expected from materials that come closer to two-level systems than a semiconductor, i.e., have narrower energy bands and in particular a smaller dephasing, e.g., artificial materials like superlattices and quantum dots.

References:

1. O. D. Mücke, T. Tritschler, M. Wegener, U. Morgner, and F. X. Kaertner, "Signatures of Carrier-Wave Rabi Flopping in GaAs," *Phys. Rev. Lett.* **87**, 057401 (2001).
2. C. Jirauschek, J. Chandalia, L. Duan, F. X. Kaertner, O. D. Mücke, T. Tritschler, and M. Wegener, "Opto-Electronic Carrier-Envelope-Phase Detection," IEEE LEOS SUM 2003, TuC2.3.
3. C. Jirauschek, L. Duan, O. D. Mücke, F. X. Kaertner, Klaus D. Hof, T. Tritschler, and M. Wegener, "Semiconductor-based carrier-envelope phase detector," CLEO 2004, JTUB2.

Third-order nonlinearities in chalcogenide glasses suitable for high-index contrast fiber devices

Sponsors

National Science Foundation, Omniguide Corporation

Project Staff

J. T. Gopinath, M. Soljačić, E. P. Ippen, V. N. Fufluyigin, W. A. King, and M. Shurgalin

Ultrafast all-optical switching will be required in the future for high-capacity optical communication systems. Such an all-optical switch can be implemented using the intensity-dependent phase shift caused by the Kerr effect. Chalcogenide glasses, which are easier to fabricate than single crystal semiconductor waveguides, have large values of nonlinearity at 1.55 μm . Many such glasses have been investigated in previous work [1]. Our studies focus on glasses with particular promise for fabrication into high-index-contrast highly nonlinear fiber for 1.55 μm applications. The glasses must have a glass transition and softening temperature compatible with that of lower index glasses in order to draw fiber. We have investigated several glasses with relatively high glass transition temperatures, suitable for these applications: $\text{Ge}_{33}\text{As}_{12}\text{Se}_{55}$, $\text{Ge}_{35}\text{As}_{15}\text{Se}_{50}$, $\text{Ge}_{25}\text{As}_{10}\text{Se}_{65}$, and $\text{Ge}_{22}\text{As}_{20}\text{Se}_{58}$.

A z-scan setup was used to characterize the nonlinear refractive index and two-photon absorption coefficients of these glasses. An optical parametric oscillator (OPO), producing 150 fs pulses at a repetition rate of 82 MHz, was used as the source. The experimental setup is shown in Figure 1. The OPO output beam is coupled through 3 cm of standard single mode silica fiber (SMF), for spatial filtering. It is then recollimated and focused onto the sample. To measure n_2 , an aperture is placed after the sample (closed-aperture scan), and a lens images the apertured spot onto a large area Ge photodiode. This output was analyzed with a lock-in amplifier and a computer. To measure the two-photon absorption coefficient, the aperture after the sample is removed (open-aperture scan). To account for inhomogeneities in the samples, traces at attenuated intensities were also taken and subtracted from the high intensity scans. Since the repetition rate of the OPO is high, thermal lensing can affect the measurement of n_2 . To separate the thermal effects from those of the nonlinear index of refraction, the 3 cm of SMF was replaced with 50 cm of dispersion compensating fiber (DCF), which broadened the pulses to 1.5 ps. Additionally, a pump-probe technique was used to verify some of the values obtained for the two-photon absorption coefficient, as the sensitivity of this measurement is higher than that of the z-scan.

The samples studied were 3 mm thick windows with parallel faces, polished to optical quality. Figures 2 and 3 show typical open- and closed-aperture traces. At 1540 nm, the nonlinear refractive index of $\text{Ge}_{33}\text{As}_{12}\text{Se}_{55}$ was measured to be $1.5 \times 10^{-13} \text{ m}^2/\text{W}$ +/- 25% and the two-photon absorption coefficient, 0.4 cm/GW +/- 25% [2,3]. Thermal effects were checked for by comparing results obtained using 1.5 ps pulses with the short pulse results. No evidence of thermal effects for any of the glasses are seen in the data. The results are summarized in the table below.

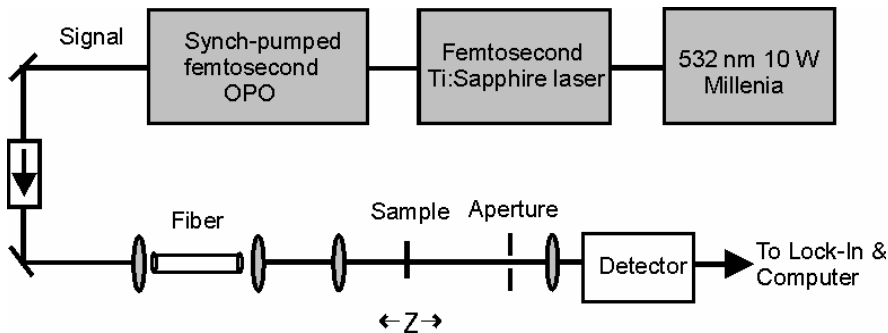


Fig. 1. Experimental setup for zscan measurements.

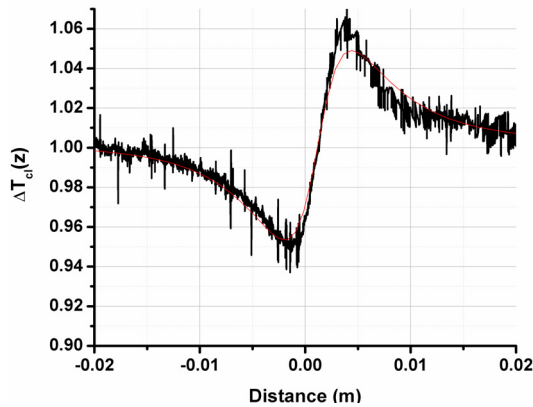


Fig. 2. Transmission vs. position for a closed aperture scan of $\text{Ge}_{33}\text{As}_{12}\text{Se}_{55}$.

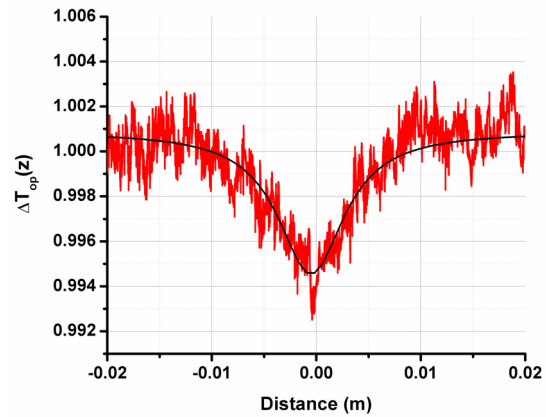


Fig. 3. Transmission vs. position for an open aperture scan of $\text{Ge}_{33}\text{As}_{12}\text{Se}_{55}$.

From the table, the value of n_2 ranges from 200x to ~900x the value of silica at $1.54 \mu\text{m}$. One of the best values reported for other chalcogenide glasses is 500x that of the value of silica, but the glass transition temperature is quite low (As_2Se_3 188C) [1]. A small variation in composition has a large effect on n_2 , but the value of β and the bandedge are less sensitive to composition. As more germanium is added to the samples, the glass transition temperature increases as well as the nonlinear refractive index, making the glass more favorable for fiber-based applications. The bandgap also shifts to longer wavelengths. However, too much germanium causes crystallization in the glasses. The nonlinear figure of merit, $n_2/\beta\lambda$, is approximately 3.2 for $\text{Ge}_{35}\text{As}_{15}\text{Se}_{50}$, the highest value reported for glasses that can be codrawn into fiber with low index glasses (such as fluoride and oxide glasses).

| Material | Bandgap* +/- 20 nm | n_2 ($\times 10^{-18} \text{ m}^2/\text{W}$) +/- 25% | β (cm/GW) +/- 25% | Glass Transition Temp | Softening Temp | Figure of Merit $n_2/\beta\lambda$ |
|--|-----------------------|--|----------------------------|-----------------------------|-------------------|---------------------------------------|
| $\text{Ge}_{35}\text{As}_{15}\text{Se}_{50}$ | 639nm | 26.4 ⁺ | 0.5 ⁺ | 380C | 474C | 3.2 |
| $\text{Ge}_{33}\text{As}_{12}\text{Se}_{55}$ | 600nm | 15 | 0.4 | 362C | 476C | 2.4 |
| $\text{Ge}_{25}\text{As}_{10}\text{Se}_{65}$ | 585nm | 6 ⁺ | 0.4 ⁺ | 305C | 436C | 1 |
| $\text{Ge}_{22}\text{As}_{20}\text{Se}_{58}$ | 614nm | 9 ⁺ | 0.4 ⁺ | 292 C | | 1.5 |

*based on $\alpha=1000 \text{ cm}^{-1}$; ⁺assuming 19% front surface reflection

References

1. G. Lenz, J. Zimmerman, T. Katsufuji, M. E. Lines, H. Y. Hwang, S. Spalter, R. E. Slusher, S. W. Cheong, J. S. Sanghera, and I. D. Aggarwal, "Large Kerr effect in bulk Se-based chalcogenide glasses," *Opt. Lett.* **25**, 254-257 (2000).
2. J. T. Gopinath, M. Soljačić, E. P. Ippen, V. N. Fuflyigin, W. A. King, and M. Shurgalin, "Third-order nonlinearities in $\text{Ge}_{33}\text{As}_{12}\text{Se}_{55}$ glass for high-index contrast fiber devices". *To be presented at the 2004 Conference on Lasers and Electro-Optics (CLEO)* (June 2004).
3. J. T. Gopinath, M. Soljačić, E. P. Ippen, V. N. Fuflyigin, W. A. King, and M. Shurgalin, "Third order nonlinearities in Ge-As-Se-based glasses for telecommunications applications". *Submitted to Applied Physics Letters* (May 2004).

Nonlinear Nanocrystallite Materials for Laser Mode-locking

Sponsors

National Science Foundation – ECS-01-19452

Air Force Office of Scientific Research – F49620-01-1-0186, F49620-01-01-0084

Project Staff

Rohit P. Prasankumar, Vikas Sharma, Dr. Paul Mak, Professor Michael Ruane, Professor James G. Fujimoto

The shortest pulses from femtosecond solid-state lasers have been generated using Kerr-lens mode-locking, which is a mechanism that utilizes nonlinear self-focusing in the gain medium combined with an intracavity aperture for pulse shaping. However, high-performance Kerr-lens mode-locked lasers are difficult for the casual user to operate because these lasers rely on critical alignment of the laser cavity to achieve the optimal focusing for mode-locking. The optimal alignment for Kerr-lens mode-locking does not coincide with the optimal alignment for laser output power, so short pulses come at the expense of output power. In addition, the shortest-pulse Kerr-lens mode-locked lasers are not self-starting, they require a noise perturbation to be introduced (by tapping a mirror or other cavity element) to start the mode-locking process.

Instead of Kerr-lens mode-locking, femtosecond pulses can be generated using an additional intracavity device, a saturable absorber, for pulse shaping. Lasers using saturable absorbers depend less critically on the cavity alignment and allow self-starting modelocked operation. These saturable absorbers typically consist of semiconductor quantum wells grown on a dielectric mirror structure using molecular beam epitaxy (MBE). These semiconductor saturable absorber mirrors (SESAMs), have been used to generate sub-6-fs pulses with 300 mW average output power from a Ti:sapphire laser [1]. However, these MBE-grown SESAMs have some disadvantages. The fabrication requires complicated and costly equipment, and the materials that can be used to fabricate the SESAMs are limited by lattice-matching requirements.

This project explores the possibility of using RF sputtering to fabricate saturable absorbers that can be used for laser mode-locking, in collaboration with Professor Ruane and Dr. Mak. RF sputtering is relatively simple and inexpensive, and allows flexibility in the materials used for the saturable absorbers. The absorbers used in this study take the form of InAs nanocrystallites doped into SiO₂ films and sputtered onto sapphire substrates. Changing the nanocrystallite size and film thickness allows control of the optical absorption edge and the magnitude of absorption, respectively. The broad nanocrystallite size distribution leads to a broad bandwidth of absorption, which is necessary to support short pulses. Figure 1 shows the measured transmission of three absorbers having different ratios of InAs dopant to SiO₂ film. From the data, we see that the onset of absorption is shifted to longer wavelengths for higher InAs/SiO₂ ratios (larger nanocrystallites), as expected.

Pump-probe spectroscopy was used to measure the saturation fluence of the saturable absorbers. The saturation fluence is an important parameter of a saturable absorber. A low saturation fluence is desirable for avoiding Q-switching instabilities and providing a high modulation depth [2]. Figure 2 shows the saturation fluence versus wavelength for films having different ratios of InAs/SiO₂. From this data, we have developed guidelines for optimizing RF-sputtered saturable absorbers for laser mode-locking [3]. We find that the saturation fluence decreases as the wavelength increases toward the onset of absorption. The data points at 800 nm show that we can control the saturation fluence by varying the nanocrystallite size. Using these guidelines, we have designed semiconductor-doped silica film saturable absorbers to provide self-starting mode-locked operation of a Cr:Forsterite laser [4]. This laser produced pulses having 91 nm bandwidth and 25 fs duration.

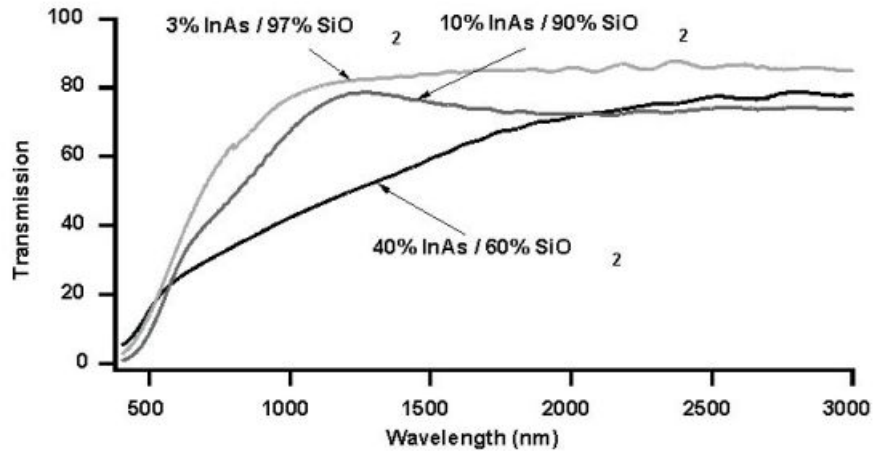


Figure 1. Transmission, measured with a Cary 5E spectrophotometer, for films with different InAs/SiO₂ ratios. The onset of absorption is about 950 nm for the 3% InAs/97% SiO₂, 1200 nm for 10% InAs/90% SiO₂, and 1700 nm for 40% InAs/60% SiO₂.

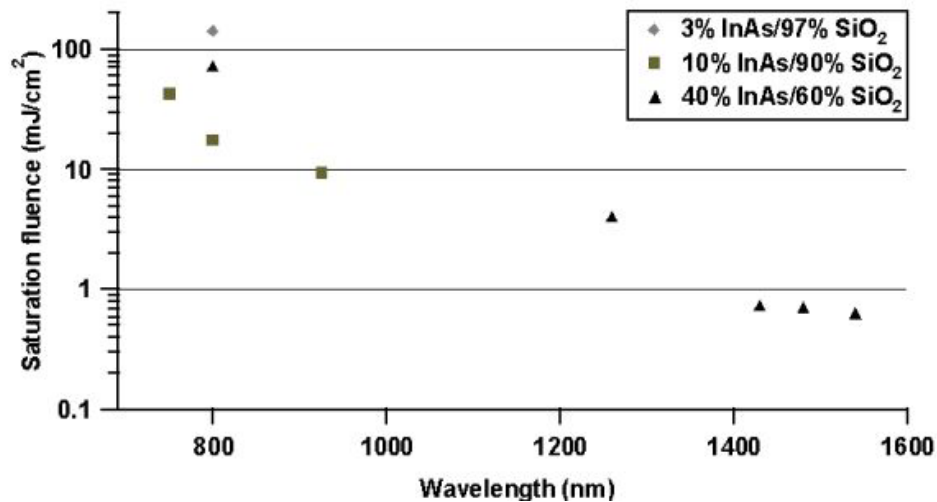


Figure 2. Logarithmic plot of saturation fluence versus wavelength for saturable absorber films having different ratios of InAs/SiO₂.

References

1. D.H. Sutter, G. Steinmeyer, L. Gallmann, N. Matuschek, F. Morier-Genoud, U. Keller, V. Scheuer, G. Angelow, and T. Tschudi, "Semiconductor saturable-absorber mirror-assisted Kerr-lens mode-locked Ti:sapphire laser producing pulses in the two-cycle regime," *Optics Letters* 24(9): 631-3 (1999).
2. R.P. Prasankumar, *Development and Application of Saturable Absorbers to Femtosecond Solid-State Laser Mode-Locking*, Ph.D. Dissertation, Department of Electrical Engineering and Computer Science, MIT, 2003.
3. R.P. Prasankumar, I. Hartl, J.T. Gopinath, E.P. Ippen, J.G. Fujimoto, P. Mak, and M.E. Ruane, "Design and characterization of semiconductor-doped silica film saturable absorbers," *Journal of the Optical Society of America B-Optical Physics* 21(4): 851-857 (2004).
4. R.P. Prasankumar, C. Chudoba, J.G. Fujimoto, P. Mak, and M.F. Ruane, "Self-starting mode locking in a Cr:forsterite laser by use of non-epitaxially-grown semiconductor-doped silica films," *Optics Letters* 27(17): 1564-1566 (2002).

Integrated Tunable, Switchable Optical Add-Drop Multiplexer Design

Sponsor

MIT-Pirelli Program

Air Force Office of Scientific Research - F49620-01-01-0084

Project Staff

Miloš Popović, Michael R. Watts, Tymon Barwicz, Peter T. Rakich, Prof. Erich P. Ippen, Prof. Franz X. Kaertner, Prof. Henry I. Smith

The optical add/drop multiplexer (OADM) is a key enabling component for the implementation of high-capacity all-optical networks that can reach the end-user in the optical domain. Its function is to permit controlled extraction of one or a small number of selected wavelength channels from the wavelength-division-multiplexed (WDM) optical spectrum of a trunk fiber to a secondary fiber link, or into the electrical domain via a photo-detector. Reciprocally, it must also permit insertion of new data streams at a subset of unoccupied wavelengths without disturbing the express traffic.

The complex functionality of OADMs and the large number of such devices called for in a future network make it ideally suited to implementation in micron-scale integrated optics technology.

The present research is an ongoing effort on the functional and electromagnetic design of an integrated OADM chip using high refractive-index contrast (HIC) materials, where dense device integration can be achieved. A cornerstone of the project is the tunable, switchable channel add/drop filter based on microring resonators. Over the course of this year's research, we have demonstrated low-loss, wide-FSR static filters [7], identified a new deleterious resonance-shifting effect and methods for its correction [8], and demonstrated corrected filter designs. We have also continued to develop numerical simulation tools necessary for HIC filter design [9].

1. High-index contrast microring resonator add/drop filters [7-8]

Central to the integrated OADM project are the design and demonstration of microring-resonator-based channel add/drop filters which exhibit low loss, flat passbands and a sharp roll-off, low crosstalk and a wide free spectral range (FSR) that permits operation over a significant part of the C-band. Little *et al.* have demonstrated the potential of microrings as filters [1], and recently high-quality filter responses have been shown in devices of moderate index contrast [2], but their FSR is limited to $\sim 5\text{nm}$. While Vernier operation can be used to suppress non-synchronous filter resonances and extend the FSR [4], it can introduce intolerable dispersion into through-port channels making such filters unsuited to OADMs, in which the through-port response is critical.

Implementation of filters in HIC materials permits negligible radiation loss to be achieved in microring resonators with small bend radii (i.e. a large FSR). With an initial set of device designs fabricated by scanning electron beam lithography (SEBL), we have demonstrated for the first time third-order microring add/drop filters (Fig. 1) with a wide (24nm) FSR and low (3 dB) drop loss [7], a 10 dB improvement over previously-reported results in similar structures [3]. Finite-difference time-domain (FDTD) simulations based on measured dimensions match the measured filter response and indicate that *all* observable loss can be accounted for by the fundamental bending loss and by scattering at couplers into radiation and higher-order ring modes. This indicates not only that loss due to waveguide sidewall roughness (measured at 1.5 dB/cm) has been successfully controlled to have no discernible impact on filter performance, but also that improved waveguide coupler designs could yield new filters with lower loss.

The asymmetry in the drop- and through-port responses in Fig. 1(b) confirms that the three microring resonators are mismatched in resonance frequency, with the middle ring at a higher resonance frequency than the outside two rings (at equal frequencies). Frequency mismatch can have a particularly deleterious effect on through-port extinction (limited to 7.5dB in Fig. 1), where

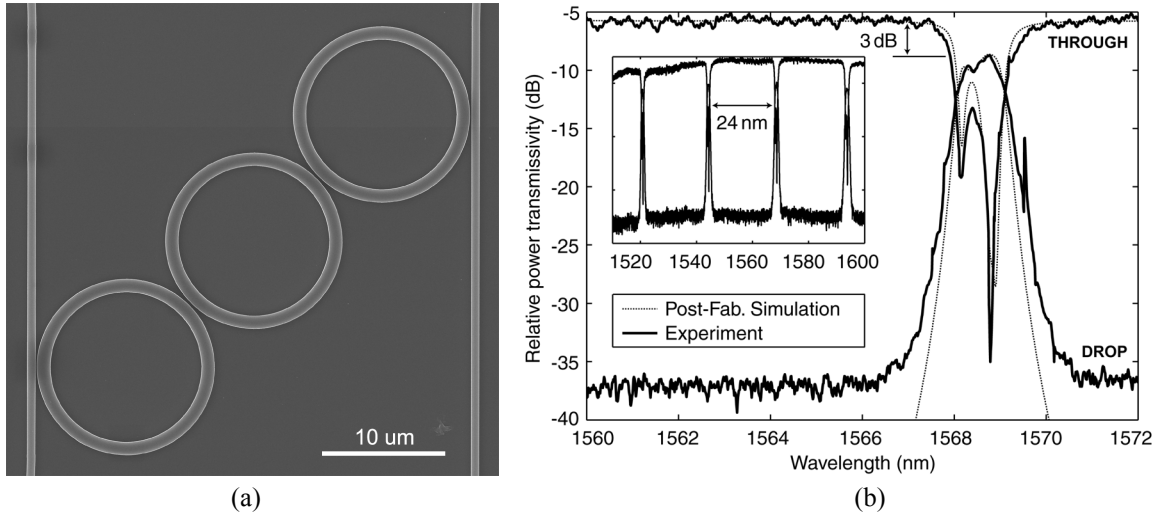


Figure 1. (a) SEM of 3rd-order microring filter, measuring 50mm across, fabricated in high-index contrast SiN; (b) drop-port and through-port responses show low loss (3 dB) in a wide-FSR filter (24nm) [7].

30dB is required for add/drop filter functionality. While proximity effects and discretization error in SEBL fabrication can account for such a symmetric frequency mismatch, we have shown that there is also a fundamental source of resonance frequency shift which can have a significant impact on filter performance [8].

The resonance frequency of each microring in a coupled configuration, as in Fig. 1(a), is modified by the presence of adjacent coupling structures (bus waveguides and other rings). Because the several rings in a filter have different surroundings (e.g. their spacing is non-uniform), their frequencies shift by different amounts from the uncoupled resonance frequency. The result is a frequency mismatch between the rings and a deteriorated frequency response. That the effective index of each resonance increases, and thus the resonance frequency decreases is an intuitive result. However, when the adjacent coupling structures possess well-matched modes of their own, we have shown that the coupling-induced frequency shift (CIFS) can be of the opposite sign also [8]. Fig. 2 illustrates the resonance shift vs. ring-bus spacing with a two-dimensional example of a microring symmetrically coupled to two bus waveguides. With a bus width of

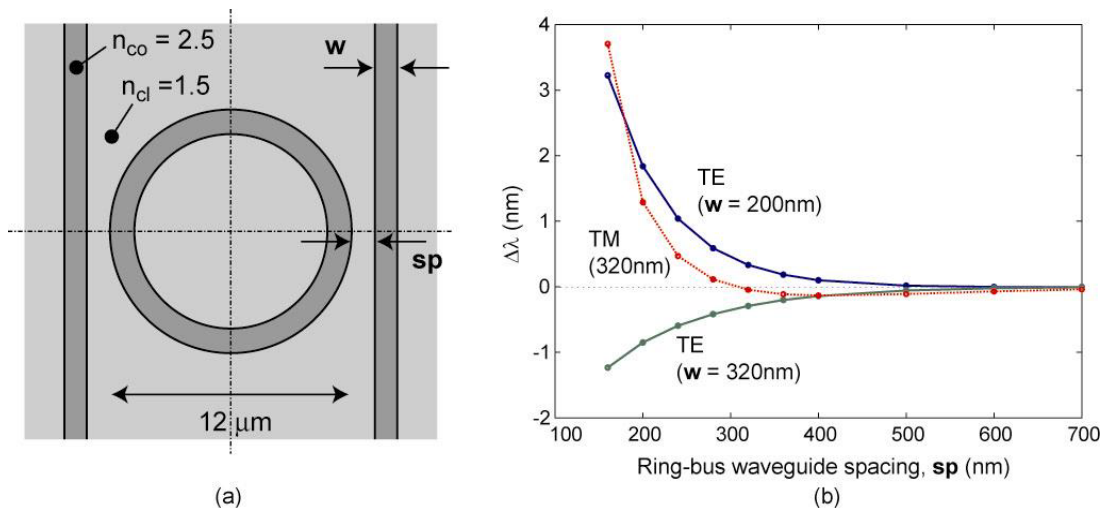


Figure 2. (a) schematic of 2D ring resonator model loaded by two bus waveguides used to illustrate the coupling-induced frequency shift effect encountered in the devices of Fig. 1; (b) wavelength shift (CIFS) vs. ring-bus waveguide spacing for two examples illustrates that a CIFS of either sign can be observed [8].

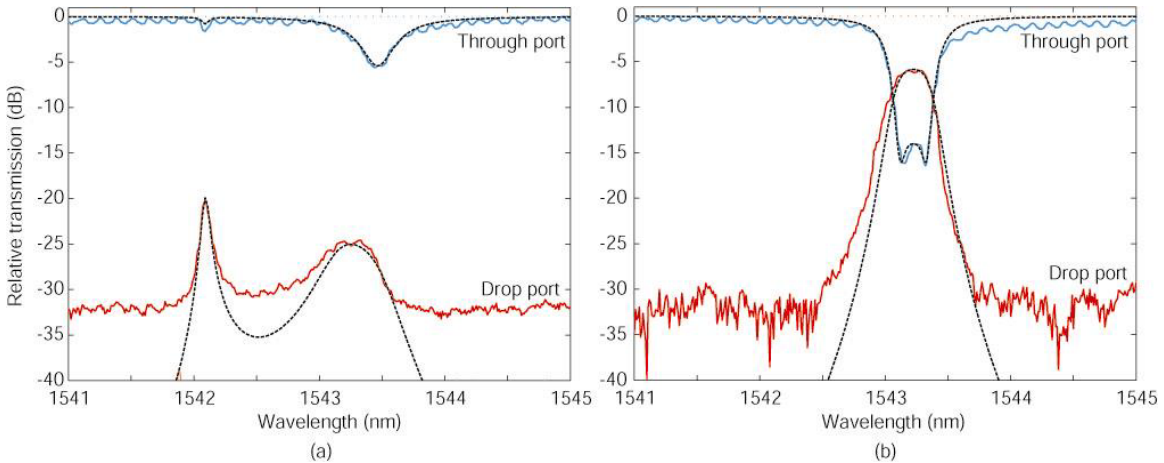


Figure 3. Second-generation filter: (a) Drop- and through-port measured responses of a regular (CIFS-uncompensated) 3-ring filter (model fit in black dash); (b) responses of a preliminary CIFS-compensated design show improved through port extinction (model fits in black dashed line).

320nm, it is shown that the two polarizations of the same structure can have opposite signs of CIFS. On the other hand, a change in the waveguide width can change the sign of CIFS in the same (TE in this case) resonance. The solution to correcting the frequency mismatch due to CIFS is to predistort the resonance frequencies of the filter rings in design, by changing their shape, structure or material index such that in the final coupled configuration the effective resonance frequency degeneracy is restored. Because multi-pole optical filters require the coupling of resonators of identical frequencies, it has been common practice to design filters with coupled microrings of identical dimensions. We have shown for the first time that the ideal design of multiple-ring filters must employ ring resonators of slightly *non-identical* dimensions or structure, by design [8].

A simple way to realize a predistortion to compensate for the CIFS is to enlarge the middle ring by an increase in electron-beam dose during its exposure, in order to reduce its resonance frequency. This method permits fine control of the correction. Fig. 3 shows a second-generation filter design with several improvements including CIFS correction. FDTD simulations have been employed to simulate ring-bus and ring-ring coupling coefficients in order to arrive at a design bandwidth of 40 GHz, and to improve coupler design for reduced losses. In addition, the e-beam dose on the middle ring was varied to produce a CIFS-corrected filter.

Fig. 3(a) shows the response of an uncompensated filter. The combination of CIFS and proximity-effect frequency shifts produces a severely degraded filter response. The wide peak on the right can be identified with the strongly-coupled outside-ring resonances, while the narrow peak on the left can be identified with the weakly-coupled middle ring, indicating a frequency difference of about 150 GHz. Fig. 3(b) shows the 40 GHz filter where the middle ring has been frequency-compensated. The passband is flat, and the through port shows an improved extinction of 13dB. Future work remains to identify the sources of the larger than expected insertion loss and correct it.

3. Numerical simulation tools [9]

High-index contrast devices have modal fields with hybrid polarization distributions and strong normal-field discontinuities, and their interaction without careful design can lead to significant scattering of radiation. All of these factors contribute to the need for rigorous numerical simulations to aid in design of HIC integrated optical components.

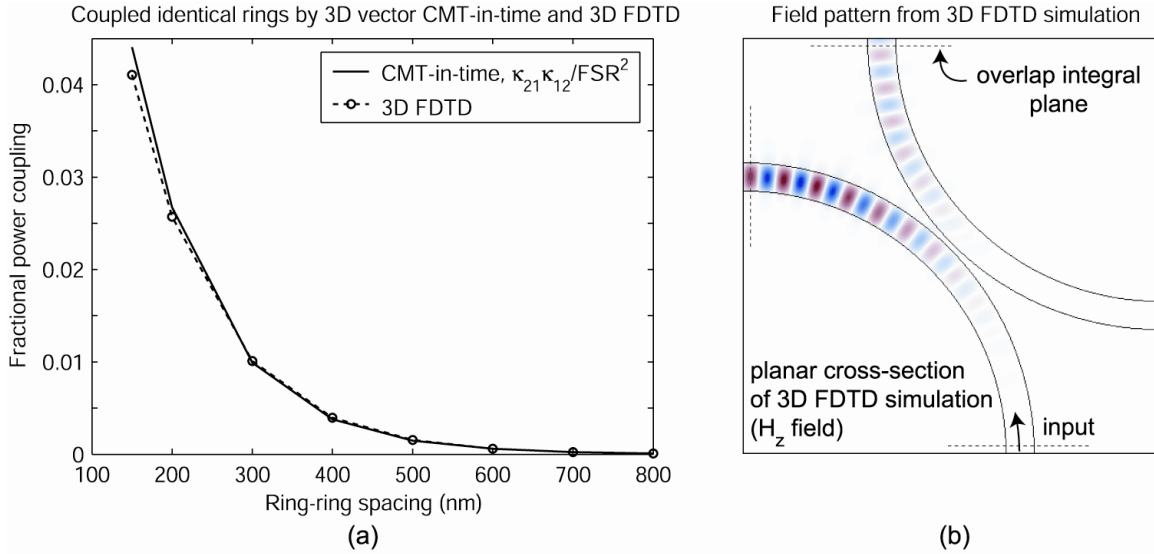


Figure 4. (a) Comparison of full-vector coupled-mode theory in time and 3D FDTD prediction of ring-ring coupling; (b) normal magnetic field distribution from a 3D FDTD simulation used to compute ring-to-ring coupling for the microring filter design in Fig. 3 (figure from [10]).

We have developed a complex-frequency, vector-field mode solver for leaky resonator modes [9] using the broadband perfectly-matched layer (PML) absorbing boundary condition [5,6]. The mode solver has been applied to accurately model 3D microring leaky resonances and design high radiation-Q microrings for the filters in Figs. 1 and 3, as well as to investigate 2D arbitrary-geometry coupled-resonator configurations, such as that for the coupling-induced frequency shift (CIFS) in the example of Fig. 2.

Computed microring leaky modes have also been used as the basis in a vectorial coupled-mode theory in time (CMT) formulation to evaluate ring-ring coupling, shown in Fig. 4(a) compared to numerically rigorous FDTD results with good agreement. However, CMT is incapable of predicting scattering to radiation at waveguide couplers which must be taken into account in the design of resonator filters. Thus, 3D FDTD simulations are relied upon for the design of ring-ring and ring-bus waveguide couplers.

In FDTD, the full-wave Maxwell's equations are propagated by discretization in space and time. With no approximations except the discretization, FDTD leads to very accurate results for arbitrary structures over wide frequency spectra. Because of the large memory and computational requirements of 3D FDTD simulations, a parallelized code has been implemented on a shared memory, multi-processor machine. The magnetic field snapshot from one FDTD simulation used to compute ring-ring coupling for our second-generation filter design in Fig. 3 is shown in Fig. 4(b).

Some of the advances in theory and device design from this year's work have been incorporated into a contributed book chapter on microring-resonator filters, co-authored with colleagues from Little Optics, Inc. [10]. In forthcoming work, improved filter designs will be combined with a polarization diversity scheme to demonstrate a polarization-independent add/drop filter, and focus will be turned to incorporating tuning and switching capabilities into the filter design.

References

1. B.E. Little, S.T. Chu, H.A. Haus, J. Foresi and J.-P. Laine, "Microring resonator channel-dropping filters," *J. Lightwave Technol.*, vol. 15, pp. 998-1005, June 1997.

2. B.E. Little, "Advances in microring resonators," in *Proc. Integrated Photonics Research Conference*, 2003, pp. 165-167.
3. J.V. Hryniewicz, P.P. Absil, B.E. Little, R.A. Wilson and P.-T. Ho, "Higher order filter response in coupled microring resonators," *IEEE Photon. Technol. Lett.* 12, pp. 320-322, 2000.
4. Y. Yanagase, S. Suzuki, Y. Kokubun and S.T. Chu, "Box-like filter response and expansion of FSR by a vertically triple coupled microring resonator filter," *J. Lightwave Technol.* 20, pp. 1525-1529, 2002.
5. J.-P. Berenger, "A perfectly matched layer for the absorption of electromagnetic waves," *J. Comp. Phys.*, 114(2):185-200, Oct 1994.
6. F.L. Teixeira and W.C. Chew, "PML-FDTD in cylindrical and spherical grids," *IEEE Microwave and Guided Wave Lett.*, vol. 7, pp. 285-287, Sep 1997.

Publications

T. Barwicz, M.A. Popović, P.T. Rakich, M.R. Watts, in *Proc. Optical Fiber Conference*, 2004, TuL3.

C. Manolatou, M.A. Popović, P.T. Rakich, T. Barwicz, H.A. Haus, and E.P. Ippen, "Spectral anomalies due to coupling-induced frequency shifts in dielectric coupled-resonator filters," in *Proc. Optical Fiber Conference*, 2004, TuD4.

M. Popović, "Complex-frequency leaky mode computations using PML boundary layers for dielectric resonant structures," in *Proc. Integrated Photonics Research*, 2003.

H.A. Haus, M. Popović, M.R. Watts and C. Manolatou; B.E. Little and S.T. Chu, "Optical resonators and filters" contributed chapter in *Optical Microcavities*, Kerry Vahala, ed., to be published.

All Optical Switching and Modulation in Silicon by Carrier Injection

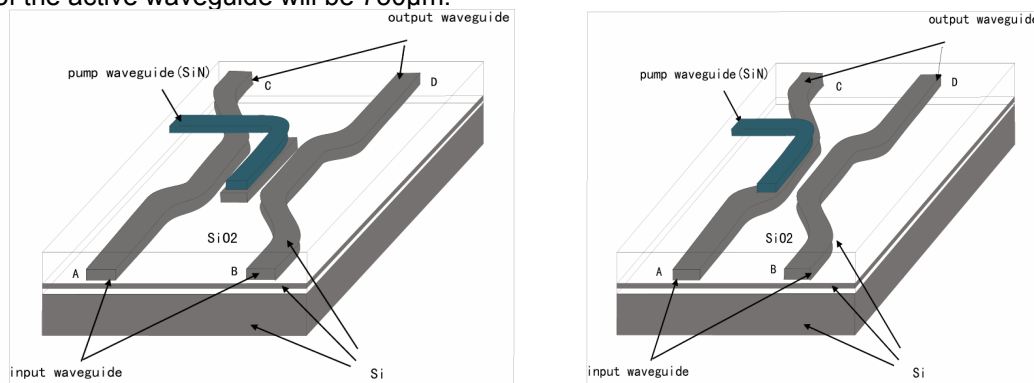
Sponsors:

MIT-Communications Roadmap Consortium
National Science Foundation - ECS 03-22740

Project Staff:

Fuwan Gan, Felix Grawert, Shoji Akiyama, Dr. Jurgen Michel, Dr. Kazumi Wada, Prof. Franz X. Kaertner

We investigated different layouts for switches based on carrier injection in high index contrast Si/SiO₂/SiN waveguides as shown in Fig. 1. The use of crystalline silicon as well as poly-silicon waveguides is possible. The later can be used for switches with fast switching time. The switches consist of two/three silicon waveguides that channel the signal through a coupler region and a SiN-control waveguide. Without any light (800 nm, for example) in the control waveguide, the input waveguide couples either through a center waveguide (Fig. 1.a) or directly to the output waveguide (Fig. 1 b). The coupling length is suitably chosen such that all signal light in the input waveguide couples to the output waveguide when no carriers are injected ("OFF-State": No light leaves the input waveguide). In this state the system is ideally lossless and 100% power is transferred to the output waveguide. To have full transmission in the OFF-state the typical length of the active waveguide will be 750 μ m.



a.) Slow Switch

Figure 1: Layouts for low loss switches using optical carrier injection. Slow switching needs the center waveguide to prevent carriers from escaping.

The architecture of Fig. 1, i.e. parallel signal and control waveguides, is motivated by the problem of absorbing nearly all of the 800 nm photons (the control light) in a 550 nm-thick waveguide (the penetration depth of 800 nm light is about 16 μ m). Fig. 1 shows an efficient waveguide coupling of the control light into a Si-layer such that essentially all control light is absorbed in the thin but long Si-waveguide [3]. Numerical simulations show that, for distances between the control and signal waveguide on the order of 10-50 nm and for a waveguide length of 100 μ m and beyond, more than 90% of the control light is absorbed in the signal waveguide for efficient carrier generation. The index change by carrier injection comes at the price of induced free carrier absorption. In the "ON-State", control light entering the SiN-waveguide is absorbed in the active waveguide and changes the index, which detunes the active waveguide from the input waveguide. No light is transferred to the output waveguide and almost all light continues in the input waveguide.

A full numerical simulation of a specific switch gives transmission results for the ON and OFF state shown in Fig. 2. Note that the transmission loss of the switch is less than 3% in the OFF-state and less than 10% in the ON-State over the whole C-band. The ON-OFF ratio of output

waveguide can be as large as 40 dB over the whole C-band. Assuming a carrier lifetime of 100 ns in the waveguide results in a switching power of only about 1mW.

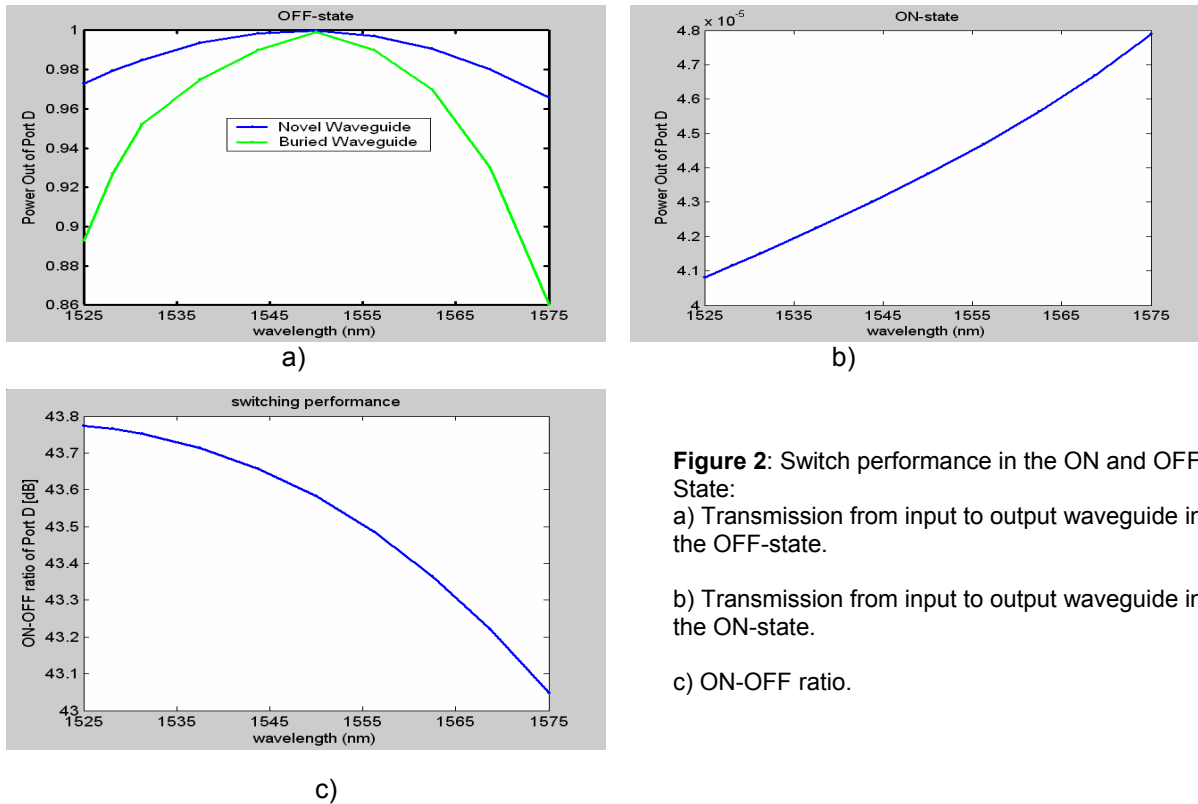


Figure 2: Switch performance in the ON and OFF State:

a) Transmission from input to output waveguide in the OFF-state.

b) Transmission from input to output waveguide in the ON-state.

c) ON-OFF ratio.

The performance described above can be only achieved by using a waveguide, which shows high thermal conductivity to the substrate, such that large optical powers can be dissipated in the waveguide with negligible temperature increase. To achieve good thermal properties, broadband behavior of the switch, reduced sensitivity with respect to fabrication tolerances and carrier confinement we developed a novel Split-Rib waveguide as shown in Fig. 3.c. Such a waveguide combines the favorable properties of an ordinary buried waveguide with those of a rib-waveguide.

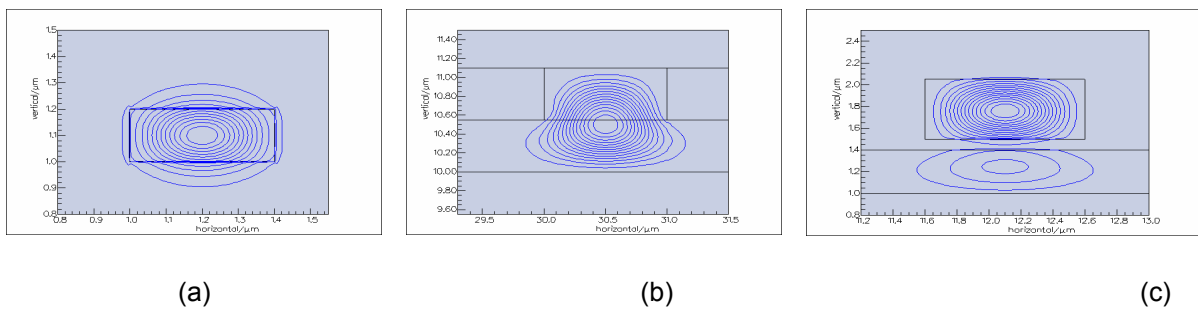


Figure 3: Single Mode Profile, (a) stripe waveguide, (b) ridge waveguide, (c) novel waveguide.

1. Soref, R. A. Silicon-based optoelectronics. Proc. IEEE 81, 1687–1706 (1993).
2. A. Soref and J. P. Lorenzo, “Optically controlled integrated optical switch,” US Patent 4,693,547 (1987).
3. M. Fisher and K. Wada, “Method for Efficient Carrier Generation in Silicon Waveguide Systems For Switching/Modulation Purposes Using Parallel Pump and Signal Waveguides,” MIT-Patent Case 9941.

Polarization Effects in Lightwave Systems

Sponsors

DSO National Laboratories;
Air Force Office of Scientific Research - F49620-01-01-0084

Project Staff

P.B. Phua, Professor H. A. Haus, Professor E. P. Ippen,

The deployment of optical amplifiers in lightwave systems has significantly increased the length of propagation and the number of optical components distributed along the link. As a result, small polarization effects, such as polarization dependent loss (PDL) and polarization mode dispersion (PMD) accumulate to produce noticeable performance degradation and limit the long distance ultrahigh speed optical telecommunication systems.

As the bit rate of a single channel increases, compensator that cancels the first order of these polarization effects is insufficient since higher order effects dominate the signal's degradation. Thus we propose in [1,2] a broadband feed-forward compensator for both PDL and PMD. By the polar decomposition theorem, the compensation can be carried out by having a lumped PDL followed by PMD compensation at the receiver's end. Figure 1 shows its schematic. We employ polarization scrambling at the transmitter's end for characterizing the feed-forward information. A portion of the optical signal is tapped at the fiber output for real-time spectrally resolved polarimetric SOP monitoring. From the polarimetric measurements, we know the maximum and minimum attenuation and its associated polarization states. Thus we can characterize the PDL of each frequency component. Based on this information, we compensate the global PDL using a broadband PDL compensation module shown in Figure 2. This PDL compensator consists of three stages. Stage 1 and 2 are the frequency-dependent polarization rotators that align all the different PDL vectors into the $\{1,0,0\}$ direction in Stokes space. Stage 3 eliminates both the PDL magnitude and the frequency dependence in the isotropic attenuation by introducing different frequency-dependent variable attenuation to each polarization. Using the Stokes space representation, we synthesize the required rotation angle profiles of the frequency-dependent polarization rotators, Stage 1 and Stage 2, and the required transmission profiles of the frequency-dependent variable attenuators in Stage 3, once the information on the PDL is gathered.

By applying the known transformation of each stage to the monitored polarimetric data, we then use the transformed SOP to deduce the composite PMD as a function of frequency by the method given in [3]. The composite PMD spectrum serves as the input parameter for subsequent broadband PMD compensation. The broadband PMD compensator is comprised of 4 stages. The net effect of the first two stages is equivalent to a frequency dependent polarization rotation that aligns all PMD vectors into $\{1,0,0\}$. The third stage compensates the frequency dependent variable Differential Group Delay (DGD) and the last stage compensates for the isotropic dispersion created by the first three stages as shown in Figure 3. Using PMD concatenation rule, we synthesize the required rotation profile of the various stages.

There are at least three physical implementations of the proposed PDL and PMD compensators. The first two implementations can be adapted from the femtosecond pulse shaping schemes using a spatial light modulator and using a deformable mirror. With diffraction gratings, one can disperse the various frequency components spatially onto the spatial phase modulator (or deformable mirror) and program appropriate spectral phase to achieve the required phase difference profiles. The third promising implementation is based on All-Pass Filters (APFs) integrated on a planar lightwave circuit as shown in Figure 4 for the PDL compensator and Figure 5 for the PMD compensator. By numerical simulations, we show significant improvement after compensation using such APFs architecture [1,2]. It is also worthwhile to mention that the inverse

of the above proposed configurations can be used for deterministically controlled PDL+PMD emulation [4].

References

1. P.B. Phua and E. P. Ippen, "A Deterministic Broadband Polarization-Dependent-Loss Compensator", submitted for publication.
2. P.B. Phua, Hermann. A. Haus and E. P. Ippen, "All-Frequency PMD Compensator In Feed-Forward Scheme", To appear in Journal of Lightwave Technology, Vol. 22, No.5, May 2004.
3. P.B. Phua, John M. Fini and Hermann A. Haus, "Real-Time First and Second Order PMD characterization using Averaged State-of-Polarization of Filtered Signal and Polarization Scrambling", Journal of Lightwave Technology, Vol.21, No.4, April 2003, pg 982-989.
4. P.B. Phua, H.A. Haus, E.P. Ippen, "Deterministic Broadband PMD Emulator", To appear in IEEE Photonics Technology Letters.

Broadband Spectral Measurements of High-Index Photonic Circuits Using Supercontinuum Light Source from 1 to 2 μm

Sponsors

U.S Air Force – Office of Scientific Research
Grant F49620-01-1-0084
National Science Foundation ECS-0119452
MRSEC

Project Staff

Peter T. Rakich, Dr. Chee Wei Wong, Dr. Steven G. Johnson, Juliet Gopinath, Dr. Hideyuki Sotobayashi, Professor John D. Joannopoulos, Professor Erich Ippen

High index photonic crystal waveguides promise many scientific and practical applications for novel photonic devices. However, spectral measurements of such devices continue to be a daunting task. Conventional measurement techniques generally employ tunable lasers to measure the broad spectral features produced by photonic crystals, most notably photonic bandgaps, which can span hundreds of nanometers. However, few practical tunable sources exist which span the 1-2 μm spectral range, which is critical for measurement of broadband photonic devices at telecommunications wavelengths.

In the past several years, numerous fiber-based supercontinuum sources have been developed, producing high brightness white light spanning wavelengths from 0.6-2.20 μm [1, 2, 9]. In this paper, we demonstrate that a fiber-based supercontinuum source can be a practical and effective source for the measurement of nano-scale photonic bandgap waveguides over a broad spectral range spanning from 1.15 to 2.00 μm . Previous work has used supercontinuum centered at shorter wavelengths to measure two-dimensional photonic crystal slab waveguides [3-5]. In contrast, we use supercontinuum centered at telecommunications wavelengths in an all-fiber waveguide system with a measurement apparatus which is optimized for longer wavelengths.

One dimensional photonic crystal microcavities have been studied extensively over the past several years [6-8]. Previously, due to the wavelength limitations of conventional tunable lasers, these devices have been rescaled and measured to construct a reasonable picture of the band structure based on the known scaling properties of photonic crystals. To simplify these measurements, an all fiber-based waveguide measurement apparatus was constructed with a white-light supercontinuum source. This enabled transmission measurements of microcavities from 1.15-2.00 μm . These transmission measurements are compared with rigorous 3D FDTD simulations based on device parameters extracted from SEM measurements.

Supercontinuum white-light was produced by coupling 150 fs pulses generated by an optical parametric oscillator (OPO) into a 500 m length of highly nonlinear dispersion shifted fiber (HNL-DSF). The HNL-DSF has a zero dispersion wavelength of 1.565 μm and nonlinear coefficients of 21 $\text{km}^{-1}\text{W}^{-1}$. An input power to the HNL-DSF of 30 mW resulted in the supercontinuum spectrum, shown in Figure 1. Due to the nonlinear nature of the supercontinuum light source, small changes in laser or fiber state can cause significant and rapid fluctuations in the output spectrum [10]. In addition, spectral variations of 20dB were typical. For this reason, it was necessary to measure a small fraction of reference power (reference) directly from the SC light source with a broadband fiber optic coupler, at all times, in order to normalize the waveguide transmission measurements. This was done by imaging the signal from the waveguide (signal) and the reference, through a monochromator onto two identical photodetectors at the exit plane of the monochromator. To remove all wavelength dependence produced by the apparatus and fiber-to-waveguide coupling, all microcavity measurements were normalized to that of a straight waveguide without a photonic crystal, which was fabricated on the same chip. The experimental arrangement is shown in Figure 2.

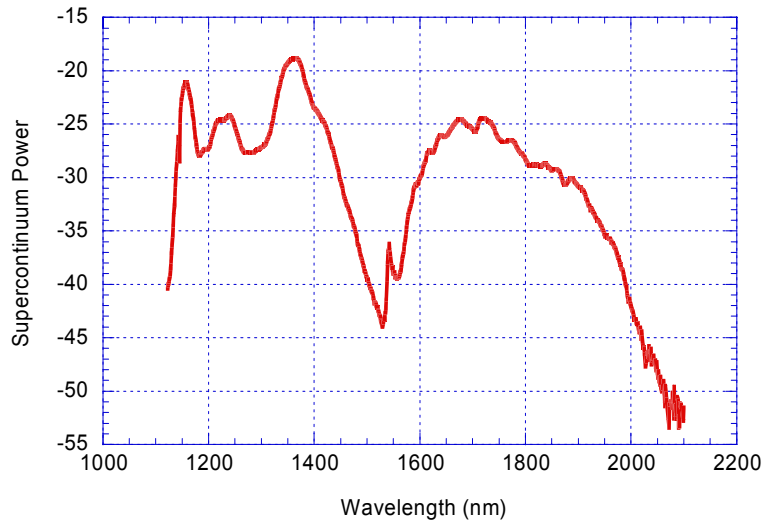


Figure 1. Optical power spectrum of supercontinuum generated with 500 meters of dispersion shifted fiber. Spectrum acquired while coupling 30mW of average power from an OPO tuned to a center wavelength of 1575 nm at a repetition rate of 82 MHz.

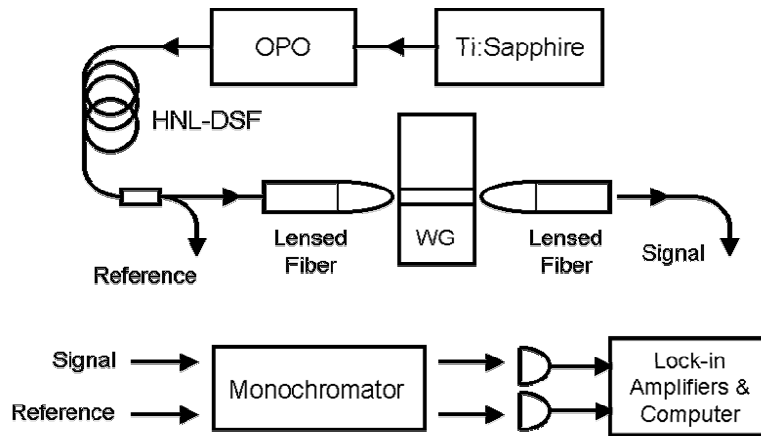


Figure 2. A schematic of the supercontinuum based waveguide measurement apparatus. Pulses from OPO are coupled into HNL-DSF to generate supercontinuum light. Supercontinuum is coupled into and out of the waveguide with lensed fibers. Signals are detected and acquired after passing through a monochromator.

The result of a microcavity measurement is shown in Figure 3. A 25dB reduction in transmission from 1750-1550nm is clear evidence of a photonic bandgap. In addition, a microcavity resonance having a total Q of 230 is observed at 1615nm. Superposed with the experimental data is a theoretical transmission spectrum of TE light which was generated through 3D-FDTD simulations. In comparing the theoretical spectrum with experiment we see very good agreement of the longer wavelength bandedge and the microcavity resonance wavelength. However, the higher than predicted transmission at the shorter wavelengths is observed. This has been identified as coupling to a TM mode, which has high transmission in the 1300-1500nm range. Until a method for polarization control is developed, isolation of the TE and TM transmission information will not be possible.

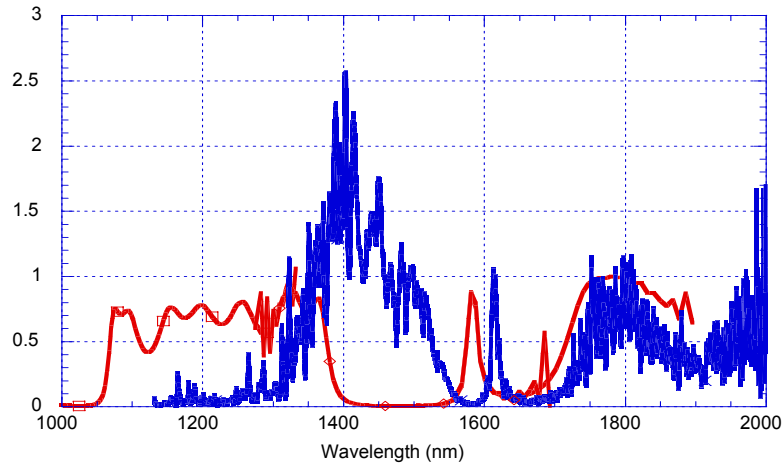


Figure 3. Transmission spectrum of microcavity normalized to that of straight waveguide with a spectral resolution of 0.8 nm. The microcavity resonance can be seen at 1615nm having a resonant Q of 230.

To demonstrate the validity of this measurement technique, measurements of the same microcavity were taken with both a tunable laser source and with the supercontinuum. The results are shown in Figure 4.

The two techniques yield nearly equivalent transmission spectra. Fabry-Perot oscillations are observed in both measurements, resulting from reflections at the photonic-crystal boundaries and at the end facets of the waveguide. The only notable difference between the two is that the laser measurements have a more pronounced Fabry-Perot oscillation and a slightly narrower measured resonance width, which are both accounted for by the lower resolution of a monochromator-based measurement. The resolution limitations of the supercontinuum-based measurements arise from spectral-power limitations of the light source, which limit the degree to which we can reduce the slits while still maintaining good signal to noise. In contrast, the laser-based measurements are only limited by the linewidth of the tunable laser.

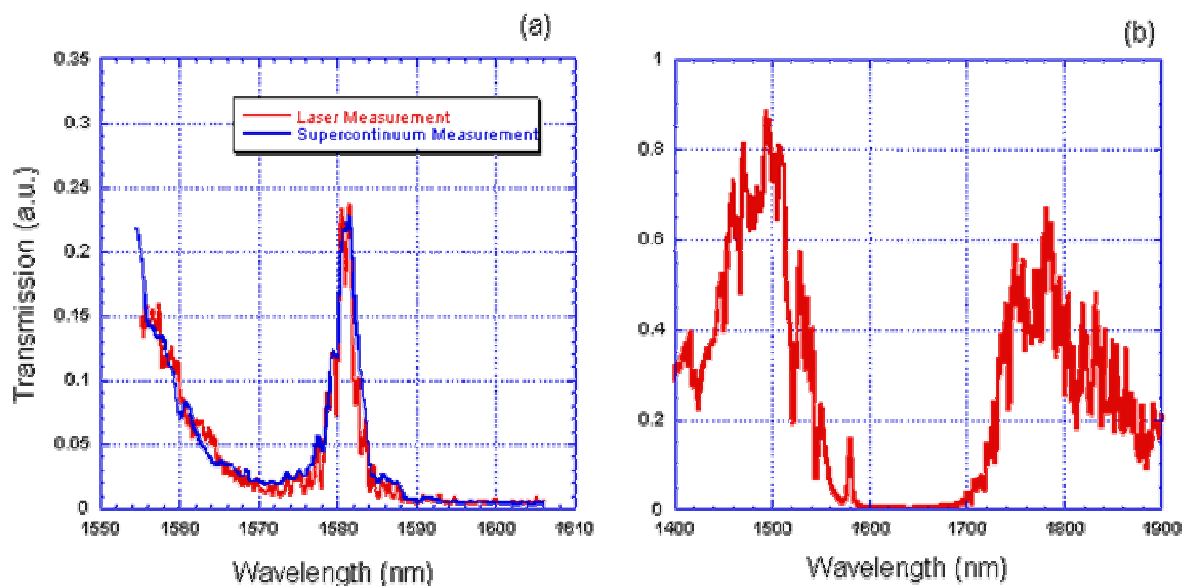


Figure 4. (a) A comparison of laser transmission measurement and supercontinuum measurements is made on a device with microcavity resonance overlapping tunable laser spectral range. Laser measurements were performed with a resolution of 0.01nm while that of the supercontinuum measurement is 0.4nm. (b) Large wavelength scan of same microcavity structure using SC light source.

In conclusion, a supercontinuum-based measurement technique has been demonstrated using only fiber components, enabling rapid measurements of photonic crystal microcavities from 1.15-2.00 μm . A comparison between conventional laser measurements and supercontinuum measurements was made on a microcavity, showing very good agreement between the two techniques. These measurements demonstrate that this technique can produce measurements of resolution and quality comparable to that of laser based techniques. Although the source used for this study was an OPO-pumped Ti:Sapphire, it could easily be replaced with a fiber laser, making the source cheap, compact and more practical to use. We currently work toward the development of broadband fiber-based polarization control techniques and new supercontinuum sources which are optimized for measurements of this type.

References

1. J.W. Nicholson, M.F. Yan, P. Wisk, J. Fleming, F. DiMarcello, E. Monberg, A. Yablon, C. Jorgensen, Veng, T., "All-fiber, octave-spanning supercontinuum" *Optics Letters*, v 28, n 8, 15 April 2003, p 643-5.
2. D.J. Ripin, Kuo-Yi Lim, G.S. Petrich, P.R. Villeneuve, Shanhui Fan, E.R. Thoen, J.D. Joannopoulos, E.P. Ippen, L.A. Kolodziejski, "One-dimensional photonic bandgap microcavities for strong optical confinement in GaAs and GaAs/Al/sub x/O/sub y/ semiconductor waveguides" *Journal of Lightwave Technology*, v 17, n 11, Nov. 1999, p 2152-60.
3. M.C. Netti, C.E. Finlayson, J.J. Baumberg, M.D.B. Charlton, M.E. Zoorob, J.S. Wilkinson, G.J. Parker, "Separation of photonic crystal waveguides modes using femtosecond time-of-flight" *Applied Physics Letters*, v 81, n 21, 18 Nov. 2002, p 3927-9

Demonstration of Line-Defect Guidance and Adiabatic Mode Conversion in 2-Dimensional Photonic Crystal Formed from Posts at Optical Wavelengths

Sponsors

U.S Air Force – Office of Scientific Research
Grant F49620-01-1-0084
National Science Foundation ECS-0119452
MRSEC

Project Staff

Peter T. Rakich, Solomon Assefa, Dr. P. Bienstman, Dr. Steven G. Johnson, Dr. Gale S. Petrich, Prof. John D. Joannopoulos, Prof. Leslie A. Kolodziejski, Prof. Henry I Smith and Prof. Erich Ippen

Photonic crystals have generated a great deal of interest as a scientific pursuit and for numerous applications. During the past several years, many studies have examined the guidance of light in photonic crystals formed by a periodic array of holes in high index slab waveguides [1-2]; however, little work has been done on photonic crystals formed by a periodic array of posts. In this report we demonstrate guidance through a line defect in a 2-dimensional photonic crystal formed from posts of high index dielectric. The defect waveguide is created by reducing the size of the posts from that of the surrounding photonic crystal, and light is confined in the defect state through Bragg reflection as opposed to total internal reflection. We present transmission measurements and radiation images of the photonic crystal waveguides which are both very strong evidence for efficient coupling to, and guidance of the photonic crystal defect mode.

Due to the fact that the photonic crystal defect mode is, in general, very poorly matched to a conventional waveguide mode, the insertion losses into the defect waveguide can be very high. For this reason we have developed a novel method for adiabatically introducing the defect waveguide to the bulk photonic crystal. The adiabatic design is, in principle, very simple. First, in a short region of about 2 microns, the straight waveguide is gradually transformed into a periodic array of posts which resembles the desired line defect design. Second, the surrounding photonic crystal is gradually introduced to the defect waveguide to adiabatically generate the designed defect mode. A fabricated structure of this type can be seen in Figure 1 (a). The devices were fabricated through e-beam lithography in a GaAs/AlGaAs materials system. The top portion of the posts is formed from high index GaAs, while the lower portion of the post and cladding are formed from a low index Al_xO_y . The high index contrast between the two materials results in a high degree of confinement in the vertical direction. Fabrication specifics can be found in ref [4].

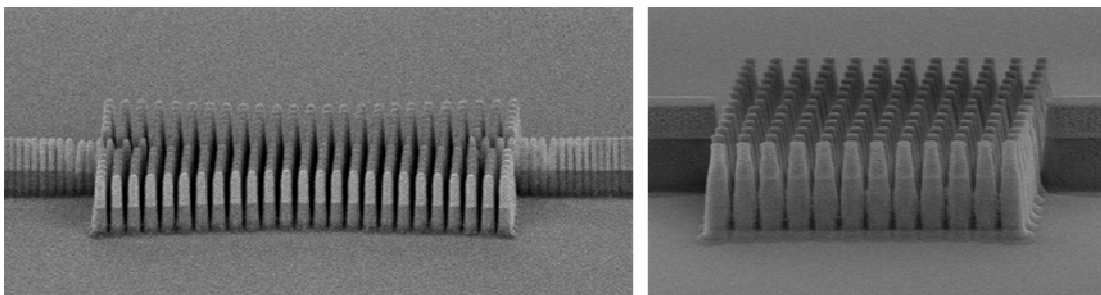


Figure 1. (a) SEM of an adiabatic taper which couples to a line defect. The straight waveguide is gradually transformed into a line of posts. The posts forming the photonic crystal are gradually brought closer to the line of posts until the designed defect photonic crystal state is achieved. (b) SEM of a bulk photonic crystal waveguide to which two straight waveguides are coupled.

In order to correctly identify the wavelengths over which the line-defect actually guides light, a device having a section of bulk photonic crystal, as shown in Figure 1 (b), was fabricated. Transmission measurements through the bulk photonic crystal device allow us to pinpoint the wavelengths over which the photonic crystal has a bandgap. Over these same wavelengths the line-defect state should be highly transmitting.

Measurements of these devices were performed with the use of tunable lasers, a polarization controller and a fiber-lens assembly which was used to couple light into the waveguides. The waveguide output mode was imaged onto IR cameras and detectors using nondispersive optics. The photocurrent signal resulting from the imaged mode was processed with a lock-in amplifier and acquired point by point as the tunable laser was scanned. During all measurements great care was taken to ensure that the correct polarization state was launched into and measured from the waveguides. Some such measurements can be seen in figures 2 (a) and (b). Figure 2 (a) shows TM transmission measurements through two bulk photonic crystal devices having four periods of posts. A pronounced dip in transmission can be seen from 1450-1480 nm which is a strong indication of a photonic bandgap. These measurements are in good agreement with 3-D finite difference time domain simulations which predict a photonic bandgap at these wavelengths. In addition, TM transmission through a line-defect and adiabatic taper is shown in figure 2 (b). Notice that the transmission reaches its maximum at wavelengths that correspond to the middle of the photonic bandgap. This is a very strong indication that light is being efficiently coupled to the photonic crystal line-defect through the photonic crystal taper.

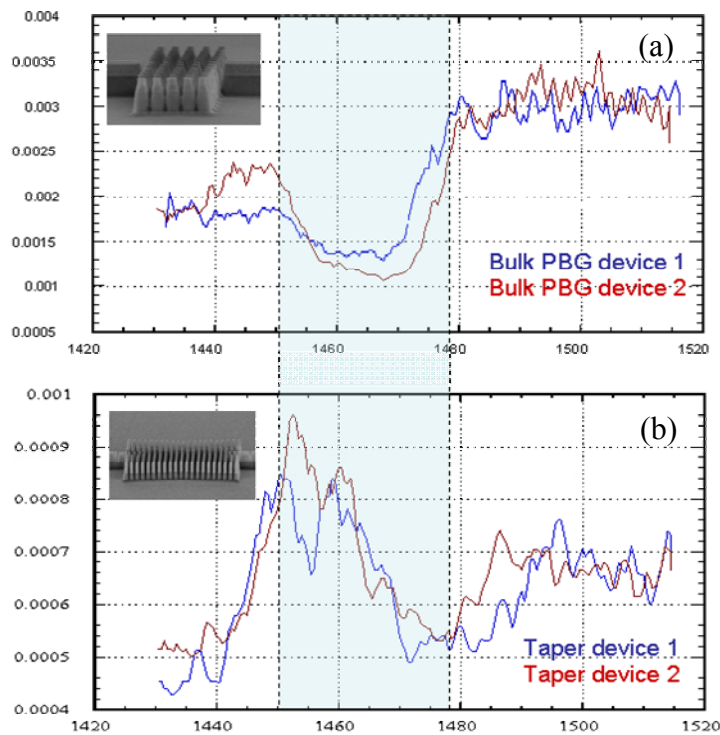


Figure 2. (a) Transmission spectrum through a bulk 2-dimensional photonic crystal with 4 periods. A pronounced dip in transmission from 1450-1480 nm is evidence of photonic bandgap. (b) transmission spectrum through an adiabatically formed line defect passing through 4 photonic crystal periods. Marked increase in transmission observed to coincide with the shorter wavelength bandedge. Both sets of measurements are in good agreement with simulations.

Further evidence of defect guidance is shown in Figure 3. Figure 3 (a) is a low resolution optical image of an adiabatic taper device taken at visible wavelengths. This image allows us to identify the position of the waveguide and photonic crystal in the IR image taken under similar conditions seen in figure 3 (b). The IR image shown was taken with a vidicon camera at a laser excitation wavelength of 1453 nms. One first notices a bright spot to the left of the photonic crystal, and with close observation, a dim stripe which continues to the other side of the photonic crystal. The bright spot, indicating strong coupling to radiation at a point on the waveguide, can be understood if we examine the SEM of the adiabatic taper shown in figure 1 (a). A single point can be seen on the waveguides to either side of the photonic crystal where the periodicity of the waveguide is broken. This break in periodicity tends to cause strong coupling to radiation. Despite this fabrication defect, we are able to observe a dim stripe from left to right across the line defect and through the adiabatic taper, which is clear evidence of a guided defect mode.

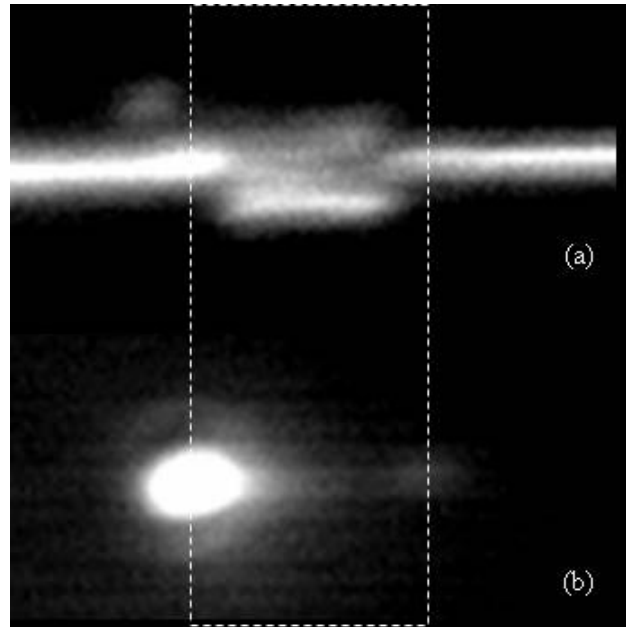


Figure 3. (a) Low resolution visible image of an adiabatic taper device shown in SEM of figure 1(a). (b) IR image of the same device while coupling 1453 nm laser light. The dotted line indicates the point of origin of the radiation on the visible image. Note that it does not originate from junction losses.

In conclusion, transmission measurements have revealed that at wavelengths where the photonic bandgap occurs, the adiabatic-taper and line-defect system exhibit increased transmission. This, in addition with radiation images, indicates that the adiabatic taper is an effective means of coupling light to a photonic crystal line-defect. Radiation images have also revealed an fabrication defect which we plan to correct so that we will have a suitable device for measurements of photonic crystal losses and near-field optical studies.

References

1. S. Rowson, A. Chelnokov, J.-M. Lourtioz, "Two-Dimensional Photonic Crystals in Macroporous Silicon: From Mid-Infrared to Telecommunications Wavelengths," *J. Lightwave Tech.* 17(11):1989-95 (1999).
2. T. F. Krauss, R. M. De La Rue, and S. Brand, "Two-Dimensional photonic-bandgap structures operating at near-infrared wavelengths," *Nature* 383(6602): 699-702 (1996).
3. S. Lin, E. Chow, V. Hietala, P. Villeneuve, J. D. Joannopoulos, "Experimental Demonstration of Guiding and Bending of Electromagnetic Waves in a Photonic Crystal" *Science*, 282(5387): 274-6 (1998).

Integrated Polarization Splitter and Rotator Designs

Sponsor

Pirelli Labs

U.S Air Force – Office of Scientific Research

Grant F49620-01-1-0084

Project Staff

Michael R. Watts, Prof. Hermann A. Haus, and Prof. Erich P. Ippen

High-index-contrast (HIC) dielectric waveguides exhibit highly confined optical modes. The tight confinement allows for waveguides to be spaced closely together without inducing cross-talk and the propagating field to be guided around sharp bends with minimal radiative loss. However, increased index contrast brings increased polarization sensitivity, a problem for the uncontrolled polarization state of the standard single mode fiber based communication link. To achieve polarization independence, we propose splitting the polarization states at the input, rotating one in order to obtain identical on chip polarizations, and operating on the two paths in parallel with identical structures. Dropped signals may be detected and recombined electronically while signals continuing in the optical domain are recombined using the reverse process. In order to implement this polarization diversity scheme, we have developed integrated polarization splitters and rotators.

Previously proposed integrated-optic devices for polarization rotation have been based on some form of mode-coupling [1-3]. For complete power transfer, the coupled modes must be phase-matched, and the degree of coupling precisely tuned to the structure length. Consequently, approaches based on mode-coupling are inherently fabrication sensitive. Additionally, the coupling strength tends to be wavelength-sensitive, a result that is not compatible with the broadband fields of wavelength division multiplexed systems.

Mode evolution based devices [4,5] only require the modes to evolve slowly in order to avoid exchanging substantial power with other modes in the system. As a result, mode evolution based devices are often largely insensitive to changes in wavelength and device dimensions. Mode evolution based polarization splitters have previously been proposed [4,5]. Recently, we presented an integrated approach for splitting and rotating polarization states through mode-evolution [6]. Our more recent designs provided herein have reduced the number of required lithographic layers from three to two while increasing the fabrication tolerances. Current designs are being readied for fabrication.

The polarization splitter is depicted in Fig. 1a. The device consists of a horizontally oriented rectangular waveguide in close proximity to a vertically oriented rectangular waveguide. The two guides are separated by a small gap and a smooth transition is made into the vertically oriented guide. The gap prevents a point of intersection which would likely result in an abrupt transition in the fabricated device due to limited resolution. The dimensions are chosen so that the fundamental output TE-like mode (TE) remains always in the horizontally oriented section while the fundamental TM-like mode (TM) adiabatically transitions from the horizontally oriented section to the vertically oriented section. Additionally, secondary TE-like (TE_V) and TM-like (TM_H) modes develop along the length of the structure (V and H subscripts denote modes of the vertical and horizontal waveguides, respectively). Coupling amongst the guided modes is mitigated by choosing a geometry that avoids nearly degenerate modes. For demonstration purposes, we have chosen to implement the structure in a silicon nitride ($n = 2.2$) and silica ($n = 1.445$) material system. The dimensions are $w_1 = 0.35\mu\text{m}$, $w_2 = 0.8\mu\text{m}$, $h = 0.4\mu\text{m}$, $s_1 = 0.25\mu\text{m}$, and $s_2 = 1.0\mu\text{m}$. Finite-difference-time-domain (FDTD) and eigenmode-expansion (EME) simulations were performed. FDTD results were obtained by separately launching the fundamental TE and TM input modes and monitoring the power in the fundamental and secondary TE and TM output modes. The EME results were obtained using only the guided modes. In order to minimize the

size of the FDTD computation grid, only the transition region was simulated (i.e. over the length L_1). EME simulations confirm that virtually all of the coupling occurs in this transition region. Both the FDTD and EME simulation results (Fig. 1b) indicate that longer device lengths (i.e. slower transitions) induce less crosstalk (TE to TE_V and TM to TM_H) and higher throughput (TE to TE_H and TM to TM_V). Essentially, as the device becomes longer, the coupling introduced by the transition is reduced and the modes have a chance to de-phase before substantial power exchange takes place. The performance of the device as a function of wavelength was obtained through a ratio of the discrete Fourier transforms (DFT) taken at the input and output ports during the FDTD simulation. A $50\mu\text{m}$ long input section (i.e. $L_1 = 50\mu\text{m}$, device length of $L_1(s_2+w_1-s_1)/w_1 = 157\mu\text{m}$) structure was simulated and the results are depicted in Fig. 1c. No discernable wavelength sensitivity is observed over the entire 1.45 to $1.65\mu\text{m}$.

Similarly, polarization rotation may be introduced through mode evolution. However, such a device must have a mode set with polarization states that evolve along the length of the transition. A twisted waveguide is such a device. However, standard micro-fabrication techniques dictate layer by layer construction making a pure twist next to impossible to fabricate on an integrated optic chip. Fortunately, as a result of Gauss' Electric Law for dielectrics, $\nabla \cdot \epsilon \mathbf{E} = 0$, the fundamental mode of a dielectric waveguide tends to possess a polarization state that is largely aligned to the principal axis of the structure. Consequently, with only a pair of waveguide core layers the polarization of the fundamental mode may be easily manipulated. We do so with the structure depicted in Fig 2a. Here, the layers are asymmetrically and oppositely tapered producing a "twist" of the waveguide in the electromagnetic sense. A large aspect ratio is chosen so as to inhibit coupling between the fundamental and secondary guided mode ($w_1 = 0.4\mu\text{m}$, $w_2 = 0.8\mu\text{m}$, $h = 0.4\mu\text{m}$). Here again a silicon nitride / silica material system was chosen. FDTD and EME simulations were performed as a function of the device length (Fig. 2b). FDTD results were obtained by launching a TM input mode and monitoring the power in the TE and TM output modes. The EME results were obtained using only the two guided modes. Both the FDTD and EME results of Fig. 1b indicate that power not transferred to the fundamental output mode is transferred to the secondary guided mode. As the device length increases, the coupling is reduced allowing the modes to de-phase before substantial power transfers between them. Thus, longer devices exhibit better performance. Device lengths of only a couple hundred microns are sufficient to ensure nearly ideal performance. Here again, the performance of the device as a function of wavelength was obtained through a ratio of a DFT taken at the input and output ports during the FDTD simulation. A $200\mu\text{m}$ long structure was simulated and the results are depicted in Figure 1c. No discernable wavelength sensitivity is observed over the entire 1.45 to $1.65\mu\text{m}$.

In conclusion, we have shown that efficient polarization splitting and rotating may be accomplished using the principle of mode evolution. FDTD and EME simulations indicate that devices of only a couple hundred microns are needed to ensure efficient operation and no significant wavelength sensitivity was observed. The device designs are compatible with e-beam lithography and standard fabrication processes.

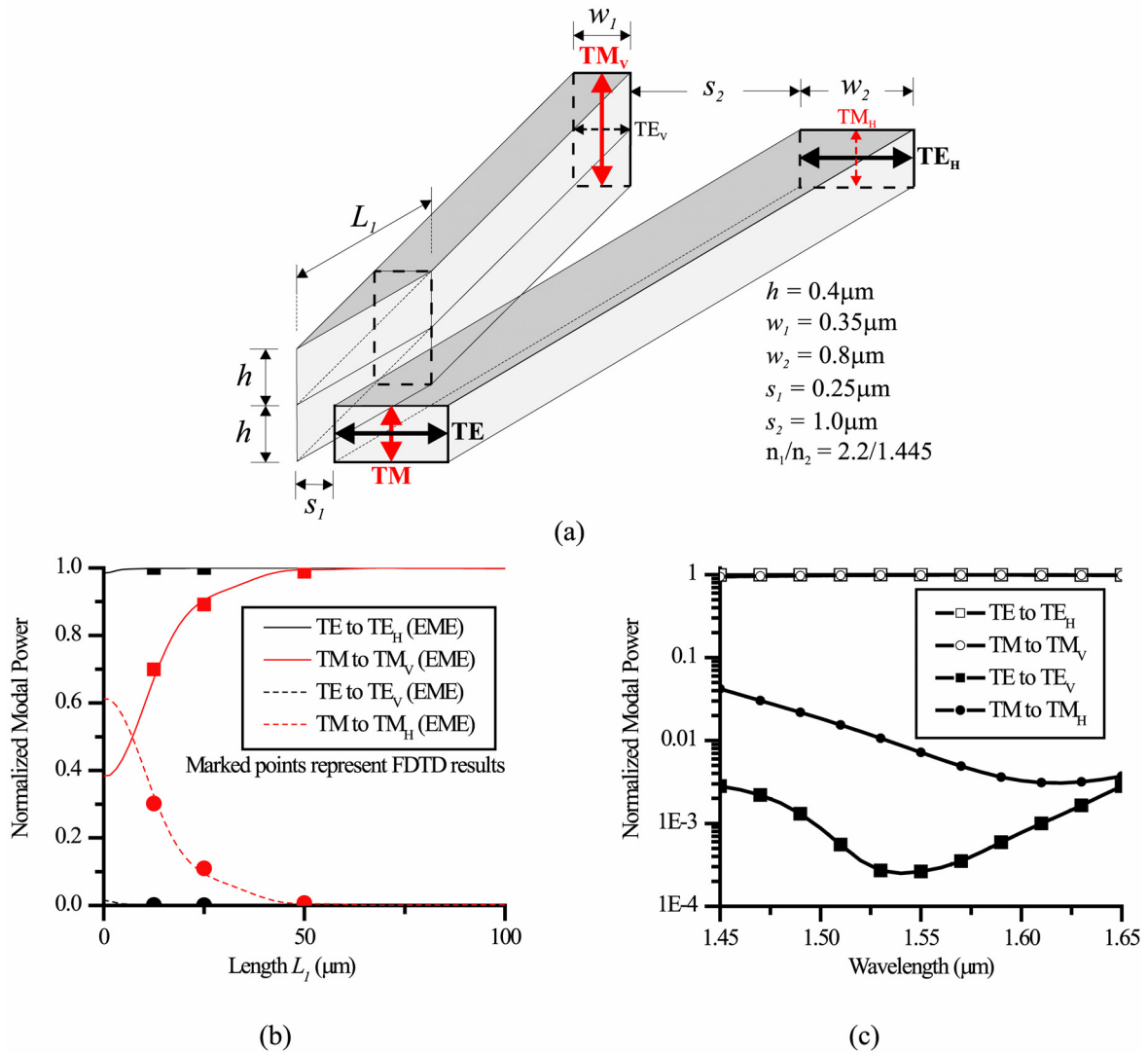


Fig. 1 (a) Polarization splitter, (b) FDTD and EME simulations as function of the length L_1 , and (c) wavelength dependence for $L_1 = 50 \mu\text{m}$ as determined from a FDTD simulation.

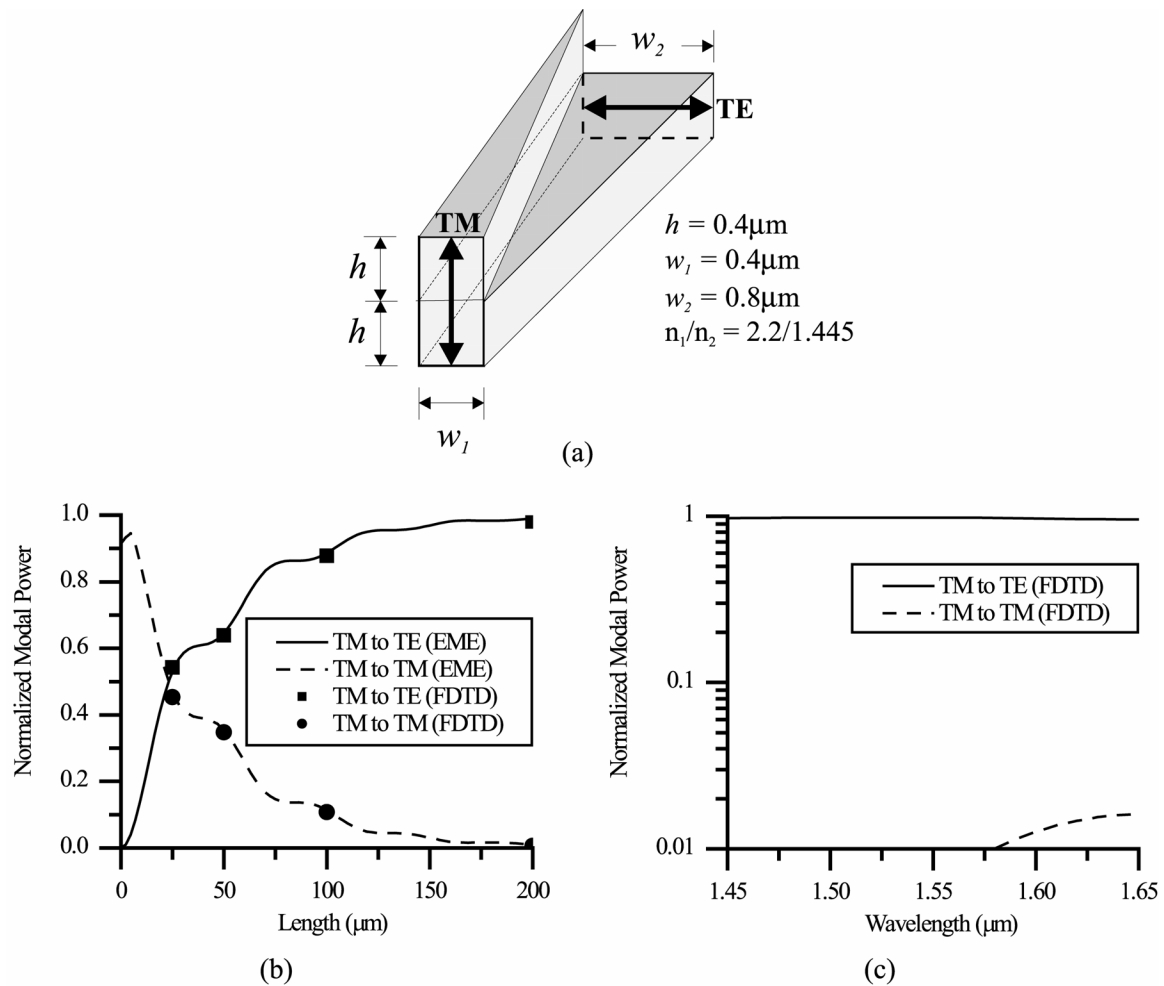


Fig. 2 (a) Polarization converter using tapering of the upper and lower waveguide core layers to produce chirality, (b) FDTD and EME simulation results of the polarization converter, and (c) wavelength dependence of a 200 μm long device as determined from a FDTD simulation.

References

1. Y. Shani, C. H. Henry, R. C. Kistler, R. F. Kazarinov and K. J. Orlowsky, "Integrated optic adiabatic polarization splitter on silicon," *Appl. Phys. Lett.* 56 (2), January 8, 1990.
2. R. M. de Ridder, A. F. M. Sander, A. Driessen, J. H. J. Fluitman, "An integrated optic adiabatic TE/TM mode splitter on silicon," *J. Lightwave Technol.* 11, 1806-1811, Nov. 1993
3. J. Z. Huang, R. Scarmozzino, G. Nagy, M. J. Steel, and R. M. Osgood, "Realization of a compact and single-mode optical passive polarization converter," *IEEE Photon. Technol. Lett.* 12, 317-319, March 2000.

Chapter 24. Optics and Quantum Electronics

4. V. P. Tzolov and M. Fontaine, "A passive polarization converter free of longitudinally periodic structure," *Optics Communications* 127, 7-13, Jun. 1996.
5. [5] W. W. Lui, T. Hirono, K. Yokoyama, and W. P. Huang, "Polarization rotation in semiconductor bending waveguides," *J. Lightwave Technol.* 16, 929-936, May 1998.
6. [6] M.R. Watts, H.A. Haus, G. Gorni, and M. Cherchi, "Polarization splitting and rotating through adiabatic transitions," *Proceedings of Integrated Photonics Research Conference 2003 (IPR 2003)*, pp. 26-28, 2003.

Patents (Pending)

1. M. R. Watts, M. Cherchi, and H. A. Haus, "An integrated optic polarization converter based on structural chirality"
2. M. R. Watts, "Wavelength insensitive integrated optic polarization splitter"

Optical Phase Control and Stabilization Techniques

Direct Frequency Comb Generation from an Octave-Spanning Ti:sapphire Laser

Sponsors

Office of Naval Research - N-00014-02-1-0717

National Science Foundation - ECS-0119452

Project Staff

Lia Matos, Onur Kuzucu, Thomas R. Schibli, Jungwon Kim, Professor Erich P. Ippen, Professor Daniel Kleppner and Professor Franz Kaertner

The use of femtosecond lasers for frequency comb generation has revolutionized frequency metrology [1,2]. Typical setups employ Ti:sapphire lasers producing 10-30 fs long pulses and spectral broadening in photonic crystal fiber to achieve an octave spanning spectrum necessary for f-to-2f self-referencing. However, external spectral broadening has been shown to introduce nonlinear phase noise into the comb spectrum [3] and coupling of the laser beam into the small core diameter of a high index contrast fiber limits the long-term stability of the overall system. The latter problem is of particular concern for the development of optical clocks (for which long term signal averaging is necessary).

We present octave spanning spectra generated by prism-less Ti:sapphire lasers operating at repetition rates of 80 MHz and 150 MHz. The 80 MHz version is self-referenced using the f-to-2f technique. The lasers consist of astigmatically compensated cavities, as shown in Figure 1a. All mirrors in the cavity, with exception of the end mirrors are double-chirped mirror pairs that generate smooth group delay dispersion when used in pairs. We used thin BaF₂ wedges for dispersion compensation because it has the lowest ratio of third to second order dispersion in the wavelength range from 600 – 1200 nm and the slope of the dispersion of BaF₂ is nearly identical to that of air. This allows for simple cavity length and repetition rate scaling without changing the overall intracavity dispersion. The compact prism-less design allows system scaling to GHz repetition rate. The output frequency comb of the 80 MHz laser is f_{ceo} stabilized directly by the f-to-2f method, (see Figure 1a). The carrier-envelope beat note of the laser is intrinsically stable with a S/N of 30 and 40 dB in a 100 kHz and 10kHz bandwidth, respectively, (see Figure 1b). In the absence of active feedback and without any temperature control of the laser breadboard the frequency stays within the bandwidth of the bandpass-filter following the PMT, which is 8MHz, for more than 10 hours. On the time scale of seconds, it can jitter by about 100 kHz.

Figure 2a and b show the spectrum under broadband operation of the 80 MHz and 150 MHz laser, respectively. The octave is reached at a spectral density about 25 dB below the average level. The same plots also show the OC transmission curves. To demonstrate control over the comb, we filter the component $f_{rep} + f_{ceo}$ at 130 MHz from the PMT signal of the 1f-2f interferometer and phase-lock it to a stable RF synthesizer using a phase-locked loop, (Fig. 1a).

Figure 3 shows the measured phase error spectral densities of the f_{ceo} beat with and without active stabilization. The integrated phase error for the in-loop measurement is 1.4 rad (from 50 mHz to 1MHz). The major contribution to this phase noise error comes from the pump noise shown in relative units in Figure 3. The spectral components from 1-10 kHz contribute 90 % of the phase error. However, this comb can be used for metrology as no cycle slips occur. An improved loop filter design for stronger noise suppression and a pump laser with lower noise to achieve lower residual carrier-envelope phase fluctuations are being implemented.

These results constitutes a major improvement over previous approaches: an octave spanning Ti:sapphire laser which used a combination of chirped mirrors and a prism pair to produce continuum directly in the oscillator [4.5].

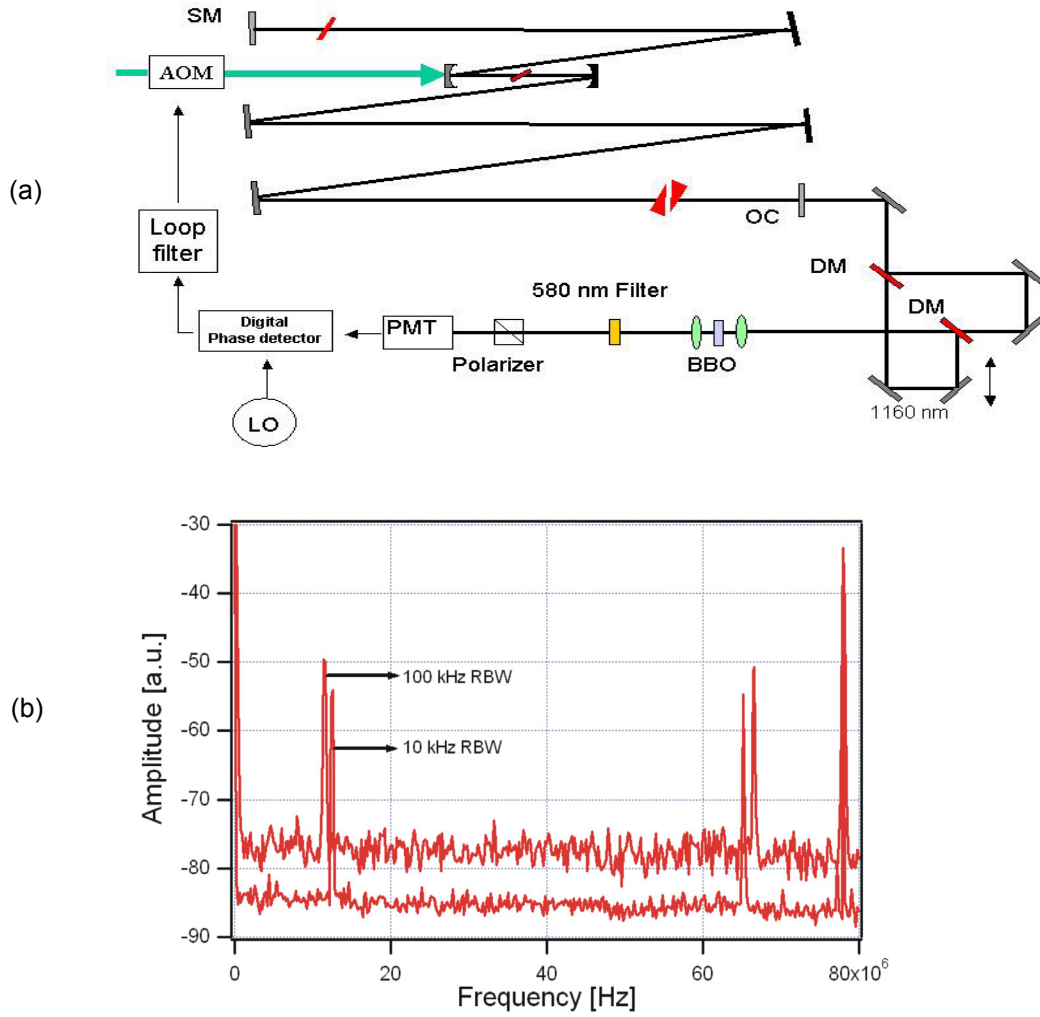


Figure 1: (a.) Schematic of octave spanning prism-less laser with f_{ceo} detection and lock (see text). Gray and black mirrors are type I and II DCMs respectively. The BaF₂ wedges are used for fine-tuning of the dispersion. (b) Measured carrier-envelope beat signal from the 80 MHz laser.

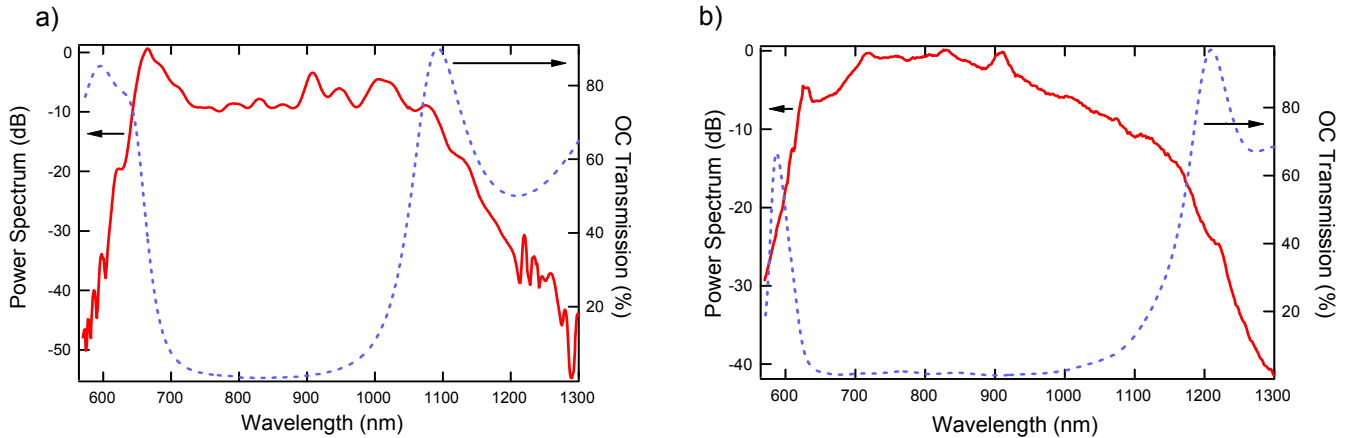


Figure 2 : Measured output spectrum for 80 MHz repetition rate (a) and 150 MHz repetition rate (b) lasers. In both cases the octave is reached at approximately 25 dB below the average power level. The average mode-locked power is 90 mW for both lasers. Also shown are the respective OC transmission curves for the ZnSe/MgF₂ Bragg-stack (a) and a broadband SiO₂/TiO₂ stack (b). Both have about 1% transmission at 800 nm.

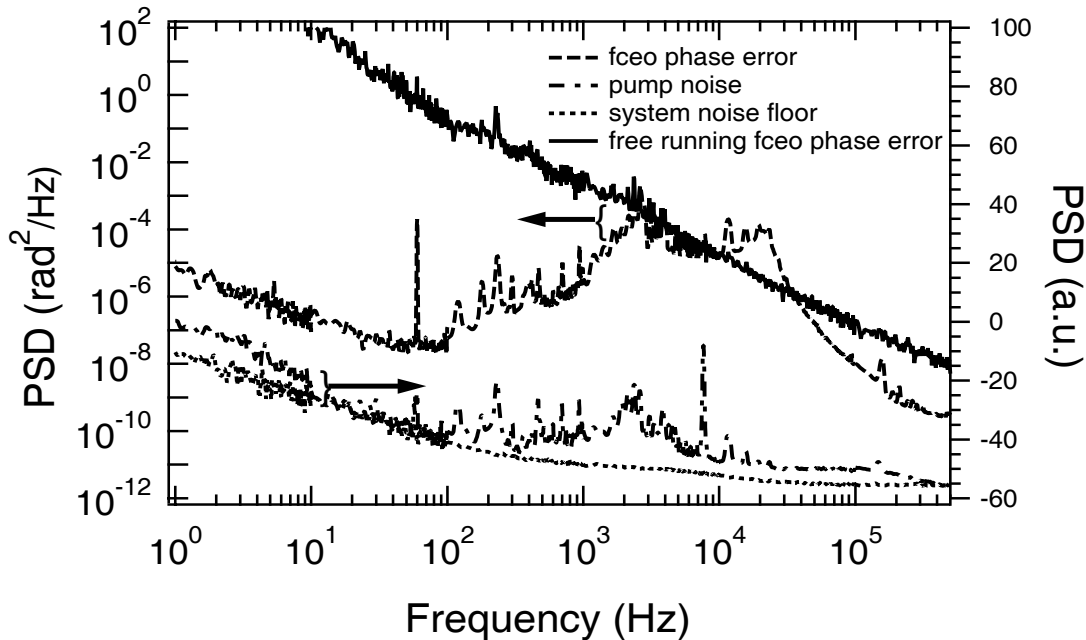


Figure 3: Spectral densities of the phase error signal at the output of the digital phase detector for the f_{ceo} lock (dashed line) and free running f_{ceo} (solid line), with scale on the left. Spectral density of the pump noise recorded in the absence of f_{ceo} feedback (dash-dotted line) and system noise floor (dotted line), with scale on the right. The major contribution to f_{ceo} noise is due to pump noise.

References

1. D. J. Jones, S. A. Diddams, J. K. Ranka, A. Stentz, R. S. Windeler, J. L. Hall, S. T. Cundiff, *Science* 288, 635-639 (2000).
2. R. Holzwarth, T. Udem, T. W. Haensch, J. C. Knight, W. J. Wadsworth, and P. S. J. Russell, *Phys. Rev. Lett.* 85, 2264-2267 (2000).
3. Tara M. Fortier, Jun Ye, Stephen T. Cundiff and Robert S. Windeler, *Opt. Lett.* 27, 445-447 (2002).
4. R. Ell, U. Morgner, F. X. Kaertner, J. G. Fujimoto, E. P. Ippen, V. Scheuer, G. Angelow, and T. Tschudi, *Opt. Lett.* 26, 373-375, 2001.
5. T. M. Fortier, D. J. Jones and S. T. Cundiff, "Phase stabilization of an octave spanning Ti:sapphire Laser," to be published in *Optics Letters*.

Optical Clockwork without the Need for Carrier-Envelope Phase Control

Sponsors

Office of Naval Research - N00014-02-1-0717

Air Force Office of Scientific Research - F49620-01-1-0084

Project Staff

Dr. Oliver D. Mücke, Onur Kuzucu, Dr. Franco N. C. Wong, Professor Erich P. Ippen, Professor Franz X. Kaertner, Seth M. Foreman, Professor David J. Jones, Professor Long-Sheng Ma, Professor John L. Hall, and Professor Jun Ye

Motivation

Femtosecond-laser based optical frequency combs have recently revolutionized the field of precision optical frequency metrology and enabled the construction of optical atomic clocks [1,2]. In this project, we demonstrate an optical clockwork without the need for carrier-envelope phase control, simplifying the implementation of the clockwork and avoiding the necessity of an octave-spanning spectrum.

Recently, A. Baltuška *et al.* [3] have shown that the phase relationship between pump, signal, and idler pulses in a parametric interaction enables the generation of a carrier-envelope phase independent idler pulse. Similarly, by using difference-frequency generation (DFG) between different spectral portions of the same frequency comb, a carrier-envelope frequency independent DFG comb in the infrared spectral region with excellent accuracy and stability can be generated [4]. Equivalently, sum-frequency generation (SFG) between an infrared frequency standard (e.g., a methane-stabilized Helium Neon laser at $3.39\ \mu\text{m}$ [5]) and the long-wavelength portion of a frequency comb yields an SFG comb with carrier-envelope frequency f_0 . If the SFG comb overlaps spectrally with the short-wavelength portion of the comb, a carrier-envelope frequency independent optical clockwork can be realised [6]. In this project, we implement such an optical clockwork based on SFG between a continuous-wave optical parametric oscillator (OPO) at $3.39\ \mu\text{m}$ idler wavelength and a custom-tailored mode-locked Ti:sapphire laser with two dominant spectral peaks near $834\ \text{nm}$ and $670\ \text{nm}$. Our experimental setup is shown in Fig. 1.

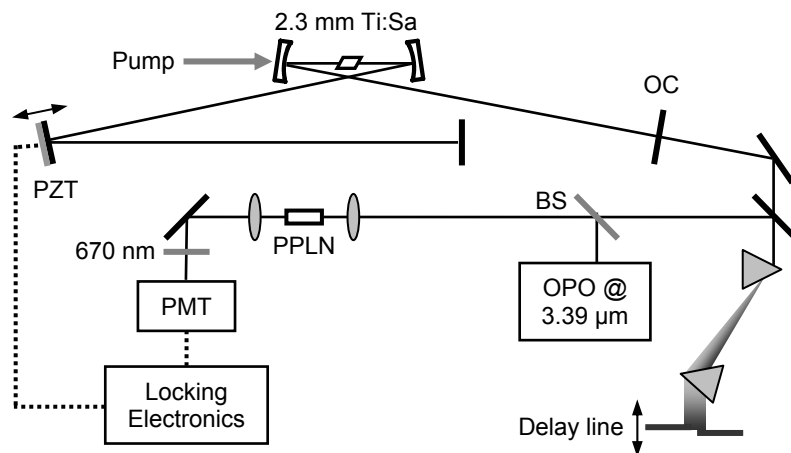


Figure 1: Scheme for SFG-based optical heterodyne beat for the implementation of an optical clock without carrier-envelope phase control. Note $3.39\ \mu\text{m} + 834\ \text{nm} \rightarrow 670\ \text{nm}$. All intracavity mirrors are double-chirped mirrors (DCMs).

The spectrum of the Ti:sapphire laser (Fig. 2) is generated using a narrowband output coupler. A transmission of about 1% occurs at the center of the output coupler. The coupler rolls off strongly at the designated wavelengths of $690\ \text{nm}$ and $866\ \text{nm}$. At these wavelengths the transmission increases to 5% leading to two pronounced spectral peaks in the output spectrum. The Ti:sapphire laser operates at a repetition frequency f_{rep} of $78\ \text{MHz}$ with an average output power

of typically 150 mW. In the experiment, we also use a commercial narrow-linewidth, singly resonant OPO with a resonated pump, which is based on a periodically-poled lithium niobate (PPLN) crystal. The OPO cavity length is locked to the pump laser by using the Pound–Drever–Hall stabilization technique. Using a 40 mm focal length calcium fluoride lens, the 28 mW of output power of the Ti:sapphire laser near 834 nm and the 16 mW idler output at 3.39 μm are focused into a 5mm long PPLN crystal (16.2 μm quasi-phase matching period) heated to 130°C. The corresponding phase matching bandwidth of this PPLN crystal is around 1 THz. The generated SFG comb and the original Ti:sapphire comb at 670 nm are temporally and spatially overlapped with the aid of a prism-based delay line (compare Fig. 1).

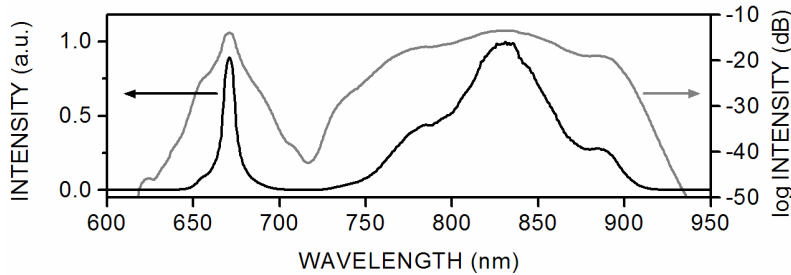


Figure 2: Output spectrum of the Ti:sapphire laser. The wings of the spectrum at 670 nm and 834 nm are enhanced due to the roll-off of the output coupler. The height of the short-wavelength peak is very sensitive to intracavity dispersion.

Results

A heterodyne beat signal between the two combs is detected by a photomultiplier with a signal-to-noise ratio of ~ 25 dB in a 30 kHz resolution bandwidth (Fig. 3(a)). Note that the final beat signal results from the coherent superposition of many comb lines. Importantly, frequency variation of this beat signal depends only on the laser repetition frequency f_{rep} but *not* on the carrier-envelope frequency f_0 . By phase locking this beat signal to a radio-frequency reference using an rf tracking filter, we lock the Ti:sapphire repetition frequency f_{rep} directly to the OPO optical frequency f_{idler} (Fig. 3(b)). The drift and small sinusoidal fluctuations in the stabilized repetition frequency are due to those of the OPO Nd:YAG pump laser.

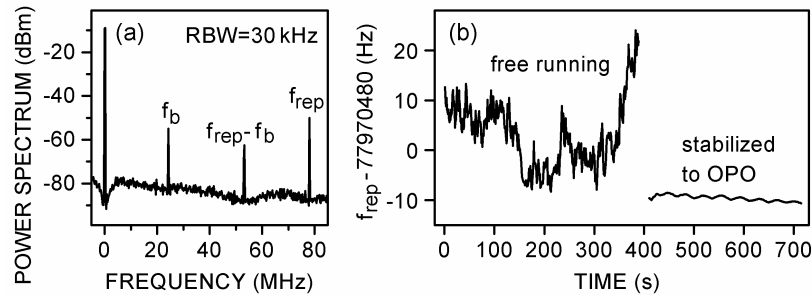


Figure 3: (a) Heterodyne beat between the SFG comb and the original comb. (b) Frequency counting of the laser repetition frequency f_{rep} under free-running conditions and while stabilized to the continuous-wave OPO.

References:

1. S. A. Diddams, T. Udem, J. C. Bergquist, E. A. Curtis, R. E. Drullinger, L. Hollberg, W. M. Itano, W. D. Lee, C. W. Oates, K. R. Vogel, and D. J. Wineland, *Science* 293, 825 (2001).
2. J. Ye, L. S. Ma, and J. L. Hall, *Phys. Rev. Lett.* 87, 270801 (2001).
3. A. Baltuška, T. Fuji, and T. Kobayashi, *Phys. Rev. Lett.* 88, 133901 (2002).
4. M. Zimmermann, C. Gohle, R. Holzwarth, T. Udem, and T. W. Hänsch, *Opt. Lett.* 29, 310 (2004).
5. M. A. Gubin, D. A. Tyurikov, A. S. Shelkovnikov, E. V. Koval'chuk, G. Kramer, and B. Lippardt, *IEEE J. Quantum Electron.* 31, 2177 (1995).
6. A. Amy-Klein, A. Goncharov, C. Daussy, C. Grain, O. Lopez, G. Santarelli, C. Chardonnet, *Appl. Phys. B* 78, 25 (2004).

Femtosecond Synchronization of RF-Signals with Optical Pulse Trains

Sponsors

Office of Naval Research (ONR) N00014-02-1-0717

Air Force Office of Scientific Research (AFOSR) FA9550-04-1-0011

Project Staff

Jung-Won Kim, Professor Michael H. Perrott, Professor Franz X. Kaertner

The extraction of a microwave signal from an optical pulse train emitted by a mode-locked laser using direct photo-detection is limited in precision by excess noise [1]. We propose a novel synchronization scheme avoiding these limitations [2]. The scheme can be applied to extract microwave signals from optical clocks based on femtosecond laser, or to synchronize one or multiple mode-locked lasers to an RF-signal. As the first experimental demonstration, sub-100 fs timing jitter between the extracted RF-signal and the optical pulse train is demonstrated. Numerical simulations show that scaling to potentially sub-femtosecond precision is possible.

The general idea for suppression of excess noise due to the photo-detection process is the transfer of timing information into an intensity imbalance in the optical domain. This can be realized by a Sagnac-loop interferometer with a phase modulator in the loop. Figure 1 shows the synchronization scheme with the measurement set-up. A 100 MHz repetition rate Ti:sapphire mode-locked laser is used as the pulse source. A resonant phase modulator at 2 GHz is positioned in the Sagnac-loop in such a way that the optical delay between counter propagating pulses at the phase modulator is set to half of the RF-signal period, i.e. 0.5 ns for the current 2 GHz VCO. This assures that the two pulses experience opposite phase modulation. The output beams are detected by a balanced detector which drives the VCO after proper filtering. For a stable and drift-free biasing of the interferometer, a quarter-wave plate is inserted in one of the beams using a thin-film coating covering only half of the substrate. A very stable and drift free phase-locked operation is achieved with this scheme.

The measured single-sideband phase noise spectra from 1 Hz to 10 MHz are shown in Figure 2. Curve (1) shows the phase noise spectrum of the free-running VCO measured with the commercial phase noise measurement system. Curve (2) shows the phase noise measured by the same method when the system is locked. The locking is clearly visible in the spectrum covering the range of 100 kHz to 10 MHz. At lower frequencies, the phase noise of the Ti:sapphire pulse train dominates. To verify this assumption, we measured the relative phase noise between the pulse train and the RF-signal by mixing VCO output in quadrature with the same frequency component from direct detection. The result is shown in curve (3) of Fig. 2. Due to the noise floor of the vector signal analyzer (curve (4) in Fig. 2) and excess noise in the photo-detector that generates the reference signal, the high frequency noise floor is increased in comparison to the first method. But this measurement clearly shows that the noise increase at low frequency in curve (2) is the phase noise of the free-running Ti:sapphire laser [3]. The origin of the enhanced phase fluctuations below 1 kHz may be due either to mechanical vibrations in the Sagnac-loop or excess phase noise in the photo-detection process that converts enhanced laser amplitude fluctuations into phase fluctuations. The relative timing jitter between the RF-signal and the pulse train integrated from 100 Hz to 10 MHz can be estimated by the area underneath curve (5), which lines up with the high frequency noise of the first measurement (curve (2) in Fig. 3) and results in about 60 fs timing jitter.

With improved system design and implementation, it is expected that this method is able to reduce the relative jitter between an RF-signal and an optical pulse train to the sub-femtosecond range, which has been so far only achieved by purely optical means [4].

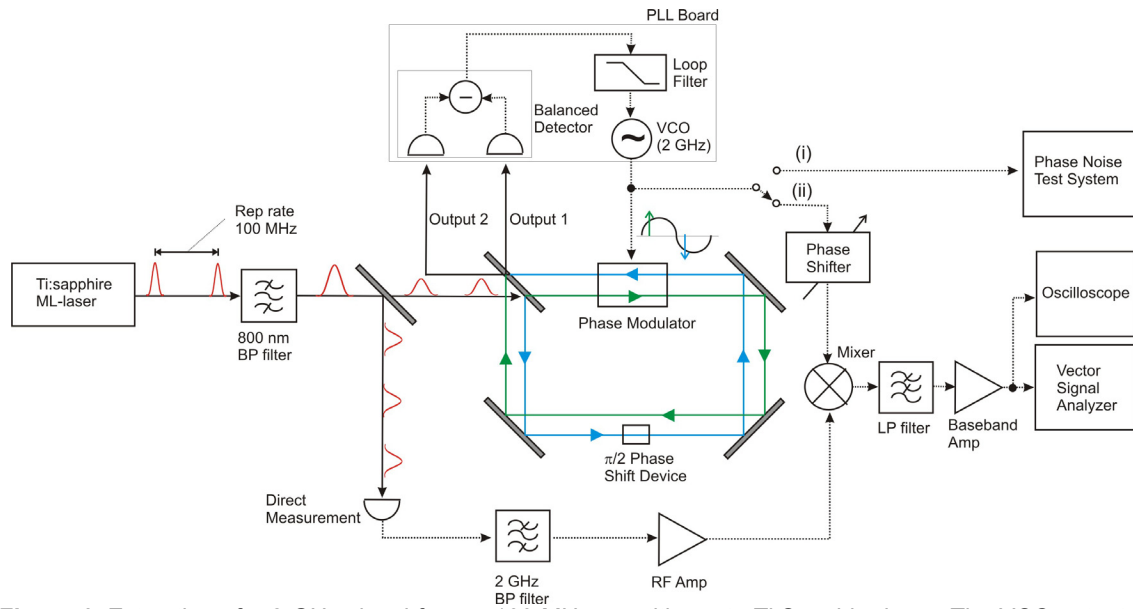


Figure 1. Extraction of a 2 GHz signal from a 100 MHz repetition rate Ti:Sapphire laser. The VCO output is characterized (i) by a commercial phase noise test system and (ii) by mixing in quadrature with the 2 GHz component of the directly detected signal. The resulting signal is measured with a vector signal analyzer. The normalization constant for calibration to the RF-phase is measured independently with an oscilloscope.

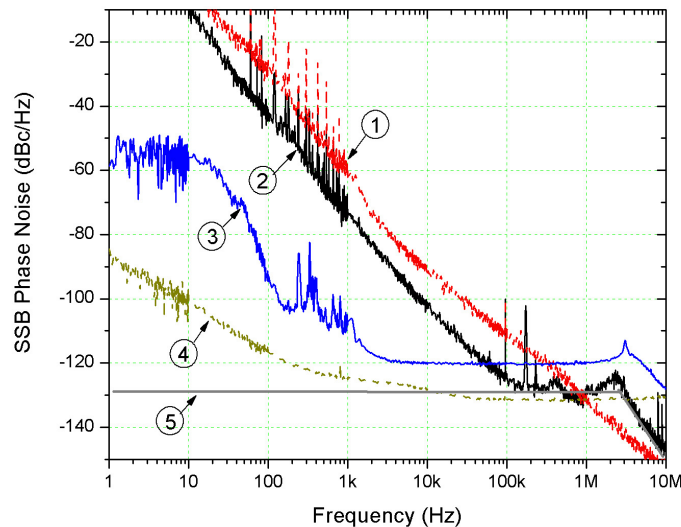


Figure 2. Measured single-sideband phase noise of (1) the free-running VCO and (2) the locked VCO using a commercial phase noise measurement system. Curve (3) shows the measured single-sideband phase noise between extracted RF-signal and the 20th harmonic of directly detected pulse train using a mixer and vector signal analyzer. Curve (4) shows the noise floor of the vector signal analyzer. Curve (5) shows the estimated phase noise level of extracted RF-signal from result of curve (2).

References:

1. E. N. Ivanov, S. A. Diddams, and L. Hollberg, *IEEE J. Sel. Top. Quant. Elec.* 9, 1059-1065 (2003).
2. J. Kim, M.H. Perrott, F.X. Kaertner, submitted to *Opt. Lett.* (2004).
3. R. P. Scott, C. Langrock, and B. H. Kolner, *IEEE J. Sel. Top. Quant. Elec.* 7, 641-655 (2001).
4. T.R. Schibli, J. Kim, O. Kuzucu, J.T. Gopinath, S.N. Tandon, G.S. Petrich, L.A. Kolodziejski, J.G. Fujimoto, E.P. Ippen, and F.X. Kaertner, *Opt. Lett.* 28, 947-949 (2003).

Publications, Presentations, and Thesis, Books

Publications

1. Th. Tritschler, O. D. Mücke, M. Wegener, U. Morgner, and F. X. Kaertner, "Evidence of third-harmonic generation in disguise of second harmonic generation in extreme nonlinear optics," *Phys. Rev. Lett.* 90(21): 217404-07 (2003).
2. T. R. Schibli, J. Kim, O. Kuzucu, J. T. Gopinath, S. N. Tandon, G. S. Petrich, L. A. Kolodziejski, J. G. Fujimoto, E. P. Ippen, and F. X. Kaertner, "Attosecond active synchronization of passively mode-locked lasers using balanced cross-correlation," *Opt. Lett.*, 28(11): 947-949 (2003).
3. Ch. Jirauschek, U. Morgner and F. X. Kaertner, "Spatio-temporal Gaussian pulse dynamics in Kerr-lens mode-locked lasers," *J Opt. Soc. Am. B* 20(6): 1356-1268 (2003).
4. P. Wagenblast, R. Ell, U. Morgner, F. Grawert and F. X. Kaertner, "10-fs, diode-pumped Cr³⁺:LiCAF laser," *Opt. Lett.* 28(18): 1713-15 (2003).
5. W. Seitz, R. Ell, U. Morgner and F. X. Kaertner, "All-optical Synchronization and Mode-Locking of Solid-State Lasers with Nonlinear Semiconductor Fabry-Perot Mirrors," *IEEE J. Sel. Top. Quantum Electron.* 9(4): 1093-1101 (2003).
6. A. Sennaroglu*, A. M. Kowalevicz, F. X. Kaertner, and J. G. Fujimoto, "High performance, compact, prismless, low-threshold 30 MHz Ti:Al₂O₃ laser," *Opt. Lett.* 28(18): 1674-76, (2003).
7. A.M. Kowalevicz, A. T. Zare, F. X. Kaertner, J. G. Fujimoto, S. Dewald, U. Morgner, V. Scheuer, and G. Angelow, "Generation of 150-nJ pulses from a multiple-pass cavity Kerr-lens modelocked Ti:Al₂O₃ oscillator," *Opt. Lett.*, 28(17): 1507-09 (2003).
8. T. R. Schibli, O. Kuzucu, J. Kim, E. P. Ippen, J. G. Fujimoto, and F. X. Kaertner, V. Scheuer, G. Angelow, "Towards Single-Cycle Laser Systems," Invited paper *IEEE J. Sel. Top. Quantum Electron.* 9(4): 990-1001 (2003).
9. S. Bourquin, R. Prasankumar, F. X. Kaertner, J. G. Fujimoto, S. Lasser and Salathe, "High-speed femtosecond pump-probe spectroscopy with a smart pixel detector array," *Opt. Lett.* 28(17): 1588-90 (2003).
10. K. Minoshima, A.M. Kowalevicz, I. Hartl, E.P. Ippen, and J.G. Fujimoto, "Photonic device fabrication with femtosecond laser oscillators," *Opt. and Photon. News*, 43-47, May 2003.
11. A. Sennaroglu and J.G. Fujimoto, "Design criteria for Herriott-type multi-pass cavities for ultrashort pulse lasers," *Opt. Exp.* 11, 1106-1113, May 2003.
12. R.P. Prasankumar, Y. Hirakawa, A.M. Kowalevicz Jr., F.X. Kärtner, J.G. Fujimoto, and W.H. Knox, "An extended cavity femtosecond Cr:LiSAF laser pumped by low cost diode lasers," *Opt. Exp.* 11, 1265-1269, May 2003.
13. T.R. Schibli, J. Kim, O. Kuzucu, J.T. Gopinath, S.N. Tandon, G.S. Petrich, L.A. Kolodziejski, J.G. Fujimoto, E.P. Ippen, and F.X. Kaertner, "Attosecond active synchronization of passively mode-locked lasers by balanced cross correlation," *Opt. Lett.* 28, 947-949, June 2003.
14. T.R. Schibli, O. Kuzucu, J. Kim, E.P. Ippen, J.G. Fujimoto F.X. Kaertner, V. Scheuer and G. Angelow, "Towards single-cycle laser systems," *IEEE J. Selected Topics Quant. Electron.*, 9, 990-1001, July/August 2003.
15. S. Bourquin, R.P. Prasankumar, F X. Kärtner, J.G. Fujimoto, T. Lasser, and R.P. Salathé, "High-speed femtosecond pump-probe spectroscopy using a smart pixel detector array," *Opt. Lett.* 28, 1588-1590, September 2003.
16. A.M. Kowalevicz, Jr., A.T Zare, F.X. Kärtner, J.G. Fujimoto, S. Dewald, U. Morgner, V. Scheuer, and G. Angelow, "Generation of 150-nJ pulses from a multiple-pass cavity Kerr-lens mode-locked Ti:Al₂O₃ oscillator," *Opt. Lett.* 28, 1597-1599, September 2003.
17. A. Sennaroglu, A.M. Kowalevicz, F.X. Kaertner, and J.G. Fujimoto, "High-performance, compact, prismless, low-threshold 30-MHz Ti:Al₂O₃ laser," *Opt. Lett.* 28, 1674-1676, September 2003.
18. S. Bourquin, A.D. Aguirre, I. Hartl, P. Hsiung, T.H. Ko, and J.G. Fujimoto, "Compact broadband light source for ultrahigh resolution optical coherence tomography imaging

- using a femtosecond Nd:Glass laser and a nonlinear fiber,” *Opt. Exp.* **11**, 3290-3297, December 2003.
19. R.P. Prasankumar, I. Hartl, J.T. Gopinath, E.P. Ippen, J.G. Fujimoto, P. Mak, and M.F. Ruane, “Design and characterization of semiconductor-doped silica film saturable absorbers,” *JOSA B* **21**, 851-857, April 2004.

Journal Articles, Accepted for Publication

1. L. Matos, O. Kuzucu, T. R. Schibli, J. Kim, E. P. Ippen, D. Kleppner and F. X. Kaertner, “Direct frequency comb generation from an octave-spanning, prism-less Ti:sapphire laser,” *Opt. Lett.*, forthcoming.
2. Y. Takushima, H. A. Haus and F. X. Kaertner, “The noise of ultrashort pulse mode-locked lasers beyond the slowly-varying envelope approximation,” *J. Opt. Soc. Am. B.*, forthcoming.
3. A. Soibel, F. Capasso, Cl. Gmachl, M. L. Peabody, A. M. Sergent, R. Paiella, H. Y. Hwang, D. L. Sivco, A. Y. Cho, h. C. Liu, ch. Jirauschek and F. X. Kaertner, “Active mode locking of broadband Quantum Cascade Lasers,” *IEEE J. Quantum Electron.*, forthcoming.
4. A. Sennaroglu, A.M. Kowalewicz, E.P. Ippen, and J.G. Fujimoto, “Compact femtosecond lasers based on novel multi-pass cavities,” *IEEE J. Quant. Electron.*, forthcoming.

Journal Articles, Submitted for Publication

1. O. D. Mücke, Th. Tritschler, M. Wegener, U. Morgner, and F. X. Kaertner, G. Kithrova and H. M. Gibbs, “Carrier-wave Rabi flopping: Role of carrier-envelope phase,” submitted to *Opt. Lett.*
2. J. Kim, M. H. Perrott and F. X. Kaertner, “Femtosecond synchronization of RF-signals with optical pulse trains,” submitted to *Opt. Lett.*

Meeting Papers

1. S. Bourquin, I. Hartl, A. D. Aguirre, P. Hsiung, T. H. Ko, J. G. Fujimoto, T. A. Birks, W. J. Wadsworth, U. Buenting, D. Kopf, “Portable broadband light sources using a femtosecond Nd:Glass laser and nonlinear fiber for ultrahigh resolution OCT imaging,” SPIE International Biomedical Optics Symposium, BIOS’2003, San Jose, California, January 25-31, 2003, paper 4956-03.
2. U. Morgner, P. Wagenblast, R. Ell, W. Seitz, and F. X. Kaertner, “Broadband laser light sources for commercial and biomedical applications,” SPIE Conference Photonics West, San Jose, January 25-31, 2003.
3. P. Hsiung, K. Schneider, P. R. Herz, S. Bourquin, T. H. Ko, X. Li, J. G. Fujimoto, M. E. Weinstein, M. S. Hirsch, A. D’Amico, J. Richie, “Ultrahigh resolution OCT of prostate pathology in the clinic using a portable Cr:forsterite laser,” SPIE International Biomedical Optics Symposium, BIOS’2003, San Jose, California, January 25-31, 2003, paper 4956-16.
4. W. Seitz, T. R. Schibli, U. Morgner, F. X. Kaertner, Ch. Lange, W. Richter, and B. Braun, “All-Optical Active Modelocking of a ps-Nd:YVO4-laser,” Advanced Solid-State Photonics 2003, San Antonio, Texas, Feb. 2-5, 2003.
5. T. R. Schibli, J. Kim, O. Kuzucu, J. T. Gopinath, S. N. Tandon, G. S. Petrich, L. A. Kolodziejski, J. G. Fujimoto, E. P. Ippen, and F. X. Kaertner, “Attosecond active synchronization of passively mode-locked lasers using balanced cross-correlation,” Postdeadline Paper Advanced Solid-State Photonics 2003, San Antonio, Texas, Feb. 2-5, 2003.

6. Th. Tritschler, O. D. Mücke, U. Morgner, F. X. Kaertner, and M. Wegener, "Role of carrier-envelope phase in few-cycle nonlinear optics in ZnO," SPIE Conference Photonics West, San Jose, January 25-31, 2003.
7. T.H. Ko, J.S. Schuman, J.G. Fujimoto, L.A. Paunescu, A.M. Kowalewicz, I. Hartl, W. Drexler, J. Duker, G. Wollstein, and H. Ishikawa, "Comparison of ultrahigh resolution and standard optical coherence tomography for imaging retinal pathologies," Association for Research in Vision and Ophthalmology, ARVO, Fort Lauderdale, Florida, May 4-9, 2003, paper 3277.
8. J.G. Fujimoto, T.H. Ko, J.S. Schuman, J. Duker, L.A. Paunescu, A.M. Kowalewicz, I. Hartl, W. Drexler, H. Ishikawa, and G. Wollstein, "Comparative study of macular holes using ultrahigh resolution and standard optical coherence tomography," Association for Research in Vision and Ophthalmology, ARVO, Fort Lauderdale, Florida, May 4-9, 2003, board B520.
9. Y. Takushima, H. A. Haus and F. X. Kaertner, "Quantum "Ultraviolet Catastrophe" of the Electromagnetic Field and Ultra-Short Mode-Locked Laser Noise," Conference on Fluctuations and Noise, Santa Fe, June 1-6, 2003.
10. S. Bourquin, P. Hsiung, I. Hartl, A. Aguirre, T.H. Ko, J.G. Fujimoto, T.A. Birks, W.J. Wadsworth, U. Buenting, and D. Kopf, "Compact ultrahigh resolution OCT system for real-time in vivo imaging," Conference on Lasers and Electro-Optics, CLEO, June 1-6, 2003, Baltimore, Maryland, paper CMU1.
11. A. Sennaroglu, A.M. Kowalewicz, Jr., F.X. Kaertner, and J.G. Fujimoto, "Compact prismless low-threshold 30 MHz femtosecond Ti:Al₂O₃ laser," Conference on Lasers and Electro-Optics, CLEO, June 1-6, 2003, Baltimore, Maryland, paper CFA1.
12. R.P. Prasankumar, Y. Hirakawa, A.M. Kowalewicz, Jr., F.X. Kaertner, J.G. Fujimoto, U. Morgner, and W.H. Knox, "An 8.6 MHz extended cavity femtosecond Cr:LiSAF laser pumped by single spatial mode diodes," Conference on Lasers and Electro-Optics, CLEO, June 1-6, 2003, Baltimore, Maryland, paper CFA2.
13. O. D. Mücke, Th. Tritschler, M. Wegener, U. Morgner, and F. X. Kaertner, G. Khitrova and H. M. Gibbs "The carrier-wave Mollow triplet in experiments on GaAs excited by 5fs pulses," International Quantum Electronics and Laser Science Conference (QELS 2003), Baltimore, MD, June 1-6, 2003.
14. T. R. Schibli, J.-W. Kim, L. Matos, A. W. Killi, J. Gopinath, G. Petrich, S. Tandon, J. G. Fujimoto, E. P. Ippen, F. X. Kaertner and L. A. Kolodziejski, "300 Attosecond active synchronization of passively mode-locked lasers using balanced cross-correlation," Conference on Lasers and Electro-Optics (CLEO 2003), Baltimore, MD, June 1-6, 2003.
15. L. Matos, O. Kuzucu, T. R. Schibli, J. G. Fujimoto, E. P. Ippen, F. X. Kaertner G. Angelow and V. Scheuer, "Direct Frequency Comb Generation from an Octave Spanning Prismless Ti:sapphire Laser," postdeadline paper Conference on Lasers and Electro-Optics (CLEO 2003), Baltimore, MD, June 1-6, 2003.
16. P. Wagenblast, U. Morgner, F. Grawert and F. X. Kaertner, "12-fs, diode-pumped Cr³⁺:LiCAF laser," Conference on Lasers and Electro-Optics (CLEO 2003), Baltimore, MD, June 1-6, 2003.
17. F. X. Kaertner, T. R. Schibli, O. Kuzucu, J. Kim, L. Matos, J. G. Fujimoto and E. P. Ippen, "Octave-Spanning Lasers and Single-Cycle Pulse Synthesis," 2003 IEEE LEOS Summer Topical Meeting on Photonic Time/Frequency Measurement and Control (PTFMC), Vancouver, Canada, July 13-16, 2003.
18. Ch. Jirauschek, J. Chandalia, L. Duane, F. X. Kaertner, O. D. Muecke, T. Tritschler and M. Wegener, "Opto-Electronic Carrier-Envelope-Phase Detection" 2003 IEEE LEOS Summer Topical Meeting on Photonic Time/Frequency Measurement and Control (PTFMC), Vancouver, Canada, July 13-16, 2003.
19. M. Wegener, T. Tritschler, O. D. Mücke, U. Morgner and F. X. Kaertner, "Determining the carrier-envelope frequency and phase by few-cycle nonlinear optics in semiconductors," (Invited Talk) International Quantum Electronics and Laser Science Conference (QELS 2003), Baltimore, MD, June 1-6, 2003.
20. F. X. Kaertner, "Octave Spanning Lasers and Single-Cycle Pulse Synthesis," Stanford Photonics Research Meeting, Stanford, CA, Sept. 5-17, 2003.

21. F. X. Kaertner, T. R. Schibli, O. Kuzucu, J. Kim, L. Matos, J. G. Fujimoto and E. P. Ippen, "Towards Single-Cycle Optical Pulses," OSA Annual Meeting 2003, Tucson, Arizona, Oct. 2-6, 2003.
22. F. X. Kaertner, L. Matos, J. Kim, O. Kuzucu, T. R. Schibli, J. G. Fujimoto and E. P. Ippen, "An Octave Spanning Prismless Ti:sapphire Laser as Direct Frequency Comb Generator," IEEE LEOS Annual Meeting 2003, Tucson, Arizona, Oct. 25-29, 2003.
23. T.H. Ko, A.M. Kowalevich, Jr., A. Paunescu, J.S. Schuman, W. Drexler, I. Hartl, F. Kaertner, and J.G. Fujimoto, "Ultrahigh resolution OCT imaging of retinal pathology in the ophthalmology clinic," European Conference on Biomedical Optics, Munich, Germany, June 22-25, 2003, 5140-26.
24. T.H. Ko, A.M. Kowalevich, Jr., A. Paunescu, J.S. Schuman, W. Drexler, I. Hartl, F. Kaertner, and J.G. Fujimoto, "Ultrahigh resolution OCT imaging of retinal pathology in the ophthalmology clinic," European Conference on Biomedical Optics, Munich, Germany, June 22-25, 2003, 5140-26.
25. T. H. Ko, A. Paunescu, I. Hartl, A. Kowalevich, J. Duker, J. Schuman, W. Drexler, A. Rogers, C. Baumal, E. Reichel, L.P. Aiello, S. Bursell, J. Fujimoto, "Comparing ultrahigh resolution optical coherence tomography and StratusOCT imaging of retinal pathologies," SPIE International Biomedical Optics Symposium, BIOS'2004, San Jose, California, January 24-29, 2004, paper 5314-22.
26. A. Sennaroglu, A. M. Kowalevich, F. X. Kaertner, E. P. Ippen, and J. G. Fujimoto, "Novel Compact Femtosecond Lasers Based on Multi-Pass Cavities," Advanced Solid-State Photonics 2004, Santa Fe, Colorado, Feb. 1-4, 2004.
27. F. X. Kaertner, "Mode Locking of Quantum Cascade Lasers (Theory)," Workshop in Infrared Physics, Seville, Spain, January 4-8, 2004.
28. F. X. Kaertner, "Advances in Laser and RF-Synchronization," TESLA-Collaboration Meeting, Berlin Germany, January 20-22, 2004.
29. F. X. Kaertner, "Laser Based Timing and Seeding of Free Electron Lasers with High Harmonics," Argonne National Laboratory, Chicago, Illinois, January 29-30, 2004.
30. P. Hsiung, Y. Chen, N. Nishizawa, P.R. Herz, T.H. Ko, J.G. Fujimoto, C.J.S. de Matos, S.V. Popov, J.R. Taylor, J. Broeng, V.P. Gapontsev, "All-fiber, continuous wave, Raman continuum sources for optical coherence tomography," OSA Biomedical Optics Topical Meetings, Miami Beach, Florida, April 14-17, 2004, paper SE7.
31. A.M. Kowalevich, Jr., P. Rakich, E. Ippen, J. Fujimoto, and K. Minoshima, "Multilevel 2D and 3D photonic devices fabricated in glass by a femtosecond oscillator," Conference on Lasers and Electro-Optics, CLEO, May 16-21, 2004, San Francisco, California, paper CMY8.
32. A. Sennaroglu, A.M. Kowalevich, A. Zare, and J.G. Fujimoto, "General design rules for multi-pass cavity lasers in ultrashort pulse generation," Conference on Lasers and Electro-Optics, CLEO, May 16-21, 2004, San Francisco, California, poster CTuP37.
33. N. Nishizawa, Y. Chen, P. Hsiung, V. Sharma, T.H. Ko, and J.G. Fujimoto, "All fiber high resolution OCT system using an ultrashort pulse high power fiber laser," Conference on Lasers and Electro-Optics, CLEO, May 16-21, 2004, San Francisco, California, paper CTuBB3.
34. C. De Matos, S.V. Popov, J.R. Taylor, P. Hsiung, Y. Chen, N. Nishizawa, P.R. Herz, T.H. Ko, J.G. Fujimoto, J. Broeng, and V. P. Gapontsev, "Continuous wave, all-fibre broadband sources for optical coherence tomography," Conference on Lasers and Electro-Optics, CLEO, San Francisco, California, May 16-21, 2004, paper CWJ1.
35. Q. T. Vu, L. Bányai, and H. Haug, O. D. Mücke, T. Tritschler, and M. Wegener, U. Morgner, F. X. Kaertner, G. Khitrova and H. M. Gibbs, "Microscopic theory of carrier-wave Rabi flopping and the Mollow band triplet in semiconductors," International Conference on Quantum Electronics (IQEC 2004), San Francisco, CA, May 22-27, 2004.
36. L. Matos, O. Kuzucu, T. R. Schibli, J. Kim, E. P. Ippen, D. Kleppner and F. X. Kaertner, "Direct frequency comb generation from a prism-less Ti:sapphire laser," Conference on Lasers and Electro-Optics (CLEO 2003), San Francisco, CA, May 22-27, 2004.
37. S. N. Tandon, J. T. Gopinath, G. S. Petrich, L. A. Kolodziejski, F. X. Kaertner, and E. P. Ippen, "Broadband Saturable Bragg Reflectors from the Infrared to Visible using Oxidized

- AiAs,” Conference on Lasers and Electro-Optics (CLEO 2003), San Francisco, CA, May 22-27, 2004.
38. Ch. Jirauschek, L. Duan, O. D. Mücke, and F.X. Kaertner, K. D. Hof, Th. Tritschler, and M. Wegener, „Semiconductor-based carrier-envelope phase detector,” Conference on Lasers and Electro-Optics (CLEO 2004), San Francisco, CA, May 22-27, 2004.
 39. J. Kim, F. X. Kaertner, V. Scheuer and G. Angelow, “Ultra-broadband beam splitter with matched group delay dispersion,” Conference on Optical Interference Coatings, Tucson, Arizona, June 27-July 2, 2004.
 40. J. Birge, Chr. Jirauschek and F. X. Kaertner, “Efficient analytic computation of group delay dispersion from optical interference coatings,” Conference on Optical Interference Coatings, Tucson, Arizona, June 27-July 2, 2004.
 41. A. Sennaroglu, A.M. Kowalewicz, Jr., F.X. Kaertner, and J.G. Fujimoto, “Compact prismless low-threshold 30 MHz femtosecond Ti:Al₂O₃ laser,” Conference on Lasers and Electro-Optics, CLEO, June 1-6, 2003, Baltimore, Maryland, paper CFA1.
 42. R.P. Prasankumar, Y. Hirakawa. A.M. Kowalewicz, Jr., F.X. Kaertner, J.G. Fujimoto, U. Morgner, and W.H. Knox, “An 8.6 MHz extended cavity femtosecond Cr:LiSAF laser pumped by single spatial mode diodes,” Conference on Lasers and Electro-Optics, CLEO, June 1-6, 2003, Baltimore, Maryland, paper CFA2.
 43. A.M. Kowalewicz, Jr., P. Rakich, E. Ippen, J. Fujimoto, and K. Minoshima, “Multilevel 2D and 3D photonic devices fabricated in glass by a femtosecond oscillator,” Conference on Lasers and Electro-Optics, CLEO, May 16-21, 2004, San Francisco, California, paper CMY8.
 44. A Sennaroglu, A.M. Kowalewicz, A. Zare, and J.G. Fujimoto, “General design rules for multi-pass cavity lasers in ultrashort pulse generation,” Conference on Lasers and Electro-Optics, CLEO, May 16-21, 2004, San Francisco, California, poster CTuP37.
 45. N. Nishizawa, Y. Chen, P. Hsiung, V. Sharma, T.H. Ko, and J.G. Fujimoto, “All fiber high resolution OCT system using an ultrashort pulse high power fiber laser,” Conference on Lasers and Electro-Optics, CLEO, May 16-21, 2004, San Francisco, California, paper CTuBB3.

Thesis

1. Oktay Onur Kuzucu, “High Repetition Rate Ti:Sapphire Modelocked Laser,” June 2003.
2. Karen Robinson, “Stabilization of Passively Modelocked Solid-State Lasers by use of Electronic Feedback,” June 2003.
3. R.P. Prasankumar, *Development and Application of Saturable Absorbers to Femtosecond Solid-State Laser Mode-Locking*, Ph.D. Dissertation, Department of Electrical Engineering and Computer Science, MIT, 2003.

Books

1. F. X. Kaertner, U. Morgner, T. R. Schibli, R. Ell, H. A. Haus, J. G. Fujimoto and E. P. Ippen, “Few-Cycle Pulse Generation directly from the Laser,” in “Few-Cycle Pulse Generation and its Applications, Springer Verlag, Topics in Applied Physics, ed. by F. X. Kärtner, submitted to Springer Verlag.